

2019:00027- Unrestricted

Report

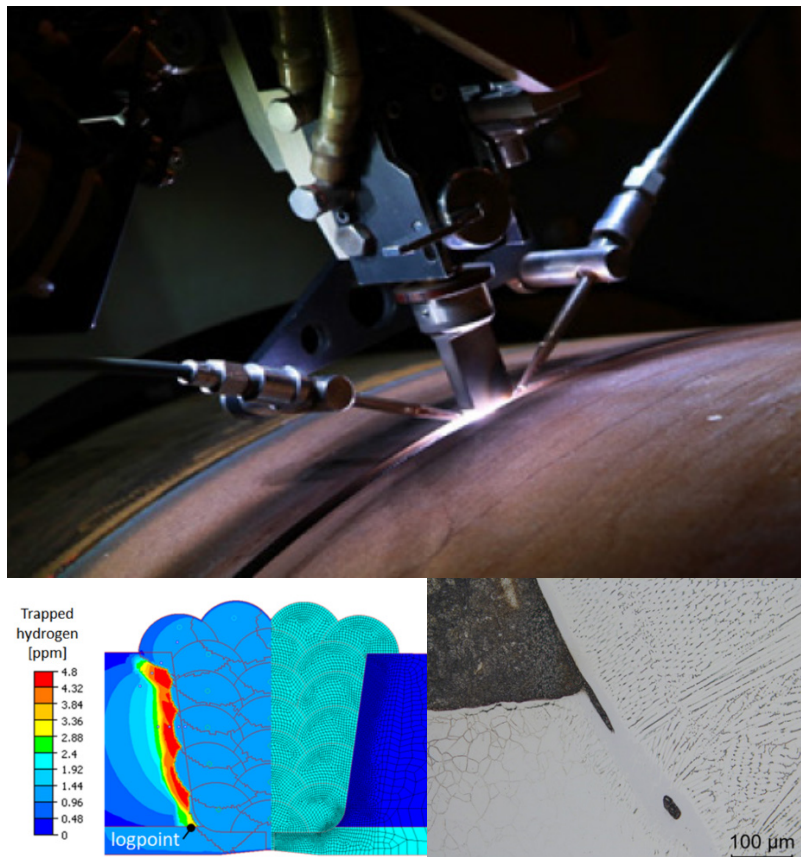
Knowledge basis for repair contingency of pipelines

Final report

Author(s)

Vigdis Olden

Dag Lindholm, Hallvard Fjær, Magne Rudshaug, Ragnhild Aune, Xiaobo Ren



Report

Knowledge basis for repair contingency of pipelines

Final report

KEYWORDS:

Welding
Steel
Pipelines
Clad
Hydrogen
Fracture
Finite element analyses

VERSION
05

DATE
2020-03-31

AUTHOR(S)

Vigdis Olden
Dag Lindholm, Hallvard Fjær, Magne Rudshaug, Ragnhild Aune, Xiaobo Ren

CLIENT(S)

RCN, Equinor, Gassco, TechnipFMC, EDF Induction, POSCO

CLIENT'S REF.

Kimberly Mayes, RCN

PROJECT NO.
102006704

NUMBER OF PAGES/APPENDICES:
69/1

ABSTRACT

The RCN competence project ROP was initiated in January 2014, with the main objective to establish basic knowledge on subsea hyperbaric repair welding and degradation of clad and lined pipes, as well as C-Mn steel. The project is motivated by the need for improving the contingency situation and increase the research effort related to clad pipe and CMn pipeline repair in the Norwegian Continental shelf. The research partners have been SINTEF, IFE and NTNU, the industry partners are Equinor, Gassco, Technip FMC, EFD Induction and POSCO.

This report summarizes the results from all work packages, a PhD thesis that was finalized in 2018 and post doc work finalized in February 2020. The work packages are: WP1 Structural Integrity, WP 2 Material and process modelling, WP3 Technical solutions and WP4 Demonstrators. An overview of the publications produced in the project is also given.

PREPARED BY
Vigdis Olden

SIGNATURE **Olden Vigdis**
Digitally signed by Olden Vigdis
DN: cn=Olden Vigdis
Date: 2020.04.01 13:35:29 +02'00'

CHECKED BY
Bård Nyhus

SIGNATURE **Nyhus Bård**
Digitally signed by Nyhus Bård
DN: cn=Nyhus Bård
Date: 2020.04.01 17:40:39 +02'00'

APPROVED BY
Magnus Eriksson

SIGNATURE **Eriksson Magnus**
Digitally signed by Eriksson Magnus
DN: cn=Eriksson Magnus
Date: 2020.04.01 17:31:19 +02'00'

SINTEF Industri
SINTEF Industry

Address:
Postboks 4760 Torgarden
NO-7465 Trondheim
NORWAY
Switchboard: +47 40005100

info@sintef.no

Enterprise /VAT No:
NO 919 303 808 MVA

REPORT NO.	ISBN	CLASSIFICATION	CLASSIFICATION THIS PAGE
2019:00027	978-82-14-06840-5	Unrestricted	Unrestricted

Document history

VERSION	DATE	VERSION DESCRIPTION
Version No 01	2019-01-18	Issue for internal review

Version No 02	2019-02-06	Issue for client review
---------------	------------	-------------------------

Version No 03	2020-02-28	Updated issue for client review
---------------	------------	---------------------------------

Version No 04	2020-03-25	Updated issue for client review
---------------	------------	---------------------------------

Version No 05	2020-03-31	Final issue
---------------	------------	-------------

Table of contents

1	Background	6
2	Brief summary.....	6
3	Comprehensive summary of the results from WP1-WP4.....	9
3.1	WP1 Structural integrity (WP leader: Vigdis Olden, SINTEF)	9
3.1.1	Task 1.1: Hydrogen diffusion	9
	TDS measurements	11
	Simulations of the TDS results in WeldsimS	14
3.1.2	Task 1.2: Modelling of hydrogen embrittlement (including notch tensile testing)	17
3.1.3	Task 1.3: Structural integrity	21
	Material.....	21
	Microhardness	22
	Fracture mechanics testing.....	25
3.2	WP2 Material and process modelling (Hallvard Fjær, IFE, Xiabo Ren, SINTEF)	30
3.2.1	Task 2.1 Weld arc modelling	30
3.2.2	Task 2.2 Weld pool modelling using SPH	38
3.2.3	Task 2.3 Modelling of hyperbaric welding	38
	The hydrogen diffusion model.....	38
	Simulation of the Tekken Y-groove test.....	39
	Case Study on Repair Welding of Clad Pipes	44
3.2.4	Task 2.4: Pre- and Post-Weld Heat Treatment	46
	Diffusion of Carbon at the Bimetallic Base-Clad Interface.....	46
3.3	WP3 Technical solutions (WP leader: Ragnhild Aune, SINTEF).....	50
3.3.1	Task 3.1 Hyperbaric CMT (Cold Metal Transfer) welding	50
	Root pass welding up to 35bar	50
	Root pass welding at 5bar - Robustness	53
3.3.2	Task 3.2: Subsea repair of clad and lined pipes & Task 3.3: Effect of shielding gas on phase constituents in the root pass	54
3.3.3	Task 3.4: Hydrogen effects.....	54
3.3.4	Task 3.5: Characterization of microstructures and secondary phases	54
3.3.5	Task 3.6: Pre- and post-weld heating.....	55
3.4	WP4 Demonstrators (Ragnhild Aune).....	55
4	PhD and Post Doc.....	59
4.1	PhD Lise Jemblie.....	59
4.2	Post doc Ivan Bunaziv	62
5	Education and recruitment.....	66

6	Project management	67
7	Publications.....	67

APPENDICES

Appendix 1 HISC screening testing of FL and WM of CoreWeld and Alloy 59 filler materials.

[Write report here]

1 Background

The RCN competence project ROP was initiated in January 2014, with the main objective **to establish basic knowledge on subsea hyperbaric repair welding and degradation of clad and lined pipes, as well as C-Mn steel.**

The project is motivated by the need for improving the contingency situation and increase the research effort related to clad pipe and CMn pipeline repair in the Norwegian Continental shelf.

The research partners are SINTEF, IFE and NTNU, the industry partners are Equinor (previously Statoil), Gassco, Technip FMC, EFD Induction and POSCO.

This report summarizes the results from four scientific work packages, a PhD thesis that was finalized in 2018 and Post Doc work that was finalized in 2020. The included work packages are: WP1 Structural Integrity, WP2 Material and process modelling, WP3 Technical solutions and WP 4 Demonstrators. The structure of the project is shown in Figure 1.

The sub goals of ROP as described in the project description are:

- Structural Integrity (WP1): To model the resistance towards fracture and degradation of materials and joints.
- Material and process modelling (WP2): To build basic knowledge on subsea clad and lined pipe hyperbaric repair welding
- Technical solutions (WP3): Address the technical solutions based on WP1 and WP2
- Demonstration (WP4): Verification of the models and technical solutions
- Education (WP1 & 2): To educate 2 PhDs
- Public dissemination (WP1, 2 & 3): To publish 15 papers in international journals and 15 in international conferences.

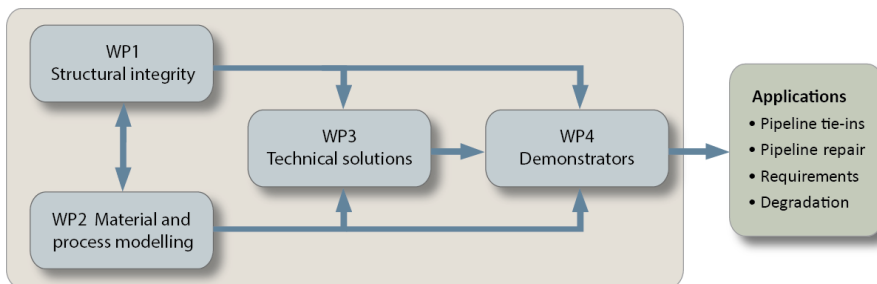


Figure 1 Structure of the ROP-project

A brief summary will be given, followed by an extensive summary of the results in WP1, WP2, WP3, WP3 as well as the PhD and Post Doc work. In the three last pages of the report you will find a numbered list of the publications financed by the project so far. Included in appendix 1 is reported additional work that was performed at SINTEF to establish some welded joint's susceptibility to hydrogen embrittlement (HISC). The report presents results from HISC screening testing of fusion line and weld metal of CoreWeld and Alloy 59 filler materials.

2 Brief summary

A short presentation of the main activities and take-aways from the different WPs is given as an introduction to the comprehensive summary in page 9.

WP 1 Structural integrity

This work package has included finite element simulations as well as small scale experimental laboratory work for input to and verification of predictive models for hydrogen induced cracking. Three research tasks have

been covered: Task 1.1 Hydrogen diffusion, focusing on establishing diffusion related parameters by experimental testing, 1.2 Modelling of hydrogen embrittlement, where we have applied the diffusion parameters to develop models for hydrogen fracture and 1.3 Structural integrity, where fracture mechanics testing and characterization of small-scale specimens have been the main activity.

Task 1.1: Hydrogen diffusion coefficients, hydrogen trapping energies and solubility have been measured for base metal and HAZ microstructure in X70 pipeline steel. Both the electrochemical permeation technique and thermal desorption spectrometry (TDS) have been applied, and TDS gave the most stable and trustworthy results. This work was performed in close cooperation with Kyushu University in Japan. The diffusion properties have also been modelled by WELDSIMS, giving a good match between measurements and simulations. The diffusion coefficients are about 3 times higher for BM material compared to HAZ, and the TDS results in general 10 times higher than the electrochemical permeation results. The results show that trapping energies in the range 20 – 60 kJ/mol are relevant to include in the prediction models.

Task 1.2: The model for prediction of hydrogen induced fracture is based on applying user defined elements for simulation of diffusion, stresses, strains and cracking within the software ABAQUS. The actual cracking is represented by cohesive zone elements that 'fractures' when a critical energy level is reached. The critical energy is influenced by the variation in hydrogen concentration. The model has been calibrated by tensile testing of specimens with different notch geometry, in air and under hydrogen charging conditions, and applying diffusion information obtained from Task 1.1. The calibration process has shown that the cohesive elements need to be corrected for the effect of geometry. The model predicts fracture when the combined effect of hydrogen concentration and applied stresses reaches a critical level.

Task 1.3: The structural integrity task has been devoted to materials characterization and investigation of fracture toughness of the interface between cladding and base material of carbon steel. Downsized fracture toughness specimens have been tested in air and CP, both before and after welding. There is a clear influence of hydrogen on the fracture toughness of clad pipes without a Ni-interlayer between the cladding and the pipeline steel. Welding contributes to a further reduction in toughness.

A Ni interlayer between clad and pipeline steel is clearly preferable in clad pipelines to avoid influence of hydrogen on the fracture toughness, both in not welded and welded condition. The reason is the mitigation of carbon diffusion from the pipeline steel into the clad and thus avoiding Cr-carbide precipitations. In the PhD work, the model based on cohesive elements described in Task 1.2 has been applied to predict fracture in the not welded specimens.

WP2 Material and process modelling

This work package has addressed modelling of the electromagnetic and thermal phenomena in the welding arc, mass flow in the melt pool and the development of temperature, stresses and hydrogen concentration in the weldment. It has been closely interlinked with work conducted in WP1 and WP3. Four sub-tasks were defined; Task 2.1 Weld arc modelling, Task 2.2 Weld pool modelling using Smooth Particle Hydrodynamics (SPH), Task 2.3 Modelling of hyperbaric welding, and Task 2.4 Pre- and post-weld heat treatment. The latter two with basis in WELDSIMS, a FEM-based software tailor-made for welding of steels.

Task 2.1: The focus in this task has been to understand the arc physics and make a model to calculate the heat flux into the workpiece. We also wanted to see how hyperbaric conditions affects the heat flux. An understanding of the physics has been achieved. A simplified model was attempted, but the approach was not successful. The reason for this may be that Fe is not a thermionic¹ material. The behaviour of non-thermionic materials is not well understood. We propose a comprehensive and self-contained model for GMAW. This approach includes metal vapor in the shielding gas, an important effect in GMAW. We have also obtained the thermodynamic and transport data needed to implement the model for hyperbaric conditions. Other necessary hyperbaric data is also provided. A solution of this model was outside the scope of this project. We propose a simplified engineering type model for the heat flux based on known arc efficiency data.

Task 2.2: The smooth Particle Hydrodynamics (SPH)-based software was evaluated as a possible approach

¹ Thermionic emission: Discharge of electrons from heated materials. Encyclopædia Britannica. www.britannica.com

for root pass simulation. It successfully simulates the shape of the weld pool but gives no information on stresses/strains or microstructure.

Task 2.3: A revised hydrogen diffusion model in WELDSIMS ensures mass conservation for hydrogen during phase transformations and provide a better description of the diffusion of hydrogen where a mixture of phases is present.

With 5 ppm hydrogen introduced in the weld metal, welding experiments of the Tekken Y-groove test revealed that preheating at 45°C was required to avoid cracking. This threshold temperature rose to 120°C with 10.3 ppm in the weld. Based on the revised hydrogen diffusion model developed in WP2, welding experiments carried out in WP3 and hydrogen trap data derived in WP1, WELDSIMS computer simulations gave detailed information about how the microstructure, stresses and hydrogen – both lattice and trapped – developed during and after welding of the Tekken test. For 10.3 ppm hydrogen introduced in the weld and preheat at 69°C, the Tekken test cracked when the simulated combination of principal stress and level of hydrogen at the crack tip reached 1735 MPa and 3.1 ppm. For 5 ppm hydrogen introduced in the weld and no preheat, this combination changed to 1930 MPa and 1.3 ppm. Hydrogen embrittlement is generally considered to be influenced by an unfavorable combination of large level of hydrogen, large residual stresses and brittle microstructure in and adjacent to the weld. In the Tekken the residual stresses are significantly influenced by the level of preheat. Because of the size of the components to be welded, and the fact that the complete structure is preheated, preheating keeps the weld and the adjacent material hot for a relatively long time after welding. Diffusivity of hydrogen is more efficient at elevated temperatures, which means that the diffusion of hydrogen in the Tekken test is also influenced by the level of preheat. For a field weld the constructions are typically larger, which means that added preheat is quickly conducted to surrounding cold material. Preheating influences on the resulting residual stresses, less to decrease of hydrogen in the weld. However, for field welds in humid surroundings, preheating is often used to dry the metal surfaces. Based on realistic process parameters, a numerical case study was carried out to examine the influence of heat treatment (pre, interpass and post) on residual stresses, microstructure and decay of hydrogen in and adjacent a realistic multi-pass U-groove weld. Post-weld heat treatment (PWHT) was demonstrated to have significant influence on reduction of hydrogen in the weld.

Task 2.4: Without a protective nickel interlayer between the base and the clad, carbon atoms have the potential to migrate across the bimetallic interface and form carbides and intermetallic compounds that degrade the structure adjacent to the interface and increases the local embrittlement. Computer simulations based on WELDSIMS identifies the diffusion bonding process to manufacture the clad pipes as the main thermal process causing a carburized/decarburized zone adjacent to the clad-base interface. PWHT too, if performed at a high temperature and/or long time, promotes detrimental diffusion of carbon.

WP3 Technical solutions

This part has comprised experimental laboratory work with the objective of developing technical solutions based on input from WP1 and WP2.

Task 3.1 Hyperbaric CMT: The main part of the work in WP3 has addressed hyperbaric CMT root pass welding using different combinations of base and filler wire materials in different fixed welding positions (12, 3, 0430 and 6 o'clock positions). Acceptable root pass penetrations are achieved for different fit-ups (2-1.5-2 and 2-0-0) at 5 and 35 bar. Combination of base and filler wire materials with high viscosity gives acceptable root pass results with root gap but is more challenging without root gap and high low, especially at 3 and 0430 o'clock positions, where the weld pool does not flow out into the sidewalls and the penetration is limited. The combination of base and filler wire materials with low viscosity is more challenging both with and without root gap, although it is possible to get good results. Without root gap the weld pool flows better into the sidewalls and the penetration is good. However, the parameter window for both fit-ups is narrow because of the low viscosity. For the same working distance, the arc voltage increases as the chamber pressure increases. The welding parameters must be adjusted (more or less) depending on the base and filler material combinations for different chamber pressures. The most robust welding positions are 3 and 0430 and the least robust welding position is the 6 and 12 o'clock positions.

WP4 Demonstrators

To demonstrate practical hyperbaric welding the welding equipment was mounted in a pressure chamber at Killingøy where orbital welding was possible. Based on experimental work in Task 3.1, where CMT root pass welding in fixed position were in focus, the most promising combinations of base and filler wire materials were tested further. Successful orbital root pass welding was performed both for C-Mn (X70) and clad pipes for different fit-ups (2-1.5-2 and 2-0-0) at 5 and 150bar. The root passes were welded only downhill, i.e., from 12-3/9-6 o'clock positions. For the same working distance, the arc voltage increases as the chamber pressure increases so the welding parameters must be adjusted to obtain the same heat input. The C-Mn- and clad pipes were also filled up completely including root and filler passes at 150bar. For the filler passes the pulsed MIG welding method was used. Mechanical test results, as Charpy-V, hardness and all weld, were all acceptable according to standard². The results show that is possible to do remote butt welding of pipes using the CMT and pulsed MIG method at least up to 150bar, which corresponds to a water depth of 1500 msw.

3 Comprehensive summary of the results from WP1-WP4

3.1 WP1 Structural integrity (WP leader: Vigdis Olden, SINTEF)

The term structural integrity includes resistance to hydrogen induced and/or assisted embrittlement and the risk of ductile or brittle fracture. In the former case, embrittlement may be due to H pick-up from CP (cathodic protection) of the pipeline, sour service with a certain amount of H- sulphide or H introduced during welding.

3.1.1 Task 1.1: Hydrogen diffusion

The diffusion properties of hydrogen in the pipeline steel are vital to establish in order to be able to simulate local hydrogen concentrations as a function time and local stresses and strains, which again will determine the onset of hydrogen induced fracture. The work in this task has been performed along two parallel and interlinked paths:

1) The ROP project have closely collaborated with the RCN researcher project HIPP³ and Hy-Flex⁴ in applying and verifying a user defined numerical framework for stress and strain driven hydrogen diffusion, developed within these two projects.

2) Experimental work establishing input parameters as diffusion coefficients and hydrogen trapping energies, for the model. International collaboration with Kyushu University in Japan has been central in this work.

The model framework is based on a modified Fick's law, which is implemented through a sub-routine (UMATH) in the software ABAQUS:

$$\frac{\partial C_L}{\partial t} + \frac{\partial C_T}{\partial t} - \nabla \cdot (D_L \nabla C_L) + \nabla \cdot \left(\frac{D_L C_L \bar{V}_H}{RT} \nabla p \right) = 0$$

Where C_L is the hydrogen concentration in normal interstitial lattice sites, C_T is the hydrogen concentration in reversible traps, D_L is the lattice diffusion coefficient, \bar{V}_H is the partial molar volume of hydrogen in iron ($7.106 \cdot 10^3 \text{ mm}^3/\text{mol}$) and p is the hydrostatic pressure. The hydrogen concentration in lattice and traps are in equilibrium. The hydrogen concentration in traps are again linked to the number of trap sites in the material

² Offshore standard DNV-OS-F101, "Submarine Pipelines Systems", October 2013.

³ Hydrogen-induced degradation of offshore steels in ageing infrastructure - models for prevention and prediction (HIPP), RCN Project No.: 234130

⁴ Field life extension through controlling the combined material degradation of fatigue and hydrogen (HyF-Lex), RCN Project No.: 244068

due to plastic deformation through the established relations shown in Figure 1. A detailed model description can be found in publication no 26 and PhD thesis (publ. no 31) and in SINTEF Report A26585 (publ. no 4).

An example of applying the diffusion model in numerical simulations are shown in Figure 3. Figure 3a presents the distribution stress and Figure 3b the distribution of the normalized, total hydrogen concentration at the point of fracture, for five different tensile test geometries tested under hydrogen charging conditions. The stress and H concentration are plotted from the surface (notch surface) and 2 mm into the sample. For these simulations a diffusion coefficient (D_L) of $7.60 \cdot 10^{-11} \text{ m}^2/\text{s}$ (established for HAZ) simulated microstructure during the DEEPIT project⁵) and a trap binding energy of 37 kJ/mol was applied. Note that the sharpest notch (C – fatigue crack) needs a lower hydrogen concentration for a H crack to initiate, compared to the less sharp notches (V-notch and E-spark eroded notch). See Task 1.3 for description of the sample geometries and results from the experimental tensile testing.

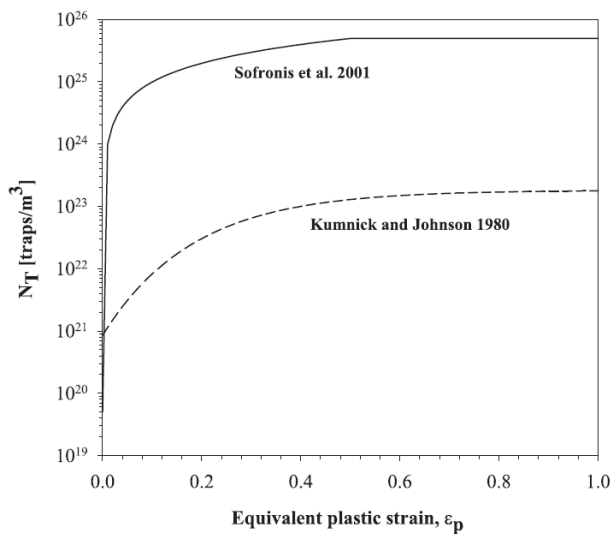


Figure 2 Dislocation trap density models

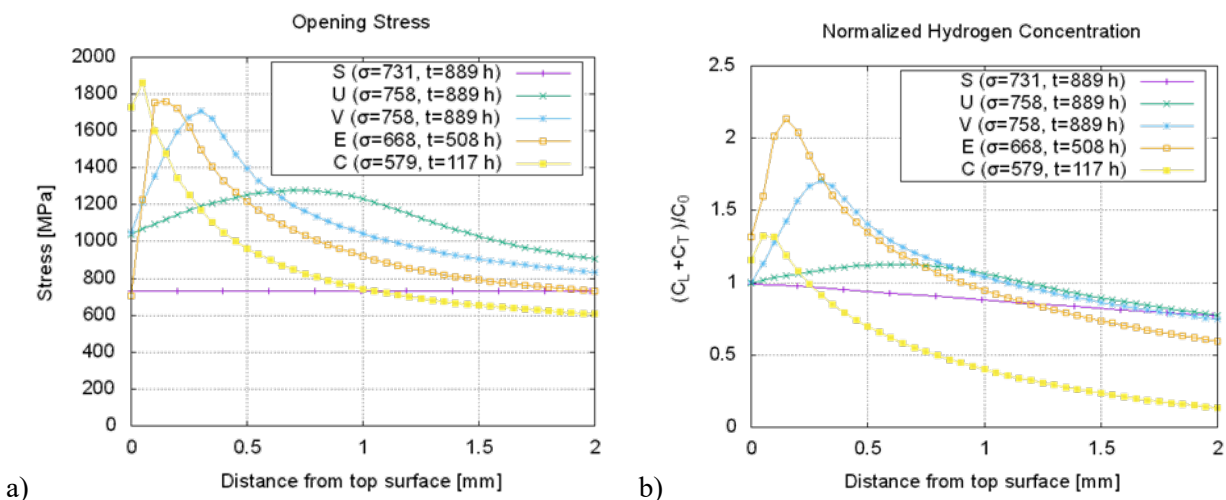


Figure 3 Opening stress distribution and the distribution of the normalized total hydrogen concentration ($C_L + C_T$) for different notch tensile geometries at the point of fracture.

⁵ Deep water repair welding and hot tapping, RCN Project No.: 192967

In the first part of the ROP project, hydrogen diffusion coefficients were sought established by permeation measurements in an electrochemical cell at NTNU. The idea was to redo the permeation measurements from the previous DEEPIT project, that were questioned due to heavy oxidation of some test specimens. However, the challenge with oxidation persisted in the new tests, and the results were therefore discarded. An NTNU Master thesis was written on the subject.

TDS measurements

A collaboration with Kyushu University on measuring the diffusion coefficient and trapping parameters applying thermal desorption spectrometry (TDS), with H gas charging and thus better controlled surface conditions was therefore established.

Throughout 2016 and 2017, X70 base metal and typical HAZ microstructure-samples were investigated with TDS, both with respect to trapping energies, hydrogen content and diffusion coefficients.

The specimens were hydrogen charged at 100 MPa H₂-pressure at 85°C for 70 hours, to ensure filling of all traps and maximize the lattice concentration. The TDS measurements were carried out at different heating rates, and gave three hydrogen desorption peaks at ~100°C, ~170°C (reversible traps) and ~450°C (irreversible traps), see Figure 4. The activation energies for the reversible traps were calculated as 19,7 kJ/mol and 65,3 kJ/mol, and for the irreversible ones 117 kJ/mol, see Figure 5 . The results reflect that the same types of traps are present in both BM and HAZ. The results also show, that there is a higher amount of hydrogen present in reversible traps in HAZ compared to the BM.

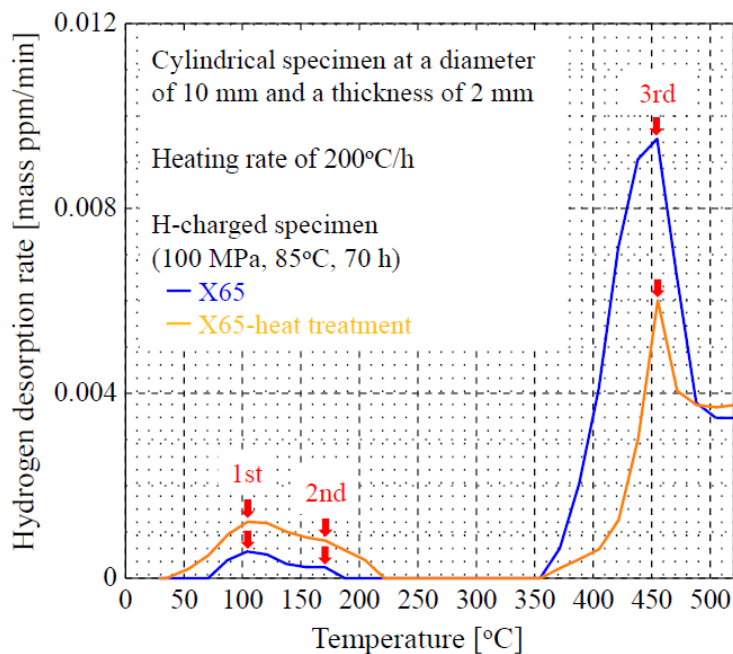


Figure 4 Thermal desorption analyses of X65 BM and HAZ, at a heating rate of 200°C.

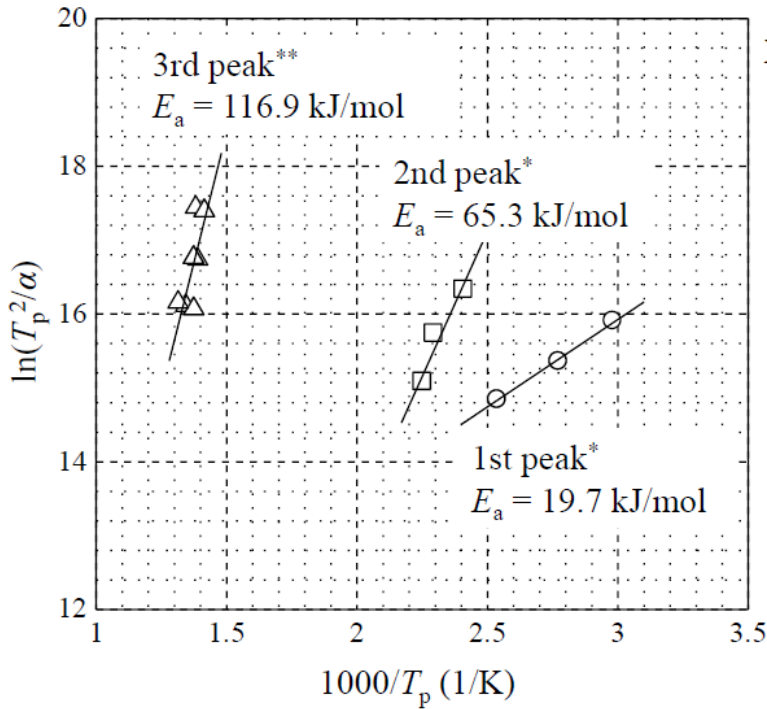
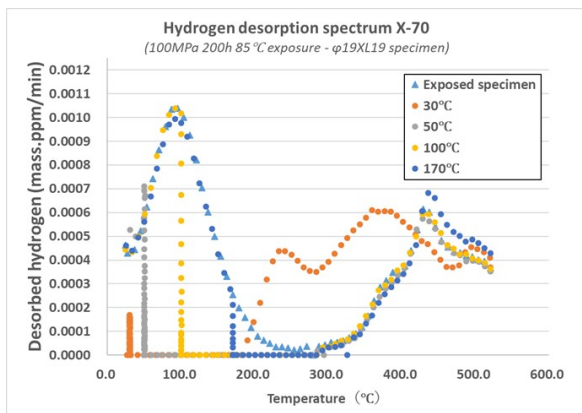


Figure 5 Activation energy (trapping energy) of reversible and irreversible traps in X65 steel (BM and HAZ).

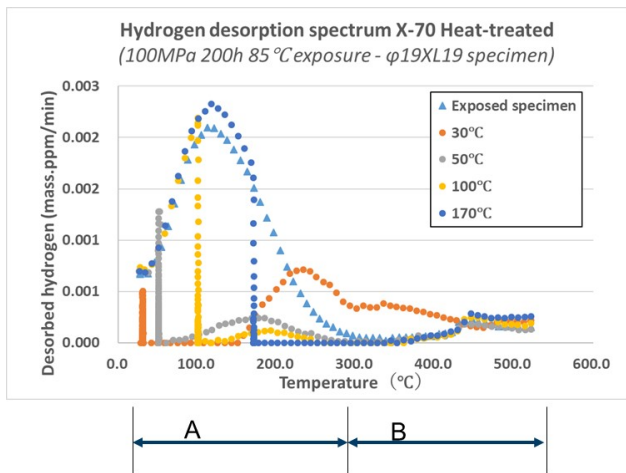
The amount of hydrogen present in the different trap types, were analyzed by measuring the desorbed hydrogen aired out at different temperatures, keeping the samples at temperatures representing lattice plus reversible traps (A) and irreversible (B) traps. The blue triangles represent the curve for hydrogen released during continuous heating of the sample from room temperature. The orange, grey, yellow and blue circles, however, show the hydrogen released when keeping the temperature stepwise constant at 30, 50, 100 and 170°C respectively, representing different trapping energies. After 170°C the same notations show the hydrogen released from the same samples during following continuous temperature increase from 170°C. The results are given in Figure 6 a) for BM and Figure 6 b) for HAZ.



a)

Desorbed amount (cumulated) (mass.ppm)

	Exposed specimen	30°C	50°C	100°C	170°C
A	0.067600	0.040870	0.062345	0.065240	0.063300
B	0.045535	0.071065	0.042700	0.044820	0.046410
Total	0.113135	0.111935	0.105045	0.110060	0.109710



Desorbed amount (cumulated) (mass.ppm)

	Exposed specimen	30°C	50°C	100°C	170°C
A	0.183540	0.152840	0.204125	0.197325	0.197740
B	0.014370	0.029535	0.011645	0.013815	0.016845
Total	0.197910	0.182375	0.215770	0.211140	0.214585

b) **Figure 6 Desorbed hydrogen (wppm) in lattice plus reversible traps (A) and irreversible traps (B) for X70 steel. a) Base metal b) Weld simulated HAZ**

The main observations are:

For BM, the hydrogen is redistributed between the lattice and the irreversible traps, seen from clear peaks both at low and higher temperatures. The irreversible traps (B) represent 45.5% of the total hydrogen amount which indicate that this trap type is not negligible for the base metal. The remaining part of the total hydrogen is contained in the lattice and reversible traps (A). The total amount of desorbed hydrogen is however low: ~0.1 ppm.

For weld simulated HAZ, the hydrogen is redistributed between lattice, reversible traps and irreversible traps. The irreversible traps represent only 7.3% of the total hydrogen in this case (There is very little hydrogen released above 170°C). The remaining hydrogen is contained in the lattice (almost totally) and one single trap of low energy. Traps (sites) with a low energy level of 20 kJ/mol are dominating. The total amount of desorbed hydrogen is: ~0.2 ppm.

The lattice diffusion coefficients for BM and HAZ were mapped as a function of holding temperature (30, 50, 100 and 170°C), and is presented in Figure 7. It may be noted that the diffusivity at 30°C is about 10 times higher as compared to the applied diffusivity in the model (measured by the electrochemical permeation technique at room temperature). This may reflect that the diffusivity measured by TDS is not slowed down by an oxide layer, as may be the case for the electrochemical measurements.

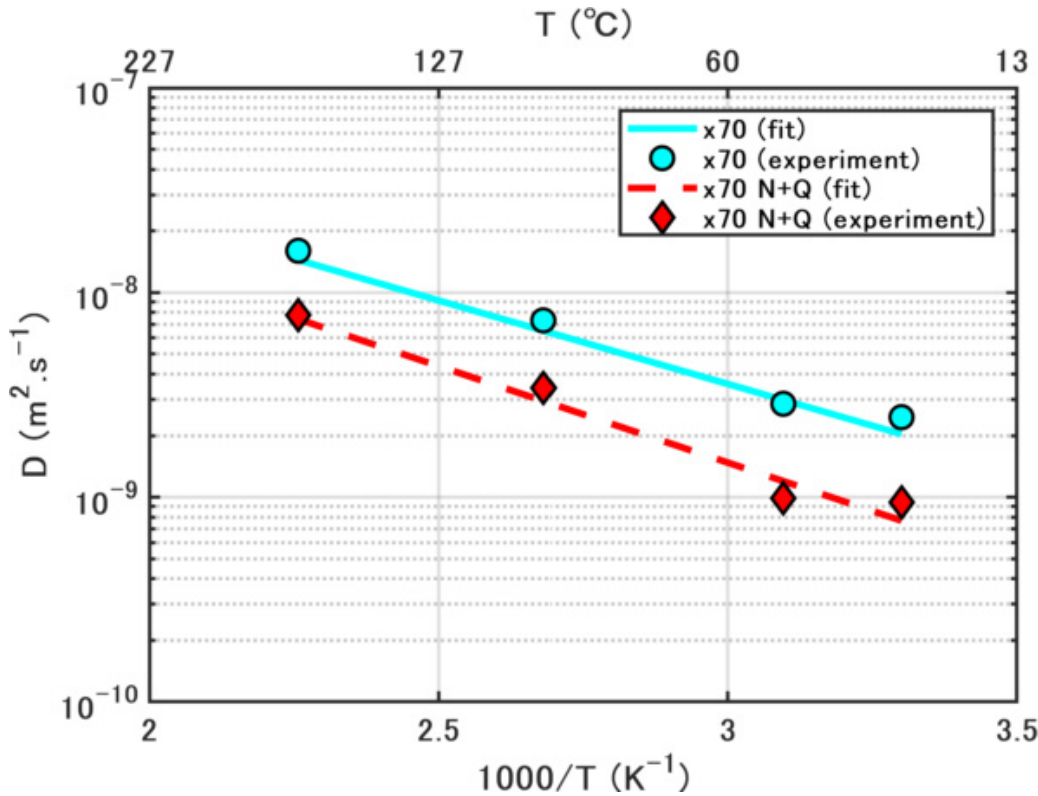


Figure 7 Diffusion coefficients as a function of temperature. Circles represent BM and diamonds HAZ.

Simulations of the TDS results in WeldsimS

The hydrogen diffusion and desorption tests at Kyushu University have also been simulated with the FEM program WELDSIMS. In these test, stresses and gradients in solubility can be assumed to be negligible, and the conservation equation can be simplified to

$$\frac{\partial C}{\partial t} = \frac{\partial C_L}{\partial t} + \frac{\partial C_T}{\partial t} = \nabla \cdot (D \nabla C_L)$$

The hydrogen concentration in traps is assumed to be in thermodynamically equilibrium with the lattice concentration. This condition can be expressed by the difference in energy between a trap site and a lattice site ΔE_T , and the occupancy in lattice sites $\theta_L = C_L/N_L$ and in traps $\theta_T = C_T/N_T$.

$$\frac{\theta_T}{\theta_L (1 - \theta_T)} = \exp\left(\frac{\Delta E_T}{RT}\right) = K_T$$

Here, the approximation $\theta_L \ll 1$ has been used. N_L and N_T are respectively the density of lattice sites and trap sites and K_T is the equilibrium constant. Including the effect of varying temperature, eliminating C_T from the equations, and allowing for co-existence of several types of traps with different trap binding energies $\Delta E_T^{(i)}$ one obtains

$$\left(1 + \sum_i \frac{N_T^{(i)} N_L K_T^{(i)}}{(K_T^{(i)} C_L + N_L)^2}\right) \frac{\partial C_L}{\partial t} = \nabla \cdot (D \nabla C_L) + \sum_i \frac{N_T^{(i)} N_L K_T^{(i)} \Delta E_T^{(i)} C_L}{RT^2 (K_T^{(i)} C_L + N_L)^2} \frac{\partial T}{\partial t}$$

As it turned out to be difficult to identify peaks in the TDS spectra for as-received material (due to very low H content), tests on heat treated material was chosen for analyses by numerical simulations. In the simulations of the diffusivity tests, a 2D axisymmetric solution domain was applied whereas the simulations of the TDS tests, were carried out on a 1D domain involving one half of the sample thickness. A large part of the hydrogen must have escaped from the samples before the experiments started, especially for the thin TDS samples. At the time the heating of the samples started from a temperature of 25°C, the lattice concentration of hydrogen in the centre of the test specimen was set to ca 0.0005 ppm in the simulation of the TDS tests and ca 0.02 ppm in the simulations of the diffusion tests. Trap densities and trap energies fitted to match the experimental data from both the diffusion tests and the TDS tests are listed in Table 1.

Table 1 Trap data applied in simulations.

Trap type	I	II	III	IV
Trap energy (kJ/mol)	20.0	57.5	69.0	120.0
Trap density (m ⁻³)	2.37×10 ²⁷	1.0×10 ²³	5.0×10 ²²	7.0×10 ²²

In general, the computed hydrogen desorption from the simulations of the diffusion tests at 50°C and 100°C is in Figure 8 seen to match the experimental results very well. In order to identify the significance of the different trap types with respect to the computed TDS spectrum, a simulation omitting the traps of type III and IV and another simulation including only traps of type I is compared with the simulation of the test with a heating rate of 200°C/s that includes all 4 types of traps. The traps type III and IV is in Figure 8 seen not to affect the results before the temperature reaches 100°C. One can assume that the high energy of these traps will cause these traps to be fully occupied for lower temperatures. With only traps of type I there is hardly seen any peak in the computed TDS spectrum.

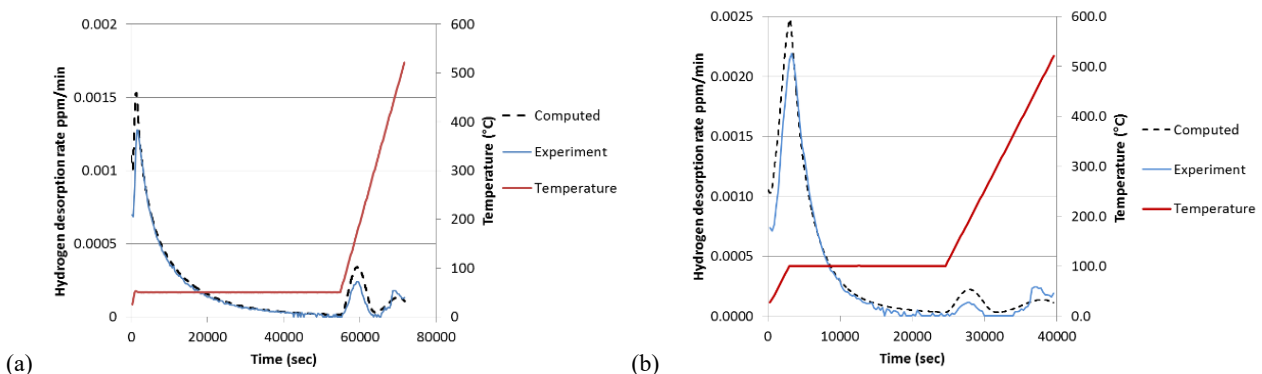
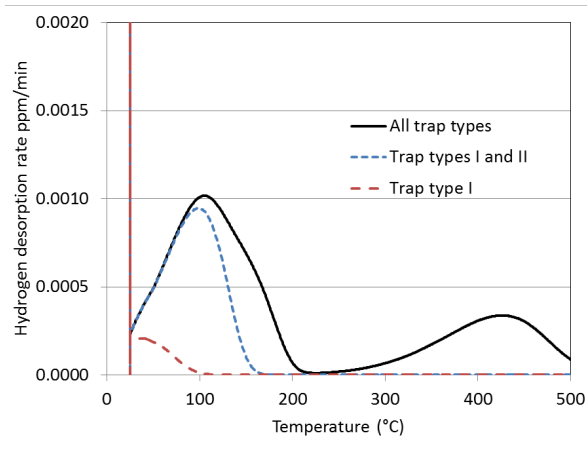


Figure 8 Comparison of experimental and computed hydrogen desorption rate from tests involving diffusion at (a) 50°C and (b) 100°C



(b) **Figure 9 Results from simulations of the TDS experiments with a heating rate of 200°C/s showing the significance of the different types of traps.**

Although trap energies found in Table 1 differ somewhat from the values obtained by Choo-Lee’s method seen in Figure 5, both sets of results contain a similar mix of low and high energy traps. However, the theoretical basis for the methods are quite different. The finite element analyses are based on the assumption of thermodynamic equilibrium, whereas the Choo-Lee’s method only consider the thermal activation in a de-trapping process. When the assumption of low trap occupancy ($\theta_T \ll 1$) is valid, it can be shown that the parameters in Kissinger’s formula on which the Choo-Lee’s method is based can be derived from the effective diffusivity and the dimension of the sample. In the investigated material, only the traps with the lowest energy satisfy the low occupancy requirement, whereas the traps with higher energy has a significant or almost complete occupancy at lower temperatures or high lattice concentration.

The efficient diffusivity will only be independent of the lattice concentration if the occupancy of all types of traps is either very low or close to 1. In Figure 10, D^* divided by the lattice diffusivity is shown as a function of temperature for different values of the lattice concentration. For temperatures below 80°C and a lattice concentration above 0.01 ppm, D^* is independent of the lattice concentration. This corresponds to a situation where only the low energy traps affect the diffusivity whereas traps with higher energy are fully occupied. These conditions with a low temperature and high C_L are the most relevant for oil and gas applications, and for these conditions a good agreement is found between model and the diffusion experiments. However, in the case of a higher temperature or a lower lattice concentration, the occupancy of the traps with energy 57.5 kJ/mol becomes significantly lower than 1 and D^* becomes lower as also these traps becomes active slowing down the diffusion. As the tests at Kyushu University involved much higher lattice concentration than the electrochemical permeation tests at SINTEF, this figure can explain the large difference in measured effective diffusivity. In the pressure charged samples at Kyushu University only the low energy traps affect the diffusivity, whereas the traps with energy 57.5 kJ/mol assumable where only partly occupied in the SINTEF tests and therefore influenced the tests to indicate a much lower efficient diffusivity.

The TDS and modelling work were presented at the 28th International Conference ISOPE 2018. A full paper is available in the conference proceedings. The results will also be published in the International journal IJOPE, which contain the papers from the conference that through peer review qualified for journal publication. The paper was written in cooperation with researchers from Kyushu University, see publication no 33.

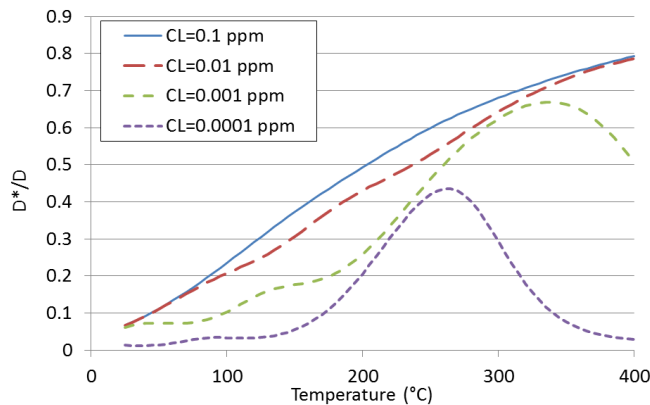


Figure 10 D^*/D as a function of temperature for different values of the lattice concentration

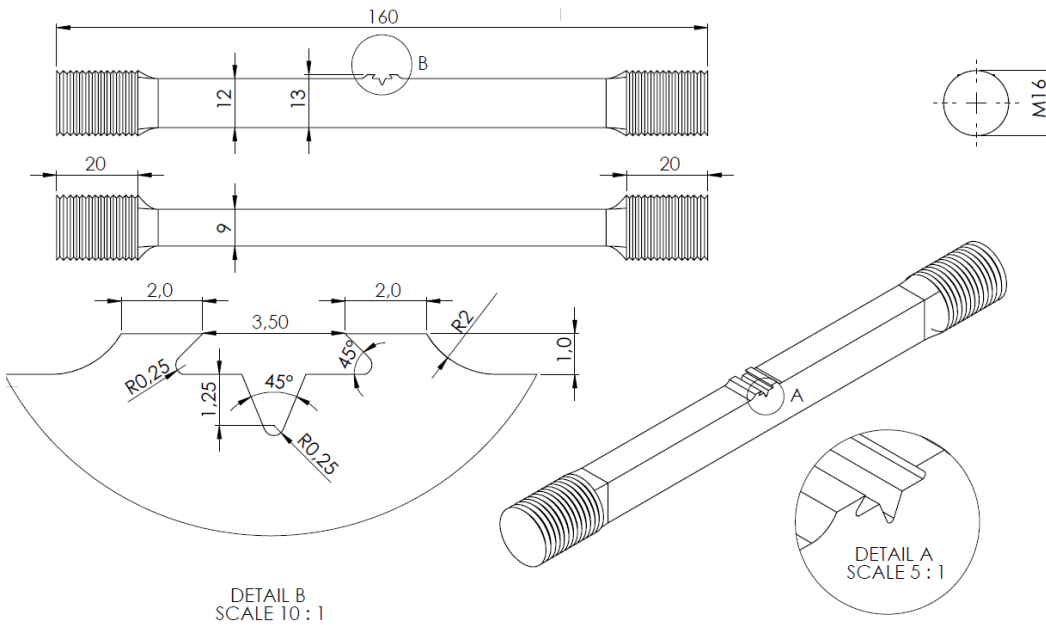
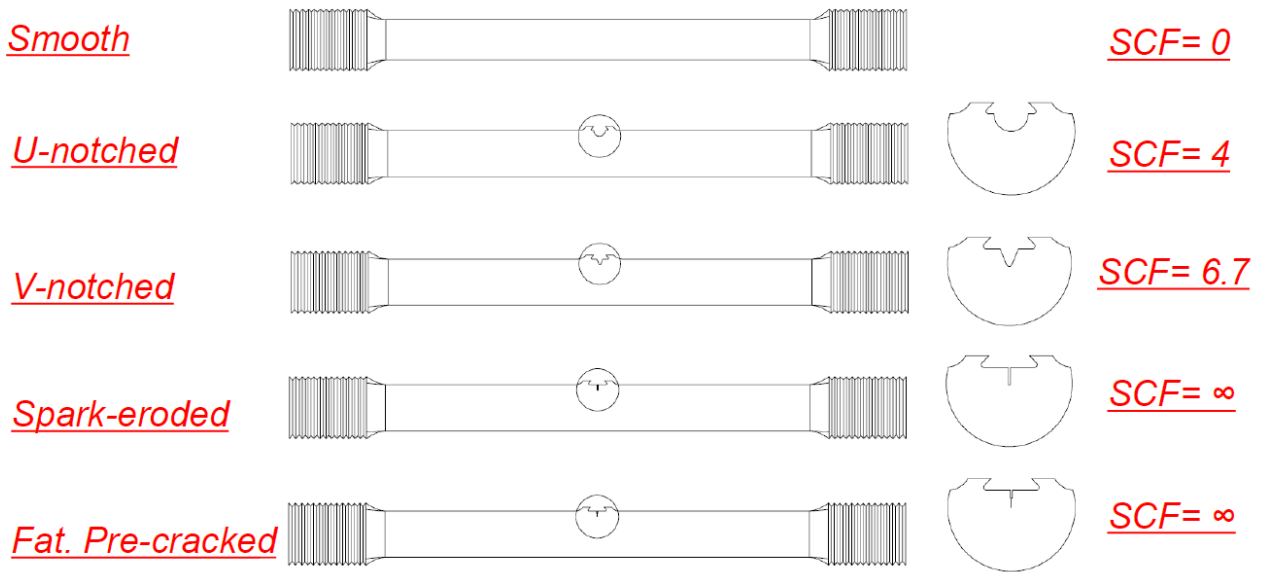
3.1.2 Task 1.2: Modelling of hydrogen embrittlement (including notch tensile testing)

User defined cohesive elements (UEL) able to continuously read and respond to the stress and strain influenced hydrogen concentration given from the diffusion simulation have been implemented in ABAQUS. These elements will 'break' when they reach a critical energy level that represents fracture initiation. The description of the UEL can be found in SINTEF Report 28059 - Cohesive zone element, publication no 24.

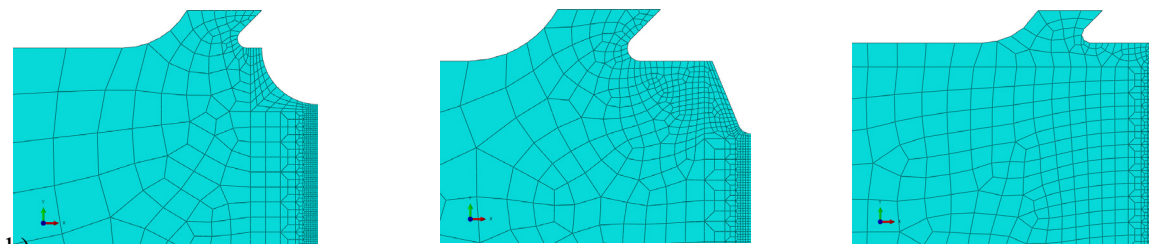
The main part of the work in this task has been to calibrate the cohesive elements in the numerical model to the experimental results from notch tensile testing, with the aim to represent H induced cracking. The tensile test specimen geometries have been: Smooth, U-notched, V-notched, with eroded crack and fatigue crack, representing stress concentration factors between zero and infinite. Numerical models of the same geometries were made. An overview of the test sample geometries and some examples of their model representation are shown in Figure 11 a-b.

The test specimens consist of X70 pipeline steel with a micro structure representative of the coarse-grained HAZ (1280°C for 35 min and quenched). Type of structure? Bainite? The resulting $R_{p0.2}$ and tensile stress are 643 and 831 MPa respectively and the average hardness is 290 HV10.

The testing in hydrogen (CP at -1050 mV_{SCE}) was performed in a stepwise constant load manner, starting at 86% of yield and increasing the load by 2% every second day until failure, to give hydrogen time to diffuse. For the testing in air, the load was increased every second hour. All tests were run in room temperature. The net section stress results at failure are presented in Figure 12. It is worth noticing that the sample with crack was not successfully tested in air due to large trough thickness plastic deformation in the notch area, that at one point gave a reduction of the CTOD. This result is therefore disregarded. Two parallels were tested for all geometries under CP conditions. A clear reduction in critical net section stress is observed, especially for the sharp notches. The model is calibrated for the air condition (blue dots) and the lowest net section stresses under CP conditions (lower red dots).



a)



b)

Figure 11 Tensile sample geometries a) The five geometries, representing stress concentration factors between zero and infinite. A detailed view of the V-notch sample is presented.

b) Numerical representation of the half notch of the U, V and eroded notch samples.

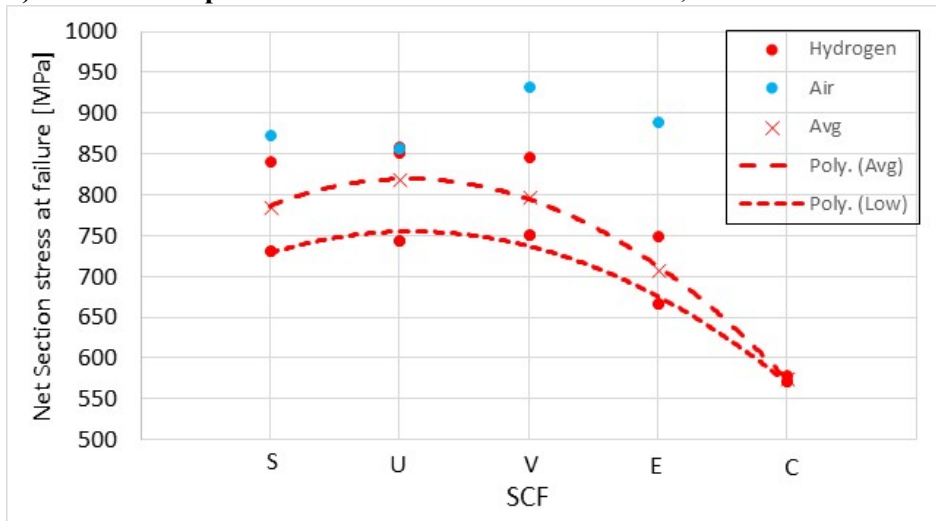


Figure 12 Net section stress at failure for smooth (S) and notched tensile specimens U (U-notch), V (V-notch), E (eroded) and C (crack) tested in air (blue) and CP (red). The X-es represent the average from the two parallels in CP conditions. The lower curve represents the targeted values for the numerical simulation of hydrogen induced fracture.

The opening stress and the hydrogen concentration (normalized) in the models at the point of fracture of the experimental tests are given in Figure 3 a-b. The applied diffusion properties are presented in in Table 2.

Table 2 Diffusion properties in the numerical model for hydrogen induced cracking

X65-X70 Coarse grained HAZ	Diffusion Coefficient (D_L) mm^2/s	Initial H conc. (C_L) mol/mm^3	Trap binding energy (E_b) kJ/mol	Partial molar volume of H, (\overline{V}_H), mm^3/mol
	$7.60 \cdot 10^{-5}$	$3 \cdot 10^{-11}$	37	$7.106 \cdot 10^3$

It has been an asset for this work that V. Osen at SINTEF have developed a new method that visualizes the results for the user defined elements. This is not a standard option in ABAQUS. The method is described in SINTEF Report 2019:00006, Visualization of user-defined elements in Abaqus, publication no 37. A visualization stress fields in a V-notch tensile specimen is shown in Figure 13

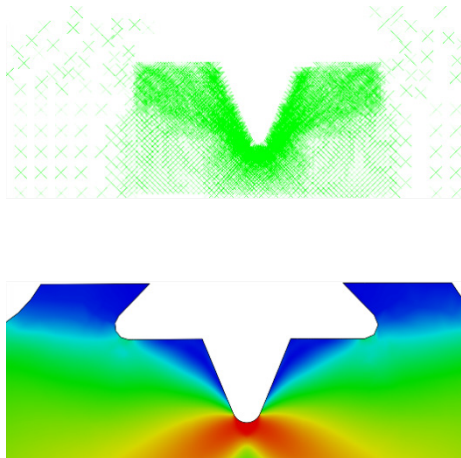


Figure 13 Visualization of user defined elements. In ABAQUS, user defined elements are only shown as X-s (upper plot), whereas the new method gives full visualizing possibilities (lower plot).

A comparison of experimental and numerical results is given in Figure 14. Except for the smooth hydrogen influenced geometry, the tendency is slightly conservative results for the numerical model. Note the following: Since we do not have experimental results in air for the specimens with sharp crack (C), the numerical results in hydrogen for this geometry is uncertain. This is because the model initially is calibrated to the air-results.

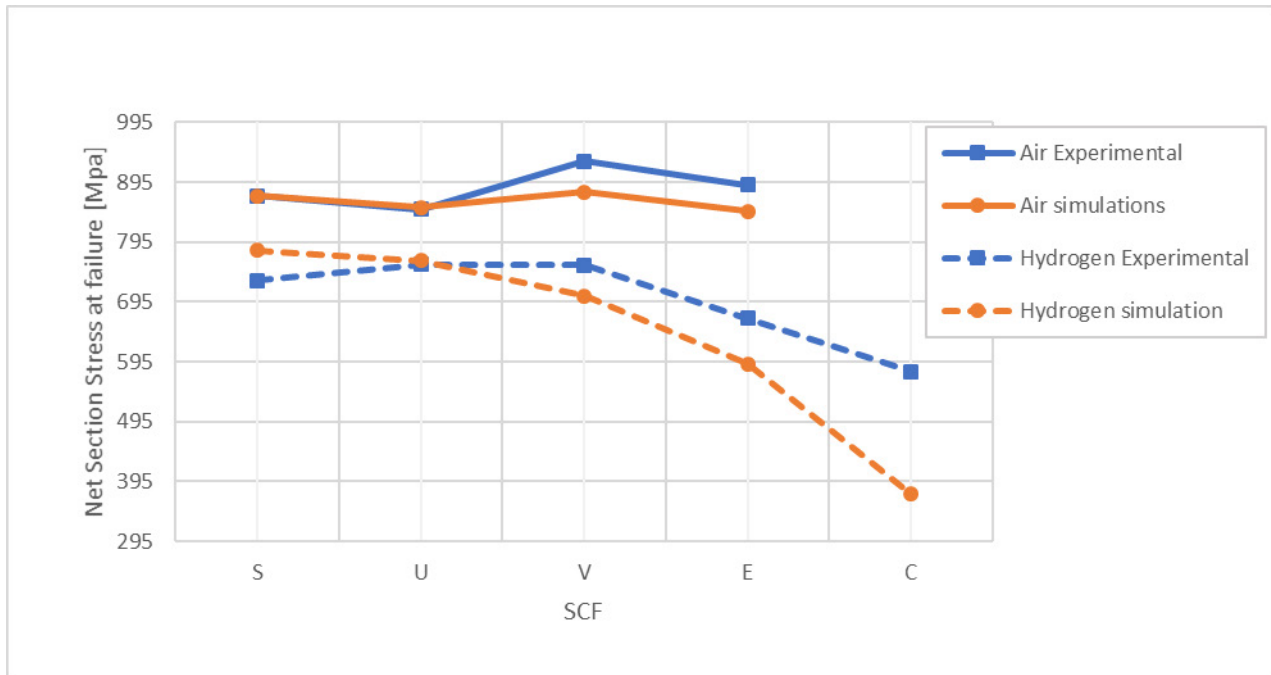


Figure 14 Comparison of experimental results (blue) and numerical simulation (orange) for the air and CP conditions.

The initial calibration of the model to the air results clearly show a geometry effect to the cohesive elements. The maximum inherent cohesive stress described by the element needs to be increased with the sharpness of the notch, see Table 3. The cohesive law is of bilinear type with a 'stiffness' of $1,55 \cdot 10^{-3}$ MPa/mm.

Table 3 Initial cohesive stress and net section stress at fracture in the cohesive elements. With increasing sharpness of the notch, the cohesive element needs a geometry correction of the initial cohesive stress.

Geometry	Initial cohesive stress in CZE MPa	Net section stress at failure MPa
Smooth	872	873
U-notch	1359	854
V-notch	1787	878
Eroded	1906	847
Crack	2250*	-

* Due to not valid experimental tests in air, the initial cohesive stress is set to 3,5 times the yield strength according to Tvergaard and Hutchinson¹.

3.1.3 Task 1.3: Structural integrity

The main objective of this task has been to investigate the fracture susceptibility and fracture behaviour of the interface between the clad (316L austenitic stainless steel) and the base material, by hardness testing and fracture mechanics testing. The fracture mechanics testing has been performed in air and in hydrogen charging condition on CT specimens in as received and in welded condition. The fracture mechanics work on the not welded specimens has been part of Lise Jemblies PhDs work, whereas the hardness measurements and fracture mechanics testing has been performed by SINTEF and also as parts of the master thesis work of Helena Bjaaland and Andreas Utvær and the internship candidate Martin Degos of the university Ecole des Mines in St Etienne.

The summary of all these results were presented at the Hydrogen & Metals conference in Ghent 29-31. May 2018, and the paper is available in the conference proceedings (see publication no. 38).

Material

Two different clad steel pipes were investigated, presented in Table 4 as Pipe A and Pipe B respectively, with the main difference being the presence of a nickel interlayer between clad and base material for Pipe A.

Table 4 Chemical composition (w%) and tensile properties of the investigated clad steels.

Pipe	Steel	C	Si	Mn	P	S	Ni	Cr	Mo	Rp _{0.2} [MPa]		Rm [MPa]
A	X65	0.07	0.13	1.48	0.007	0.0007	0.26	0.02	0.13	-		-
	316L	0.001	0.38	0.82	0.028	0.001	10.13	16.19	2.07	-		-
B	X60	0.076	0.38	1.38	0.006	0.0008	0.27	0.27	0.003	493		595
	316L	0.018	0.37	1.38	0.031	0.002	11.09	16.68	2.04	440		647

Samples for investigation of the interface microstructure prior to girth welding were extracted in the longitudinal direction of the pipes in as supplied condition. The interface microstructure of both samples is presented in Figure 15. For Sample A, the 30-35 μm thick nickel interlayer is clearly visible, while no carbide precipitates can be seen. Sample B displays a continuous area of carbide precipitates ($\sim 200 \mu\text{m}$ wide) on the clad side, attributed to carbon diffusion across the interface during production.

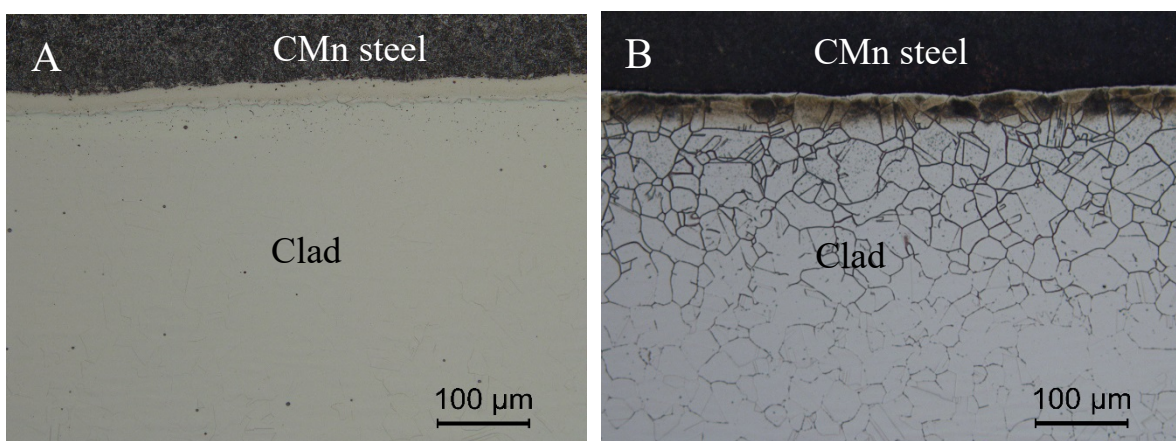


Figure 15 Interface microstructure in pipe A and B.

Figure 16 shows the interface area close to the girth welds for both pipes. The micrograph for pipe B indicates a tendency for micro-cracking along the interface on the clad side close to the weld metal. To mitigate micro-

cracks in the fracture mechanics specimens, laboratory welding in less constrained conditions was performed for pipe B.

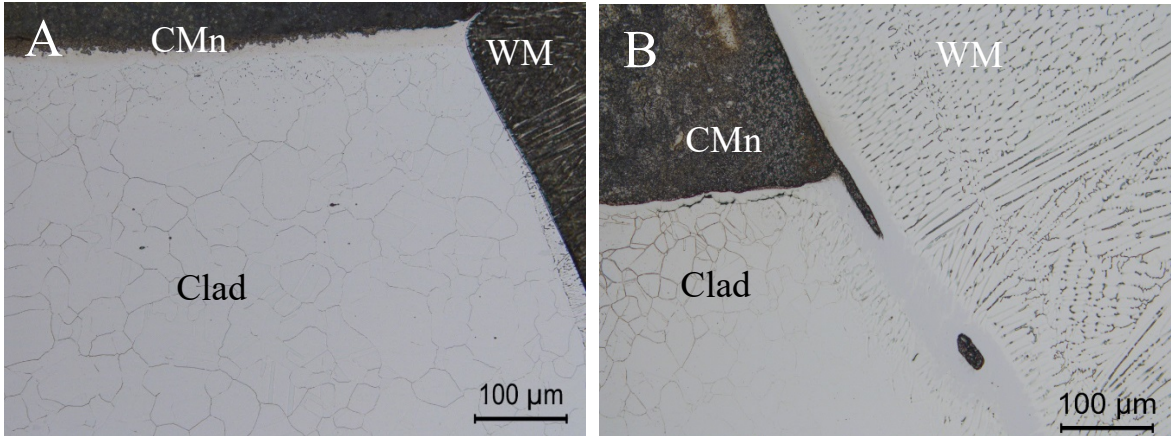


Figure 16 Interface microstructure after girth production welding of pipe A and B. For pipe B, a micro-crack can be observed on the clad side along the interface close to the weld metal.

Microhardness

Microhardness measurements applying HV 25 grams were performed across the interface, and adjacent to the interface on the clad side and in the CMn steel, as shown in Figure 17. On the CMn steel side the indentations along the interface were positioned a distance 45µm and ~820µm from the interface. The directions are indicated by the arrows in Figure 17 a. For the welded samples, the transversal indentations were positioned 300 and 700 µm from the triple point (TP) between the WM, clad and CMn steel as shown in Figure 17 b. Indentations were also placed along the heat affected zone close to the WM fusion line. The results for the indentations transversal and along the interface on both sides are presented in Figure 18 and Figure 19.

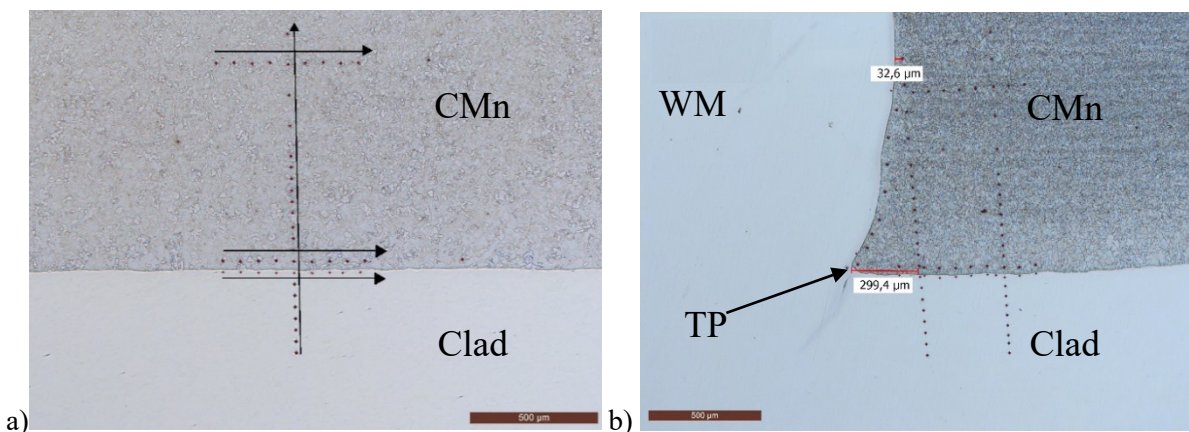
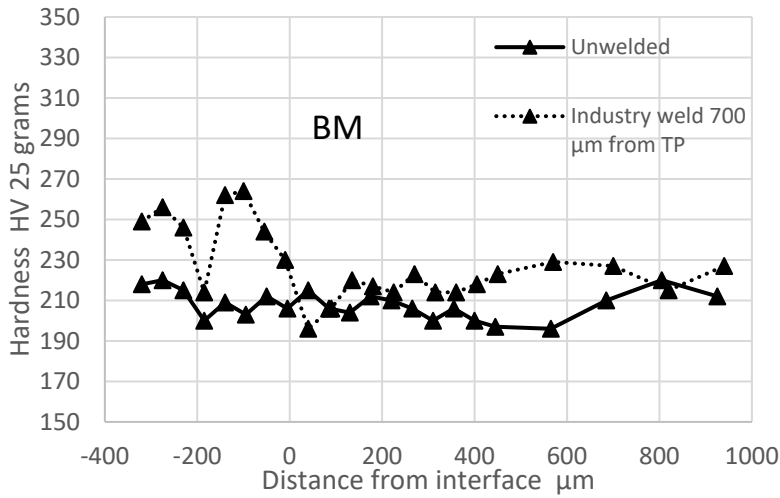
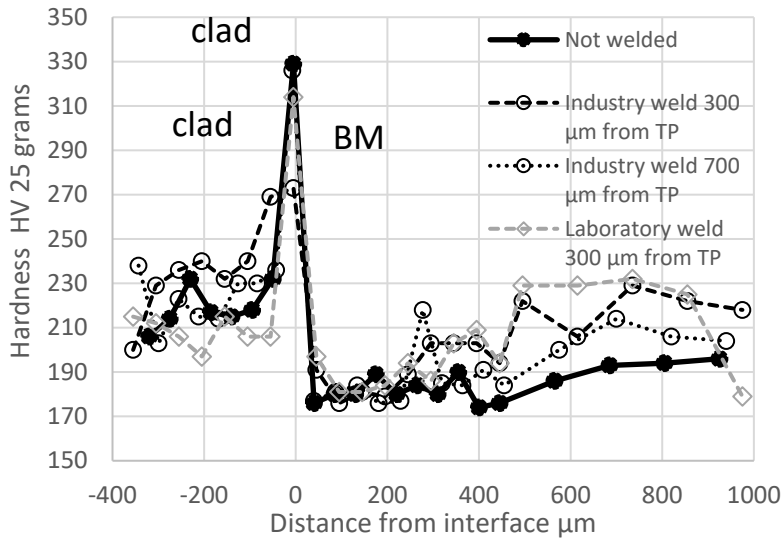


Figure 17 Microhardness indentations across the CMn steel and clad interface and along the interface on both sides of the interface. a) Not welded pipe, including arrows indicating the direction in which the indentations are made. b) Welded pipe, with indentation traverses 300 and 700 µm from the triple point (TP) and in HAZ along the weld metal fusion line.

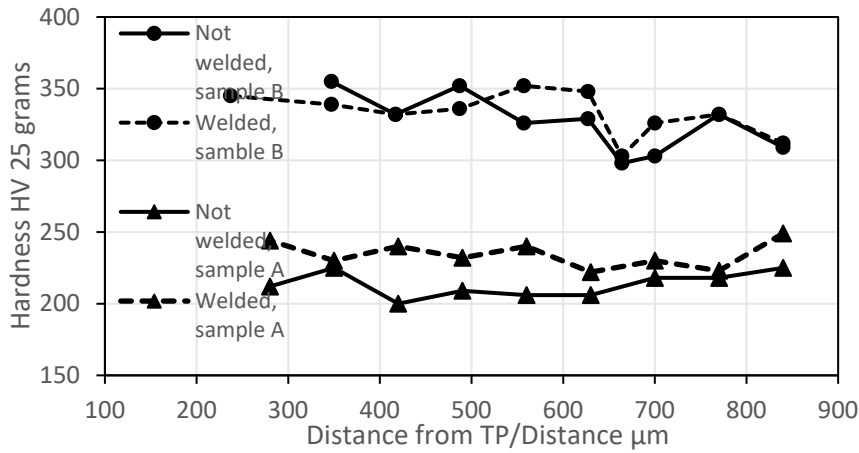


a)

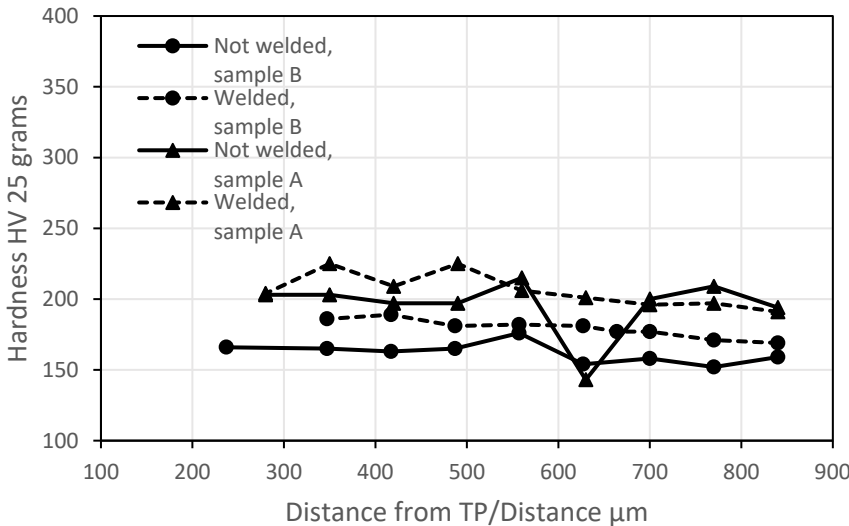


b)

Figure 18: Vickers microhardness profiles across the interface before and after welding a) Pipe A b) Pipe B, also including hardness indentations in laboratory weld (grey).



a)



b)

Figure 19 Hardness along interface a) Adjacent to the interface on the clad side b) 45 μm from the interface on the CMn steel side

As shown in Figure 18 b, the not welded Pipe B displays a hardness peak of 330 HV adjacent to the interface on the clad side and an abrupt drop in hardness adjacent to the interface on the BM side before a minimum of ~ 175 HV is attained. This is an indication that carbon diffusion across the interface takes place during production. After welding, the hardness peak is lower in the profile located 300 μm from the TP. This is however not reflected in Figure 19 a, which shows little hardness difference before and after welding on the clad side of sample B. The laboratory weld yields similar hardness as the industry weld. As shown in Figure 18 a, for Pipe A, no hardness peak is visible on the clad side adjacent to the interface prior to welding. After welding, there is a hardness increase on the clad side, but no peak close to the interface. Figure 19 b show that the hardness is generally higher in CMn steel close to the interface in pipe A, in contrast to plate B which is clearly lower due to carbon depletion during plate production. After welding there is a slight hardness increase in the heat affected zone (HAZ) on the CMn steel side for both pipes, see Figure 19 b.

Fracture mechanics testing

Constant load rate CT fracture mechanical testing was performed in air and under cathodic protection (CP), in order to establish the critical Crack Tip Opening Displacement – CTOD.

CT specimens were machined with the notch tip at the dissimilar metal interface to an initial crack length to width ratio a_0/W of 0.5, using electro-discharge machining (EDM), as it was deemed impossible to produce a fatigue crack propagating exactly along the dissimilar interface. For the welded specimens, the eroded notch was positioned along the interface, from the WM side, with the tip of the notch at the triple point between WM, clad and CMn steel. Details of the specimen geometry, dimensions and notch positions are given in Figure 20 a and b. Prior to machining, the specimens were lightly etched in 2 % Nital to better reveal the dissimilar interface. An example of a CT-specimen from a welded pipe is given in Figure 20 c.

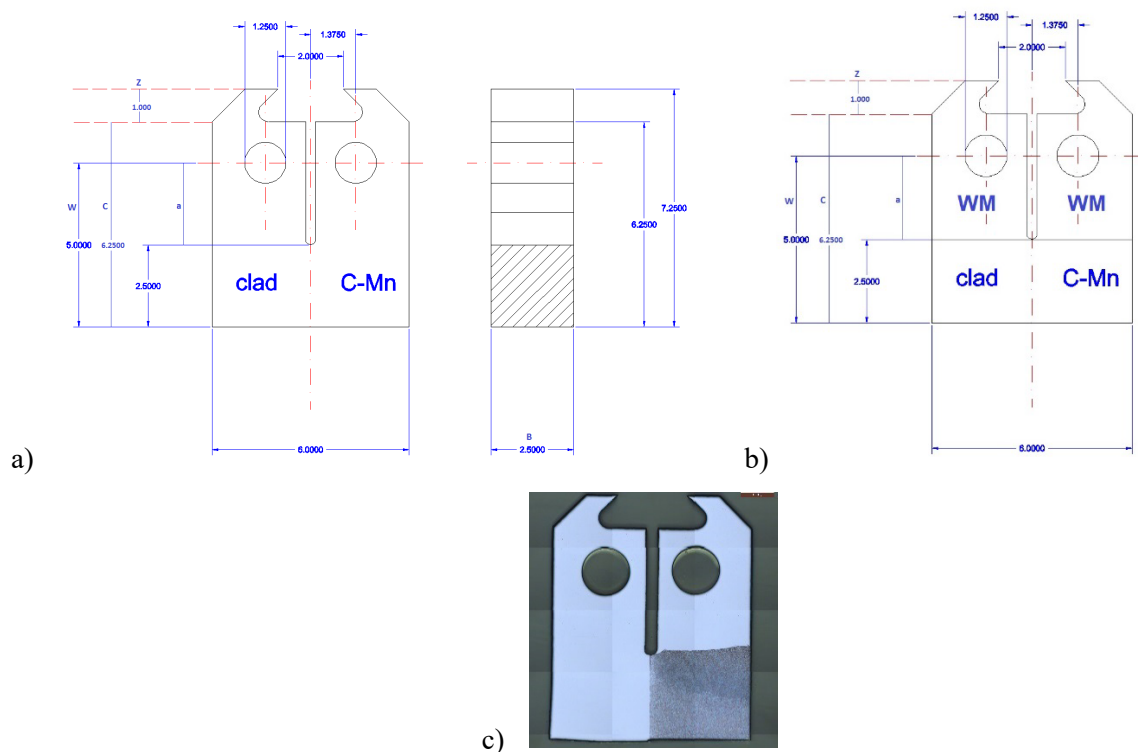


Figure 20: Compact tension specimen geometry, dimensions and material combinations, $W=5$ mm, $B=2.5$ mm, $a=2.5$ mm, $C=6.25$ mm, $z=1.0$ mm, notch radius= 0.15 mm. a) Not welded b) Welded. In the welded specimens, the notch tip is located at the triple point between weld metal, clad and CMn steel. c) Lightly etched CT specimen from welded pipe

Specimens from the C-Mn steel, with the notch parallel to and ~ 3 mm below the pipe surface was tested as reference. A constant loading rate of 0.7 N/min was applied, corresponding to a stress intensity rate of $6.8 \cdot 10^{-4}$ MPa $m^{1/2}/s$. This is in accordance with the work by Lee and Gangloffⁱⁱ on hydrogen assisted cracking of ultra-high strength martensitic steel, making the resulting fracture toughness independent of the loading rate. For testing in hydrogen environment, the specimens were immersed in a 3.5 % NaCl solution with an applied cathodic potential of -1050 mV_{SCE}. Prior to test initiation, the specimens were hydrogen pre-charged in the test rig for 24 hours at -1050 mV_{SCE} in a 3.5 % NaCl solution. All testing was performed at room temperature.

During testing, the load and the machine displacement were recorded. For testing in air, a machined clip gage, made to fit the small size of the specimen, was used to measure the Crack Mouth Opening Displacement (CMOD) at the knife edges. Due to the design of the fracture mechanical testing rig, it was not possible to use clip gages for testing under CP, where the specimen was immersed in a 3.5 % NaCl solution. Rather, the

average ratio between plastic CMOD (V_p) and plastic displacement (d_p), resulting from testing in air, was used to obtain the plastic CMOD under CP at the point of maximum load for determination of critical CTOD:

$$V_{p, CP} = \left(\frac{V_{p, air}}{d_{p, air}} \right) \cdot d_{p, CP}$$

The CTOD values at maximum attained load were determined according to standard BS 7448-1ⁱⁱⁱ. Fracture surfaces and fracture profiles were examined using a combination of light optical microscopy (LOM) and scanning electron microscopy (SEM).

The load - CMOD curves and the CTOD at maximum load for the two pipes reflect a difference between the pipes as well an influence of hydrogen and welding. Representative load-CMOD curves for pipes A and B are presented in Figure 21 a and b respectively.

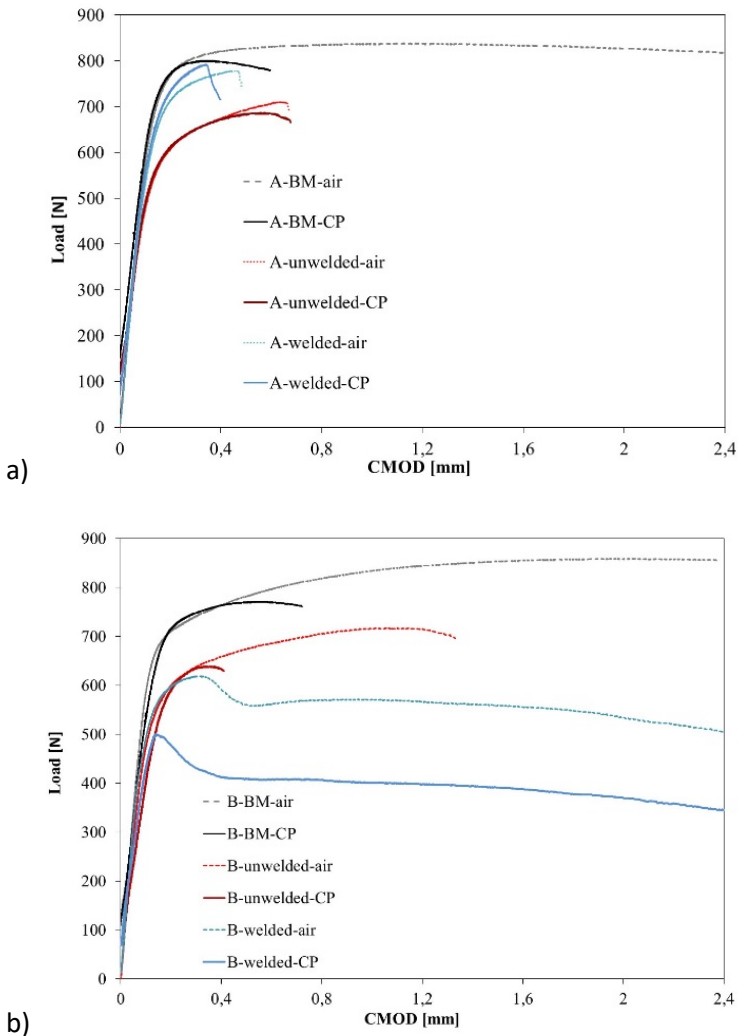


Figure 21 Representative Load-CMOD curves in air and CP a) Pipe A b) Pipe B

For both pipes, the load CMOD curves for the CMn steel reference specimens (black curves), show a clear reduction in CMOD (plastic deformation) when tested in CP. For the clad/steel specimens from Pipe A however, no influence of CP is observed. Welding increases the maximum load and reduces plastic deformation compared to the not welded specimens. For Pipe B, hydrogen clearly reduces the plastic behaviour

at maximum load for all types of specimen. Welding is further reducing the load capacity and the plastic deformation at maximum load.

The results in terms of CTOD (δ) at maximum attained load are plotted in Figure 22 for all specimens with clad. Weld specimen results are denoted with a W and plotted with red markers.

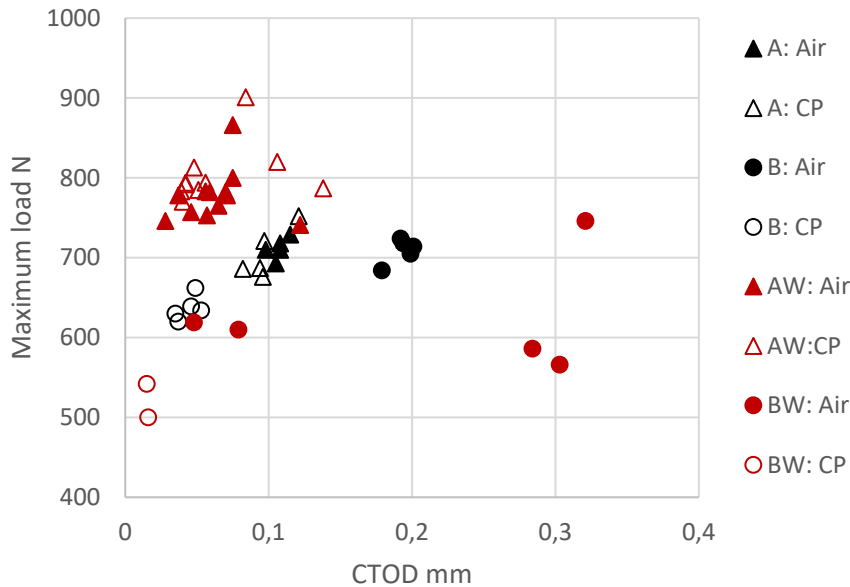


Figure 22 CTOD at maximum load for specimens with and without weld, in air and CP conditions

When comparing not welded Specimens A and B tested in air, B display a higher CTOD with no variation in terms of maximum attained load, indicating more plastic deformation prior to failure. In hydrogen charging conditions, the roles switch. The B specimens are reduced both with respect to fracture toughness and load capacity, while no influence of hydrogen is seen for the A specimens. The average CTOD value for the A specimens is 0,11mm in air and 0,10 in CP, and for the B specimens 0,19 mm in air and 0,04 mm in CP, representing a 79% fracture toughness reduction.

For the welded specimens AW and BW, the following main trends are observed: AW has the highest load capacity of all specimens, and there is no influence of hydrogen on neither load capacity nor CTOD. The average fracture toughness is however as low as 0,06 mm both in air and CP conditions. For the BW specimens tested in air, there is huge scatter in CTOD results. The load capacity is however 20% lower in average compared to the AW specimens. The minimum CTOD value is 0,05 mm and the maximum 0,3 mm. The two BW specimens tested in CP are clearly the lowest with respect to both load capacity and fracture toughness, obtaining a CTOD as low as 0,015 mm.

In order to verify the influence of welding and hydrogen on the fracture morphology, selected specimens were investigated in SEM. The results appeared consistent for all parallel tests. For Pipe A, all specimens (including not welded, welded, air and CP) revealed a dimpled morphology, indicative of ductile fracture (Figure 23 a-b). This was the case also for the not welded B-specimens tested in air. However, all other B-specimens had a brittle fracture appearance. The fracture surface of not welded B samples revealed a distinct multifaceted appearance, indicative of cleavage fracture, followed by a quasi-cleavage fracture morphology, see Figure 23 c-d. For the welded B specimens, the first part of the fracture surface reveal more intergranular fracture (Figure 23 e-f and Figure 23 g-h). The brittle fracture morphology for the presented pipe B specimens corresponds to the loss in ductility observed for two of the B specimens after welding and for all B specimens tested in CP, as quantified by the lowered CTOD values.

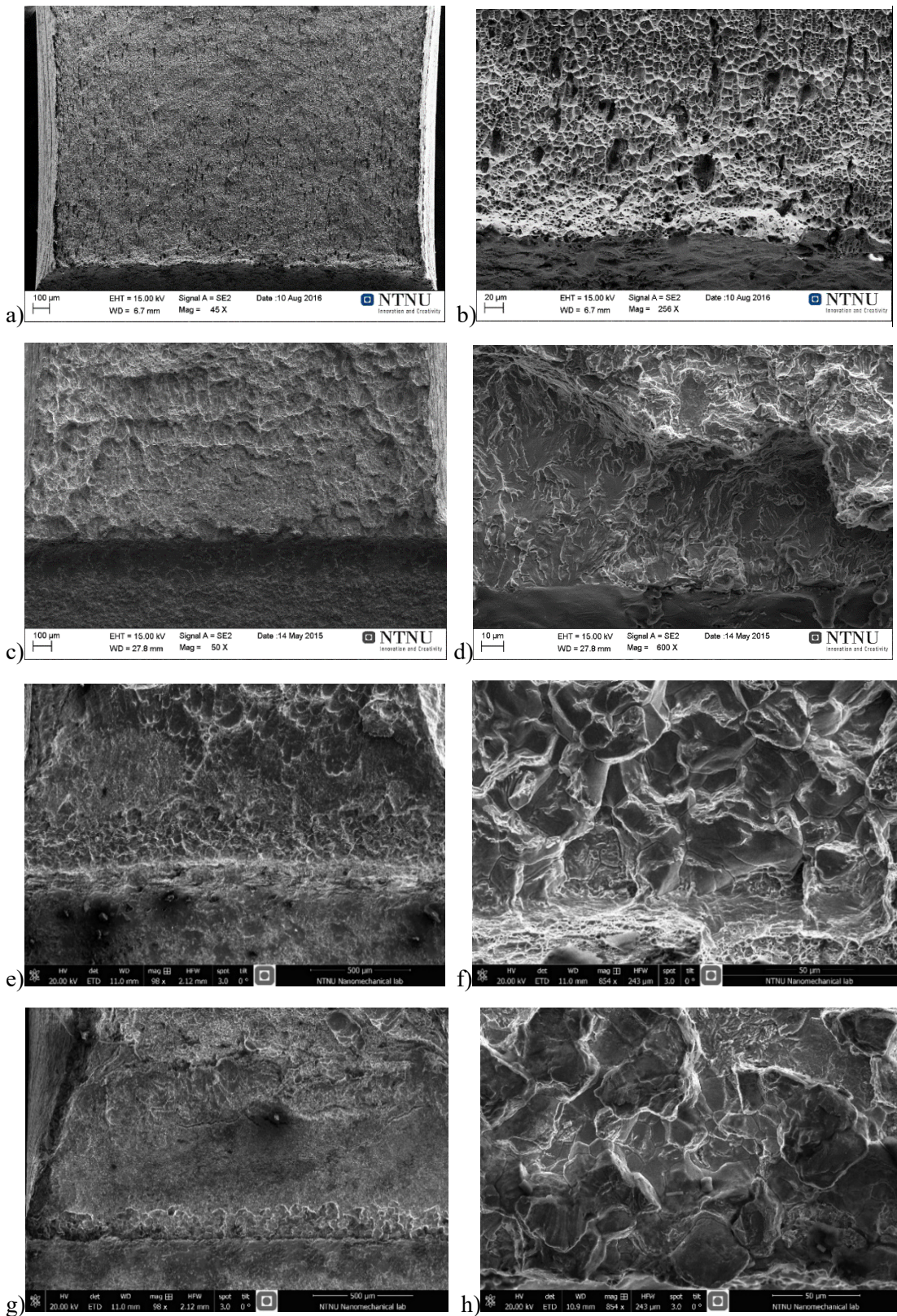


Figure 23 Fracture surfaces of CT specimens from welded pipes after testing a-b) Pipe A specimens tested in air c-d) Not welded Pipe B specimens tested in CP e-f) Welded Pipe B specimens tested in air g-h) Welded Pipe B specimens tested in CP

In order to determine the crack path, fracture surface profiles of selected specimens were examined by light optical microscopy. Micrographs of the first part of representative fracture paths are shown in Figure 24, with the fracture path in the vertical direction. In all Pipe A specimens, the crack propagated mainly along the CMn steel-Ni interface, slightly into the Ni-interlayer, as pictured in Figure 24 a. For the B specimens, the crack path shifted between the dissimilar interface and the CMn steel adjacent to the interface, with the crack propagating slightly more into the CMn steel for the specimens tested in air. It is however a clear difference in the crack path location between the not welded and welded specimen. As shown in Figure 24 b and c, the first part of the crack path is located on the clad side in the welded specimens (both air and CP), whereas the first part was on the CMn steel side in the not welded specimen, see Figure 24 d.

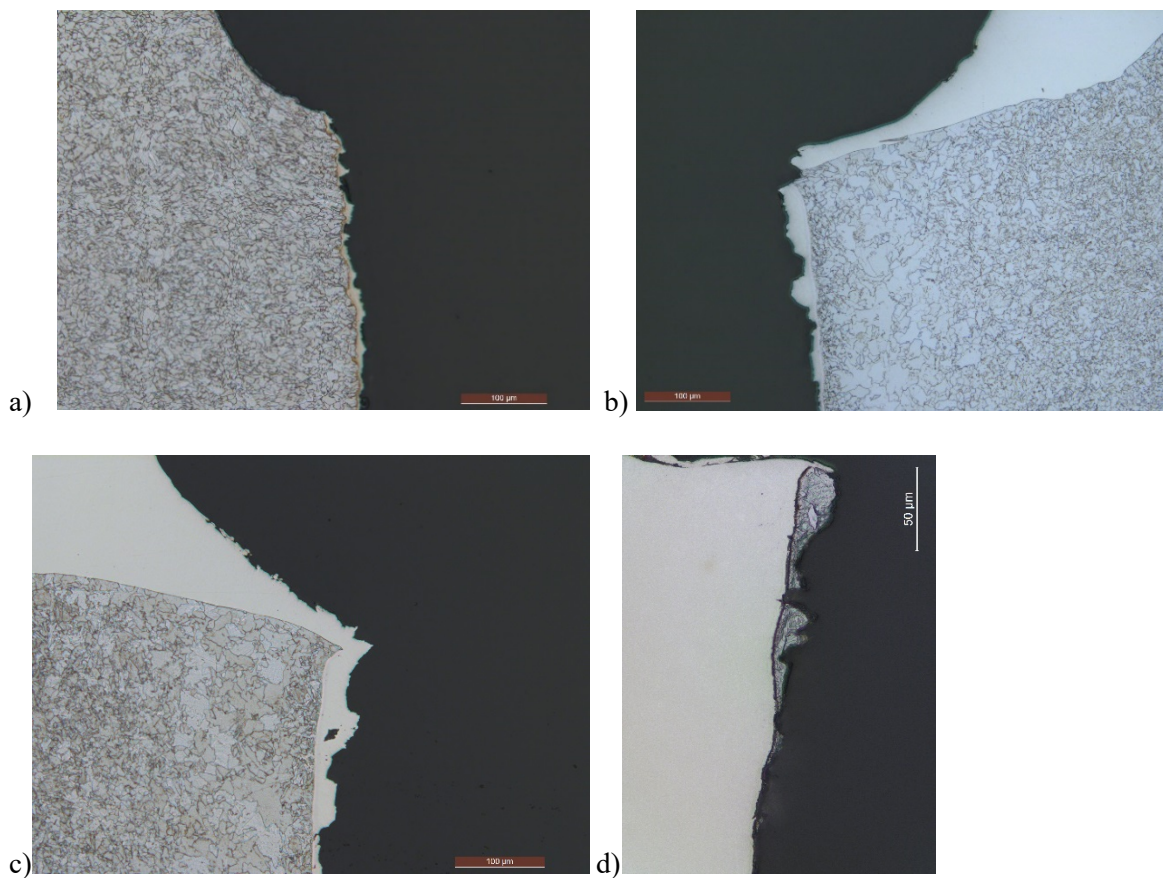


Figure 24 Location of the first part of the fracture in CT specimens a) Welded Pipe A specimen tested I air- fracture located in Ni interlayer b) Not welded pipe B specimen tested in air – fracture located in clad c) Welded Pipe B specimen tested I CP – fracture located in clad d) Not welded pipe B, tested in CP – fracture located in CMn steel.

For the not welded specimens, the results reveal a significant influence of material combination on the fracture resistance. For the specimens tested in air, the CTOD values for pipe A are ~ 45 % lower compared to pipe B. Commercially pure nickel yields at about 180 MPa ($R_{p0.2}$), well below the yield limit for steel, also considering softening due to decarburization in the CMn steel adjacent to the interface. Thus, the Ni-interlayer represents a soft zone, preferable for crack propagation, consequently lowering the fracture toughness. Hydrogen charging conditions dramatically lowers the fracture toughness for the B specimens, caused by a shift from a ductile to brittle fracture mechanism. Hydrogen degradation of the CMn steel is consistent with the general knowledge of hydrogen effects on pipeline steels and reflected in the load vs CMOD curves for pure CMn

steel. The A specimen results did not change significantly, since the fracture still propagated in a ductile manner in the soft Ni-interlayer.

Welding itself causes a change in the load capacity as well as fracture toughness. For the A specimens, there is a clear increase in load capacity and a ~50% decrease in fracture toughness. This was initially somewhat surprising, since the fracture path also after welding is in the Ni-interlayer. The soft thin Ni interlayer is confined in a stronger and less ductile material (hardened by welding) which gives increased strength and thus an increased localization of the plastic deformation in the Ni-interlayer, reducing the fracture toughness, even if the fracture mechanism is still ductile. Since fracture takes place in the Ni-interlayer, no significant influence of hydrogen is observed.

For the B specimens, the load capacity after welding is clearly reduced, and the lowest CTOD values (in air) are almost 80% lower compared to the results for the not welded case. The fracture initiates on the clad side in an intergranular manner, and resembles the micro cracks observed in pipe B after production welding. It can be assumed that welding introduces residual stresses that make these specimens prone to fracture initiation in the very hard, carbide enriched zone. The further lowering of load capacity and CTOD when testing in CP, is likely related to hydrogen trapped at the carbides lowering the cohesive strength at the grain boundary even further.

In sum, a Ni interlayer is clearly preferable in clad steel with respect to avoiding influence of hydrogen on fracture toughness of the clad/pipe interface, both in not welded and welded condition.

3.2 WP2 Material and process modelling (Hallvard Fjær, IFE, Xiabo Ren, SINTEF)

3.2.1 Task 2.1 Weld arc modelling

There has been very little activity on welding arc modelling in Norway. This meant that the work in this work-package literally started from scratch. The main motivation for this modelling was to quantify the heat-input from the welding arc to the base material more accurately. The heat source used in WELDSIM assumes a geometrical distribution of a certain amount of heat, but with little evidence in the form of a mathematical model of the physical phenomena to back it up. An additional complication is added due to hyperbaric conditions.

Welding arc modelling is a complex task involving several physical phenomena. The model geometry is seen in Figure 25 below.

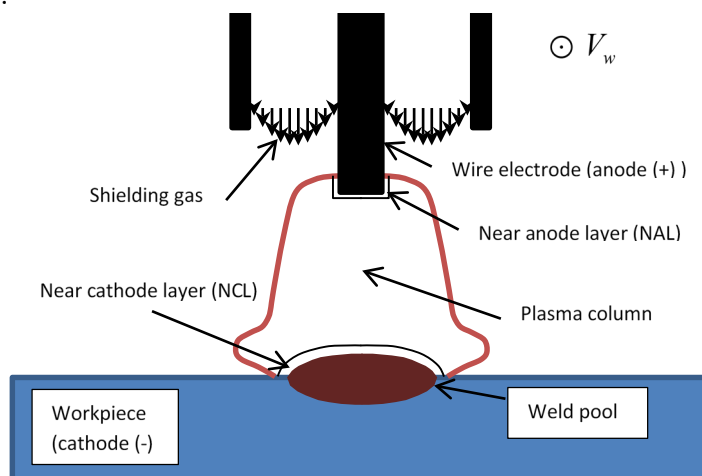


Figure 25: A schematic view of gas metal arc welding.

From Figure 25 we see that the modelling domain is highly non-uniform with respect to the materials involved. The welding process depicted in Figure 25 is gas metal arc welding (GMAW). The dominant physical phenomena are not the same throughout the arc. For this reason, we divide the modelling domain into five sub-domains characterized by their leading physical phenomena.

- 1) The wire electrode (anode). During welding this will melt, and droplets of molten metal will fall into the weld pool.
- 2) The near anode layer (NAL), highly exaggerated in Figure 1. The NAL interface contributes 1-2 V of the total voltage.
- 3) The arc plasma. This part is treated as a fluid and we need data for pressures up to 400 atm. These were not known at the start of the project. The voltage across the plasma is in the order of 10 V. Gas tungsten arc welding (GTAW) is characterized by a hot core plasma arc. GMAW however, is characterized by a cold core plasma arc. This is explained by the presence of metal vapor from the electrode.
- 4) The near cathode layer (NCL), highly exaggerated in Figure 1. There are models for the NCL, but they are developed for gas tungsten arc welding (GTAW). In GTAW the electrode is the cathode, it is cooled and consists of thoriated tungsten that does not melt. The NCL interface contributes 15-20 V of the total voltage. This voltage depends on the shielding gas used. When using Ar the voltage will close to 15 V the first ionization voltage.
- 5) The weld pool. The surface of the weld pool is an unknown.
- 6) The workpiece (cathode). Data is known.

Our first attempt in modelling the GMAW heat source was to use the NCL model developed by M. S. Benilov (University of Madeira) and A. Marotta. In this model the heat flux, $q_c = q_c(U_c, T_w)$, and current density, $j = j(U_c, T_w)$, is calculated at the workpiece interface. The NCL voltage drop is U_c and the workpiece surface temperature is T_w . A non-linear surface heating can be formulated to determine the total heat entering the workpiece (Fe) from the NCL.

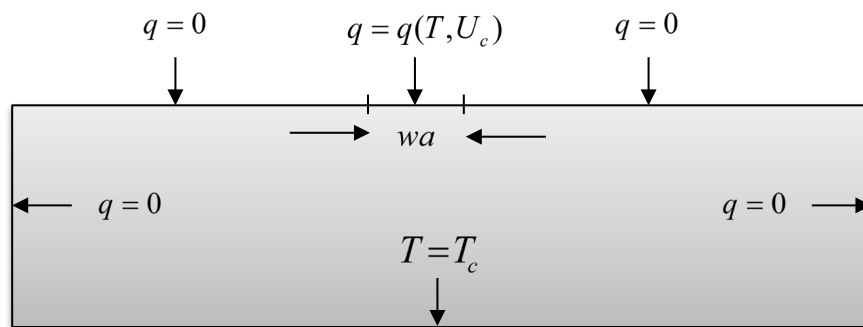


Figure 26: Boundary conditions used to solve the non-linear surface heating problem. Length and thickness of workpiece is 5 cm and 1.5 cm respectively. The initial arc attachment with, wa , is 1.5 mm at ambient pressure 1 atm and 1 mm at ambient pressure 20 atm.

We used COMSOL Multiphysics to solve the energy conservation with the added constraint equation

$$I = \int_{\text{top}} j(T, U_c) dS .$$

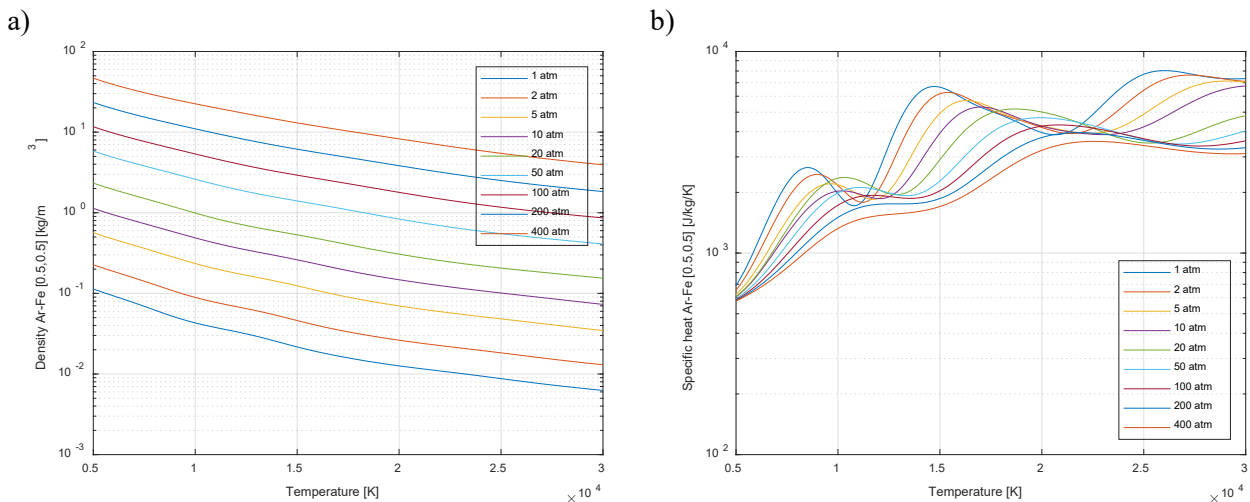
We fixed the total current to 200 A. The results obtained are shown in Table 5.

Table 5: The total current I , the NCL voltage drop U_c and the total heat transferred to the workpiece Q_c .

P [atm]	I [A]	U_c [V]	Q_c [W]
1	200	17.9	286
20	200	12.2	104

In Table 5 we observe reasonable NCL voltage drops, 17.9 V at 1 atm and 12.2 V at 20 atm. However, the total heat transferred to the workpiece Q_c are unreasonable. Assuming a total arc voltage of at least 20 V, we estimate the total heat generated in the arc to be $200\text{A} \cdot 20\text{V} = 4\text{ kW}$. The typical GMAW arc efficiency (fraction of the total heat transferred to the workpiece) is in the range of 0.8. We would therefore expect to obtain values of Q_c in the range 3.2 kW at 1 atm, but the results obtained are an order of magnitude lower. These results were communicated with Benilov, but no good explanation was obtained. We believe the most likely explanation is that Fe does not behave as a thermionic cathode. Thus, the Benilov and Marotta NCL model cannot be used on a Fe workpiece.

Realizing this we had to look for a more comprehensive and self-consistent GMAW model. We have put effort into formulating such a model and collect the material data necessary for solving it with respect to hyperbaric conditions. All models found in the literature treated atmospheric conditions only. For hyperbaric conditions we got very valuable assistance from A. B. Murphy at CSIRO (Australia). He has worked in this field for nearly 40 years. The thermodynamic and transport data needed in a comprehensive GMAW model are the mass density, the specific heat, thermal conductivity, electrical conductivity and the viscosity of the arc plasma for temperatures in the range [300 K, 30000 K], pressures in the range [1 atm, 400 atm] and compositions ([Ar, Fe] mole fractions). Data These data are not measured but are calculated based on a kinetic theory model. In Figure 27 we present a data set for the composition [0.5, 0.5].



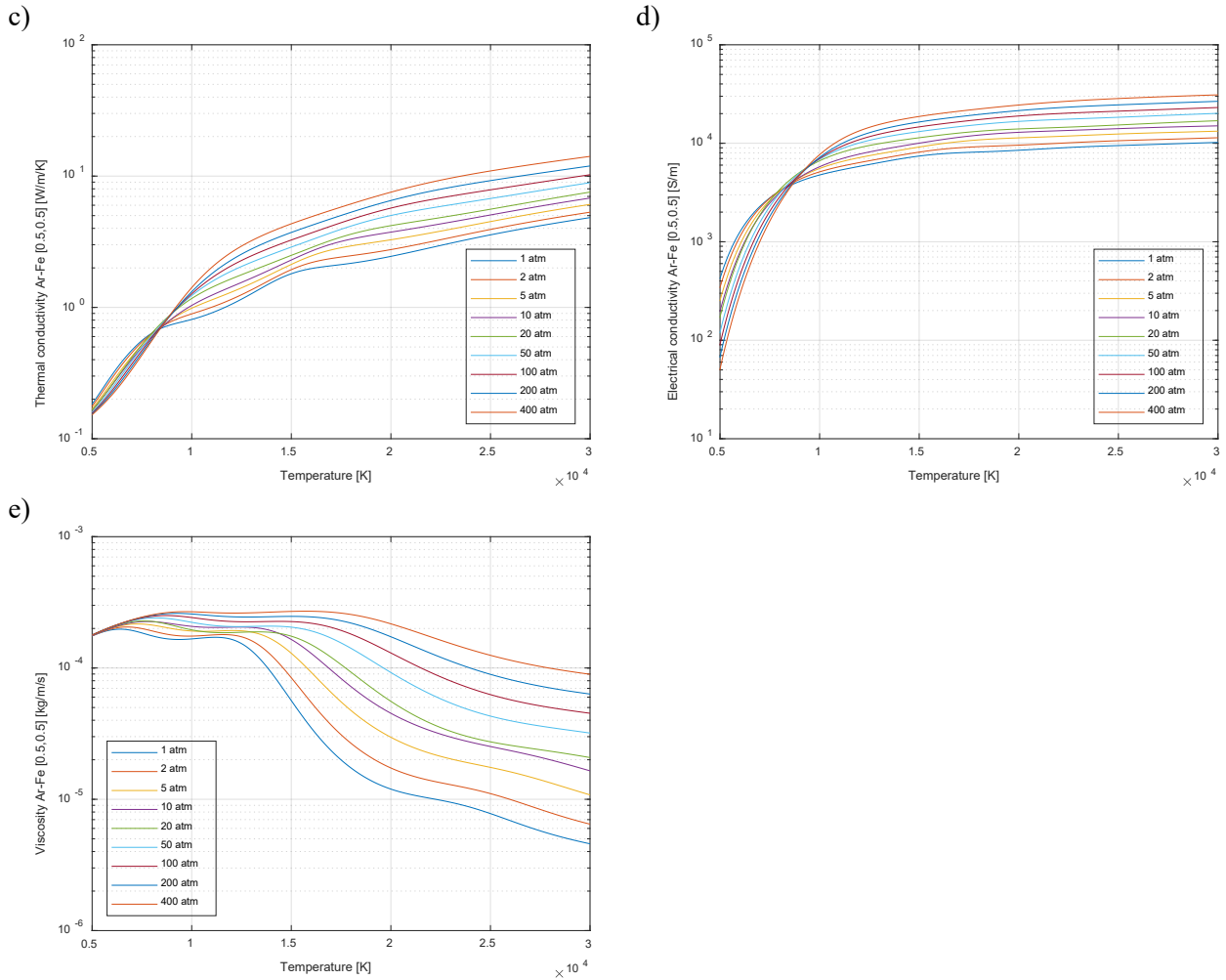


Figure 27: Thermodynamic and transport data for a plasma of mole fraction mixture 0.5Ar and 0.5Fe. a) Density, b) Specific heat capacity at constant pressure, c) Thermal conductivity, d) Electrical conductivity, e) Dynamic viscosity.

It is of interest to see how the assumption of incompressible and laminar flow is satisfied as we go to higher pressures. Assuming a plasma velocity of 250 m/s and plasma arc of length scale 1 cm we obtain the Mach number (M) and Reynolds number (Re) seen in Figure 28.

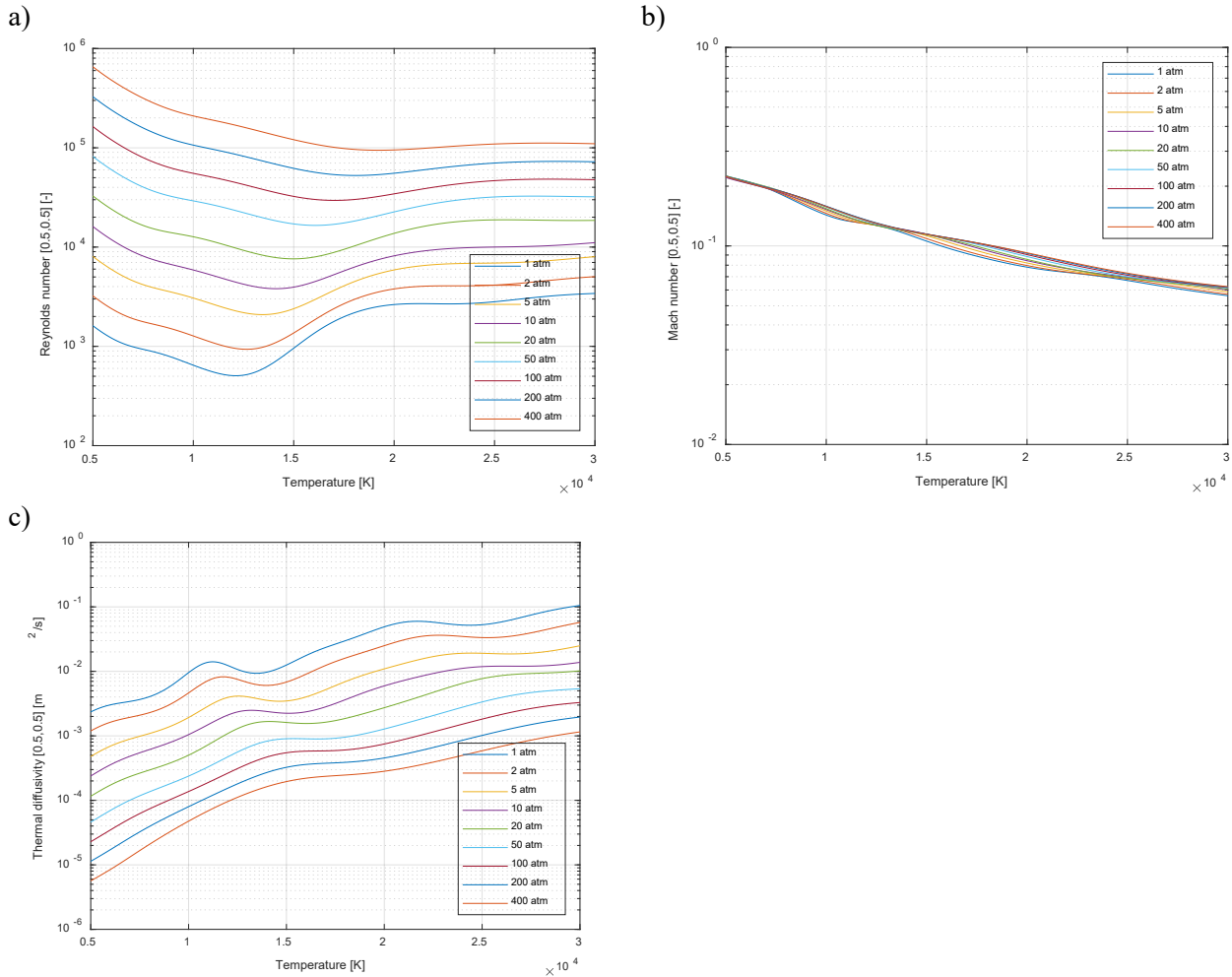


Figure 28: a) The Reynolds number for the plasma arc, b) The Mach number for the plasma arc, c) The thermal diffusivity of the plasma arc.

It is reasonable to assume laminar flow with Reynolds numbers up to 3000. From Figure 28 a) we see that this is satisfied for a pressure less than 5 atm. For pressures in the range 10-400 atm this is no longer satisfied, and we must expect a turbulent flow regime. Here this is derived on theoretical grounds, there is also experimental evidence for this. The need to include turbulent flow will of course add to the complexity of the modelling and we may get into unstable flow regimes.

From Figure 28 b) we see that the Mach number show very little pressure dependence and its value is below 0.16 for temperatures in the range 10000-30000 K. Thus, the incompressibility assumption seems to be satisfied in the pressure range 1-400 atm.

The thermal diffusivity of the plasma arc, α , is shown in Figure 28 c). We notice that going from 20 atm to 1 atm there is roughly a one order of magnitude difference in the thermal diffusivity. Going from 400 atm to 1 atm there is roughly a two order of magnitude difference in the thermal diffusivity. This indicates that the thermal properties in the arc plasma changes more rapidly (per atm) from 1 to 20 atm than from 20 atm to 400 atm.

There is an energy leak from the plasma arc through radiation. This phenomenon is also strongly dependent on the ambient pressure. Mr Y. Cressault of University of Toulouse kindly provided us with these data. In Figure 29 we see the net radiative emission coefficient in the pressure range 1-400 atm. We notice that the net radiative emission coefficient increases with pressure. At a pressure of 400 atm it is nearly three orders of magnitude higher than at 1 atm. This would indicate a cooling effect on the plasma arc. However, this effect will partly be compensated by a constriction of plasma arc.

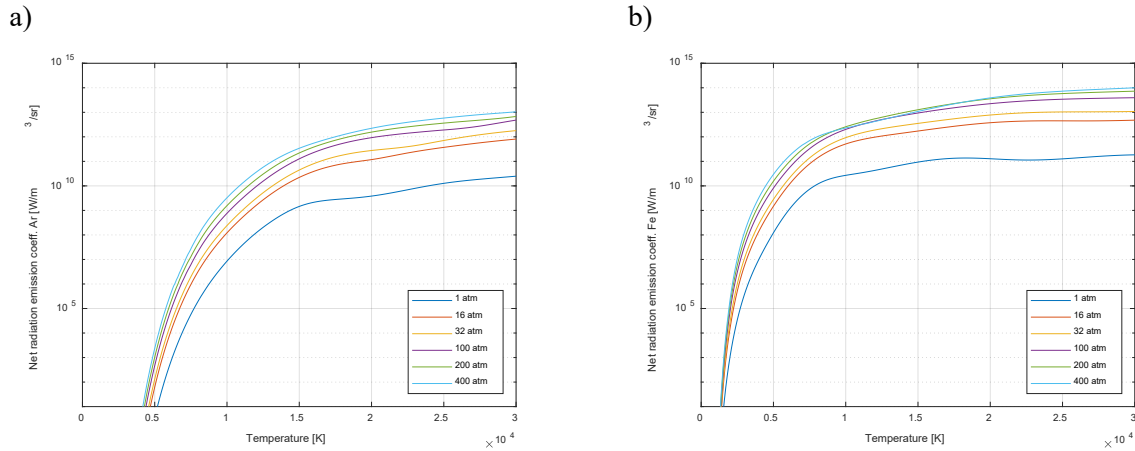


Figure 29: a) Net radiative emission coefficient for pure Ar, b) Net radiative emission coefficient for pure Fe. at ambient pressures 1 atm, 16 atm, 32 atm, 100 atm, 200 atm and 400 atm.

As pointed out previously the presence of metal vapour is a very important effect in MGAW. To include this effect in a simple fashion we must include a second species equation. The species equation for the mass fraction, Y_m , of the metal vapor.

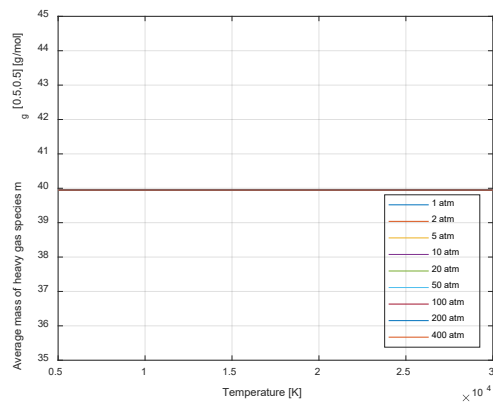
$$\begin{aligned} \nabla \cdot (\rho \mathbf{v} Y_m) = & \nabla \cdot \left(\rho \frac{m_g m_m}{M_m M} D_{mg}^x \nabla Y_m \right) \\ & + \nabla \cdot \left(\rho \frac{m_g m_m}{M^2} D_{mg}^x Y_m \nabla \left(\frac{M}{M_m} \right) \right) \\ & - \nabla \cdot \left(\rho \frac{m_g m_m}{M^2} D_{mg}^P \nabla (\ln(P)) \right) - \nabla \cdot \left(\rho \frac{m_g m_m}{M^2} D_{mg}^E \mathbf{E} \right) \\ & + \nabla \cdot \left(D_{mg}^T \nabla (\ln(T)) \right) + S_m, \end{aligned}$$

The coefficients of this equation are also dependent on the ambient pressure. In Figure 30 they can be found as functions of temperature and ambient pressure. These data were provided by A. B. Murphy from CSIRO Australia. The last term, S_m , in the above species equation is the metal vapor source term from the melting metal anode and metal droplets.

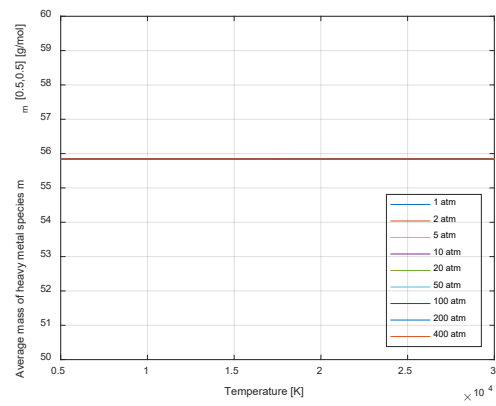
The implementation of a comprehensive and self-consistent model of MGAW is complex and way outside the scope of this project. We have through this project gathered necessary knowledge and data to attempt a detailed modelling approach in a possible follow up project.

For engineering purposes where, lower accuracy is expected we propose to use known arc efficiency, η_a , to quantify the total heat from the welding arc and resistive heating of the consumable in GMAW.

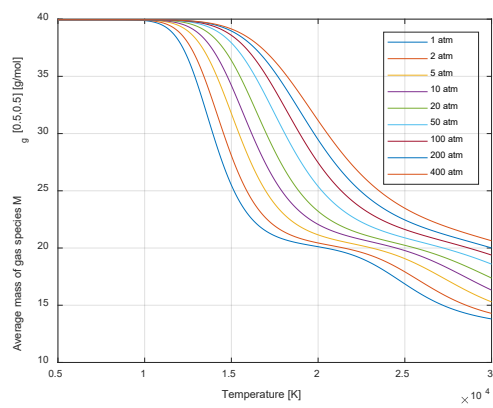
a)



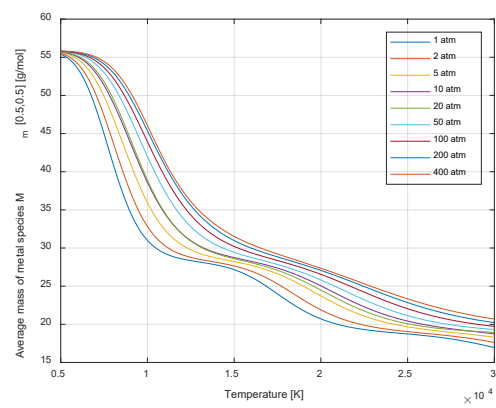
b)



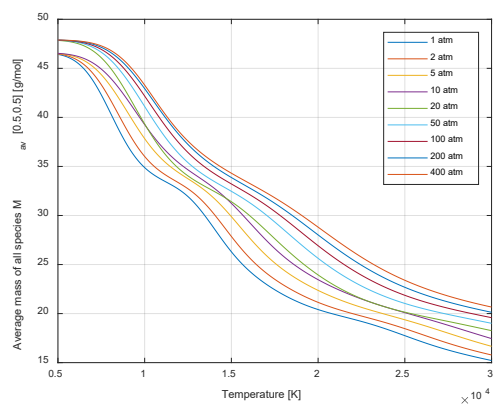
c)



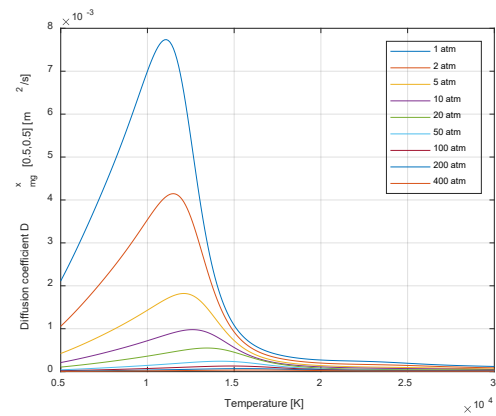
d)



e)



f)



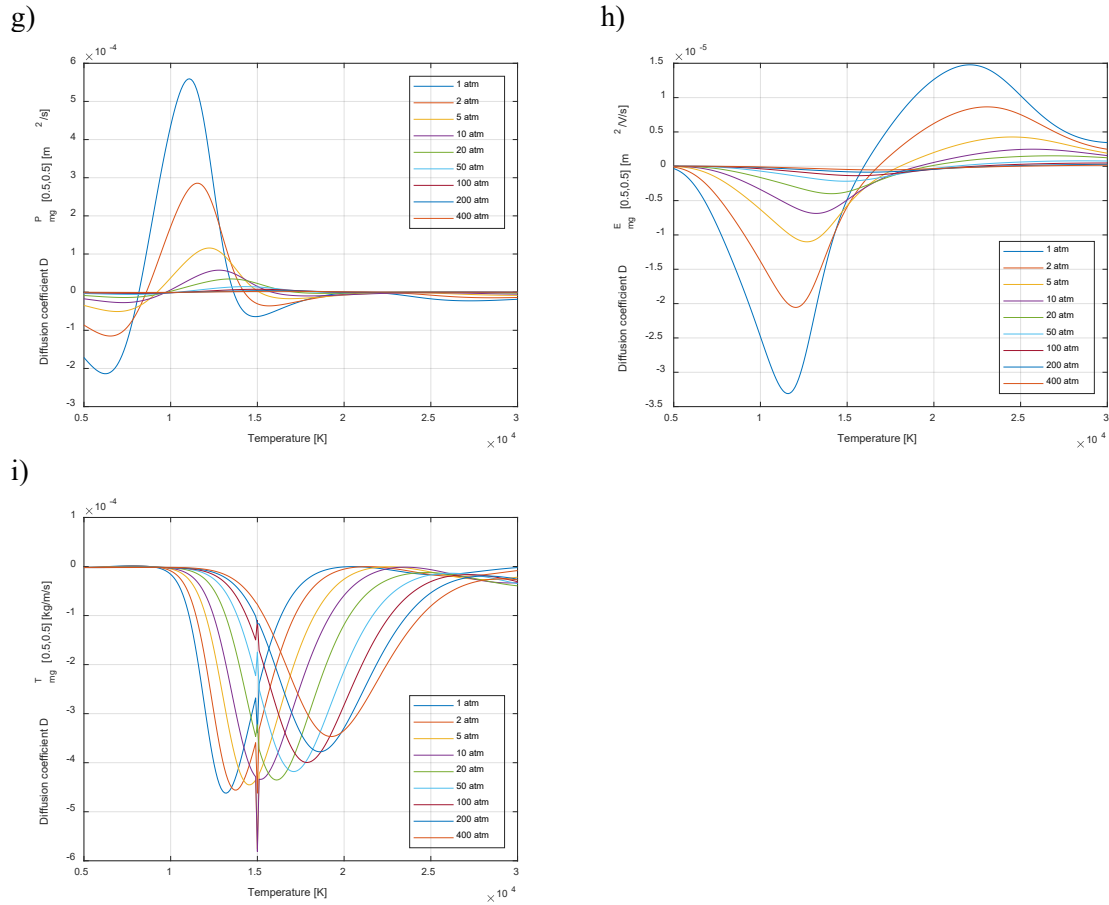


Figure 30: The parameters needed to solve the mass conservation equation for , a) the average mass of heavy shielding gas species, b) the average mass of heavy metal vapor species, c) the average mass of shielding gas species, d) the average mass of metal vapor species, e) the average mass of shielding gas and metal vapor species, f) the combined ordinary diffusion coefficient, g) the combined pressure diffusion coefficient, h) the combined electric field diffusion coefficient, i) combined temperature diffusion coefficient. There seem to be an anomaly in this data set. The author, A. B. Murphy, has been informed about this.

For a direct current electrode positive (DCEP) GMAW process a reliable value for the arc efficiency is 0.84. For a direct current electrode negative (DCEN) GTAW process a reliable value for the arc efficiency is 0.67. If we assume the total current to be I and the arc voltage to be V the total power delivered to the workpiece will be

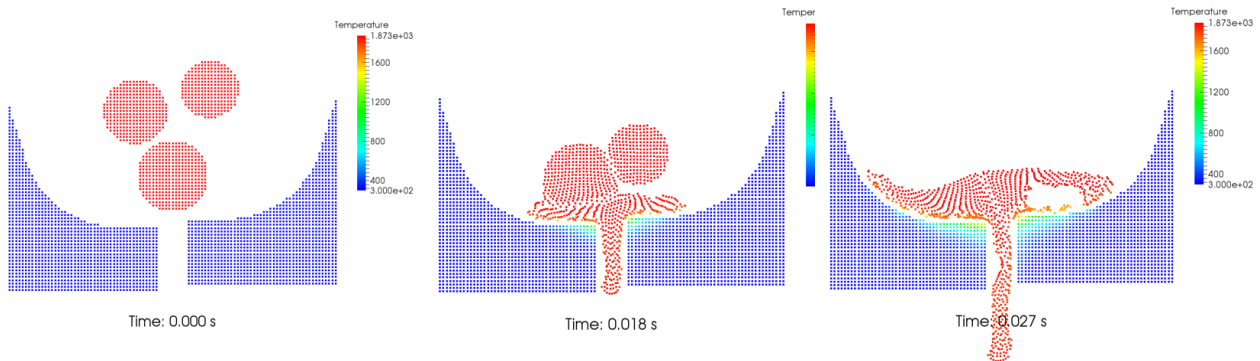
$$P_w = \eta_a VI.$$

For the heat flux distribution, we suggest a constant distribution over an elliptical shape with an area, A , equal to the cross-sectional area the electrode, A_{el} , multiplied with a factor κ . A reasonable range of κ is 9-25. The eccentricity and area, ε and $A(\varepsilon)$, of the ellipse are tuning constants. The surface heat flux associated with the welding can then simply be expressed as

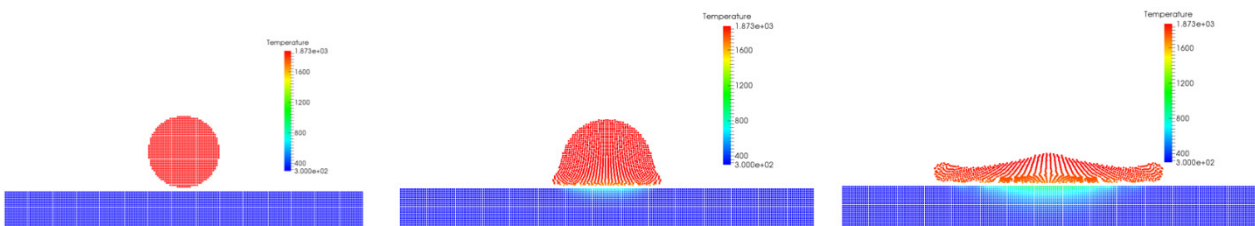
$$q_s = \frac{P_w}{A(\varepsilon)} = \frac{\eta_a VI}{A(\varepsilon)}.$$

3.2.2 Task 2.2 Weld pool modelling using SPH

Smooth Particle Hydrodynamic (SPH) based modelling of flow behaviour of welding molten pool has been developed. The flow behaviour of molten pool can influence the formation of weld bead profile after solidification, which in turn will affect mechanical performance of weld joint. The simulation can be used to optimize the welding parameter in terms of improved mechanical properties. In the ROP project, two case studies have been studied, i.e., bead-on-plate and pipe root pass welding, as shown in Figure 31.



(a) Pipe root pass case



(b) Bead-on-plate case

Figure 31 Results of SPH-based welding pool modelling.

The work is published as a Conference paper:

"Modelling of Cold Metal Transfer Welding Process Using SPH", see publication no 31.

3.2.3 Task 2.3 Modelling of hyperbaric welding

The hydrogen diffusion model

The hydrogen diffusion model formulation in WELDSIMS has been revised. In the former version the effect of the phase change on the overall lattice concentration was neglected, and simple phase averaged values for the solubility and the diffusivity were used in the equations. This has led to a lack of mass conservation for hydrogen, and a far too high diffusivity in the case of a mixture of austenite and ferritic phases. In the new formulation a fixed total concentration of hydrogen is re-distributed between the phases when the phase change is taken into account at the start of a time step. The equation that describes the rate of change of lattice hydrogen from diffusion, trapping/de-trapping, the pressure gradients, and relative changes in the solubility is then solved for a *constant* phase composition during a time step.

If we express the lattice concentration on phase j as

$$C_{L,j} = \frac{C_L}{f_j + \sum_{k \neq j} f_k \frac{s_k}{s_j}} = \psi_j C_L ,$$

the lattice concentration is computed by solving

$$\begin{aligned} & \sum_j f_j \left(1 + \sum_{i=1}^n \frac{N_{T,j}^{(i)} N_L K_{T,j}^{(i)}}{(K_{T,j}^{(i)} \psi_j C_L + N_L)^2} \right) \frac{\partial}{\partial t} (\psi_j C_L) = \\ & \nabla \cdot \sum_j \left(f_j D_j \psi_j \nabla C_L + f_j D_j \psi_j C_L \left(\frac{\bar{V}_H}{RT} \nabla p - \frac{\nabla \psi_j}{\psi_j} - \frac{\nabla s_j}{s_j} \right) \right) \\ & + \sum_j \left(f_j \left(\sum_{i=1}^n \frac{N_{T,j}^{(i)} K_{T,j}^{(i)} \nabla E_{T,j}^{(i)}}{(K_{T,j}^{(i)} \psi_j C_L + N_L)^2} \right) \frac{N_{L,j}}{RT^2} \psi_j C_L \right) \frac{\partial T}{\partial t} \end{aligned}$$

An improved consistency of the model is illustrated by Figure 10 where the total content of hydrogen in a 1D test case, computed by different version of the model, is compared.

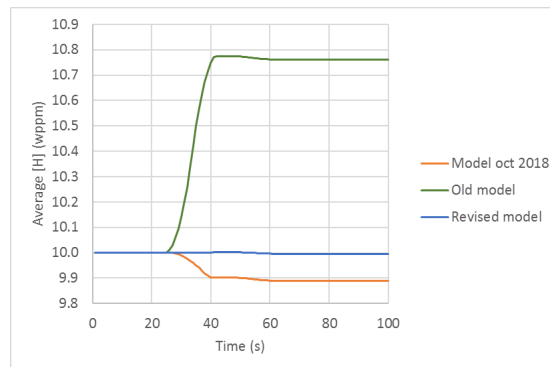


Figure 32 Comparison of the total content of hydrogen in a 1D test case computed by different versions of the hydrogen model in WELDSIM.

Simulation of the Tekken Y-groove test

As a part of WP3, several Tekken Y-groove tests were carried out in the workshop. While the dimensions of the weld specimens are shown in Figure 33, Table 6 identifies six of the welds from this work. H_0 refers to initial level of hydrogen in the weld. T_0 was the applied preheat temperature. All welds were made at atmospheric pressure. Dependent on the moisture in the shielding gas, two levels of hydrogen were added to the weld and fused metal, 10.3 wt% ppm and 5.0 wt% ppm. The low level was obtained without adding moisture to the gas, with the measured hydrogen in the weld originating from accidental absorption during storage of the welding wires. These test welds revealed that preheating was required to avoid cracking. With 5 ppm hydrogen introduced in the weld metal, preheating at 45°C was required. With 10.3 ppm this threshold temperature rose to 120°C.

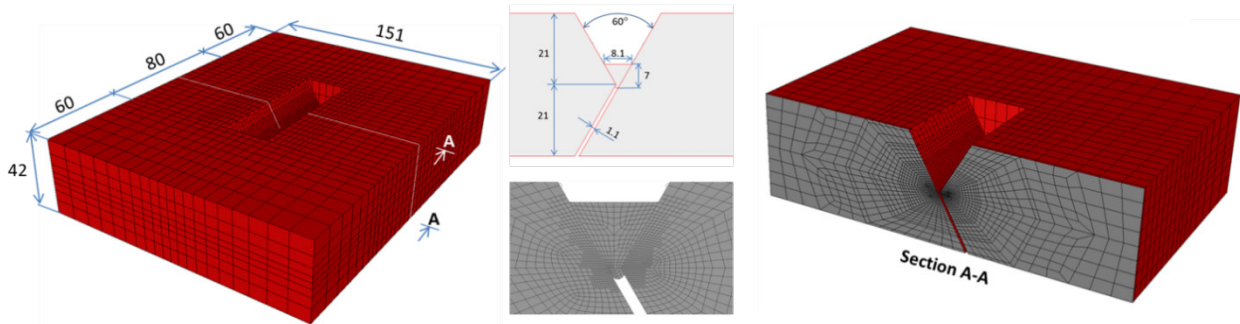


Figure 33 The computational domain of the Tekken y-groove test.

Table 6 Overview of the Tekken tests.

Test	H ₀ [ppm]	T ₀ [°C]	Comment
#07	5.0	-	Cracked after 1540 seconds
#10	5.0	45	No cracking
#09	5.0	69	No cracking
#08	5.0	120	No cracking
#11	10.3	69	Cracked after 180 seconds
#12	10.3	120	No cracking

Following the hydrogen trapping data that was reported at ISOPE 2018, the trap densities in the base material and in the weld metal was an estimated from former permeameter tests at SINTEF and the assumption that the trap energies corresponded to those identified in the tests at Kyushu University. Revised trap data values are shown in Table 7. Similar data for the base material (Table 8) and HBQ Coreweld (Table 9) were also derived.

Table 7 Trap data for heat-treated (HAZ) X70 pipeline steel.

Trap type	1	2	3	4
Trap energy	20.0	57.5	69.0	120.0
Trap density [cm ⁻³]	2.37·10 ²¹	1.0·10 ¹⁷	5.0·10 ¹⁶	7.0·10 ¹⁶

Table 8 Trap data for as-received (base material) X70 pipeline steel.

Trap type	1	2	3
Trap energy	17.0	53.5	68.0
Trap density [cm ⁻³]	1.9·10 ²¹	4.5·10 ¹⁶	9.0·10 ¹⁵

Table 9 Trap data for HBQ Coreweld.

Trap type	1	2
Trap energy	20.0	54.0
Trap density [cm ⁻³]	5.4·10 ²¹	8.1·10 ¹⁶

A 16.7 mm deep vertical hole was drilled into the plate from the bottom side and equipped with a thermocouple, as indicated by the photo in Figure 34. As the curves in the LHS part of Figure 34 (Test #07) displays, both the maximum value and the transient response were well reproduced in the model. With their positions identified by the labels M2-M4 on the RHS of Figure 34, three additional thermocouples were fixed to the

surfaces of Test #10. Measured temperatures are represented by dotted lines, calculated by continuous lines. Temperatures that represent the same position have identical colour. Computed temperatures were in good agreement with measured temperatures in the workshop.

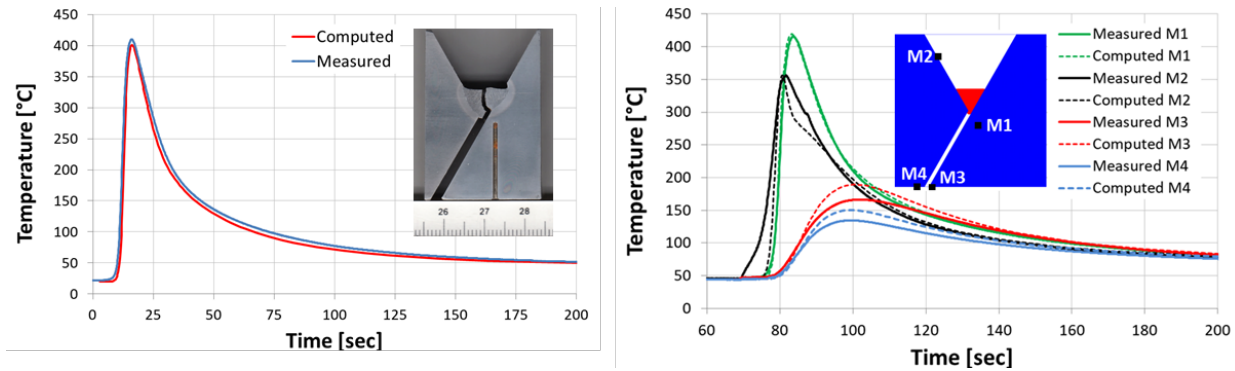


Figure 34 Computed and measured temperatures. Left: Test #07. Right: Test #10.

The computed microstructure is displayed in Figure 35. Because of the rapid cooling, the HAZ obtains a microstructure that consists of a mixture of ferrite, pearlite, bainite and martensite. The weld metal and the fused metal are dominated by bainite. The brittle martensite phase is located within a narrow circular band that encapsulates the fused metal. Outside this band, another, thicker band of bainite is present. The displayed phase distribution is the one achieved without using preheating. No significant changes were obtained for those cases that considered preheating between 45°C and 120°C.

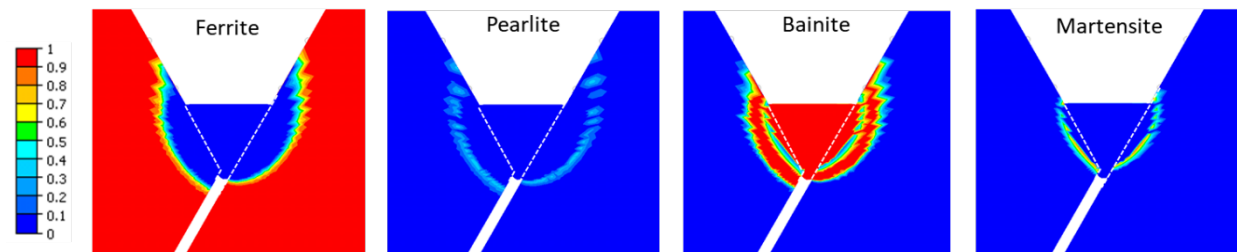


Figure 35 Computed microstructure. From left to right: ferrite, pearlite, bainite and martensite.

The transversal stress distribution obtained after welding are shown in Figure 36. While the upper part displays the stresses without use of preheating, the lower part shows transversal stresses based on preheating at 120°C. Each part is accompanied by an enlarged picture of the stress condition adjacent to the root of the weld. Obviously, preheating has a beneficial influence on the magnitude of the transversal stresses, which are lower compared to a case without preheating.

Even without moisture in the shielding gas, the Tekken test still cracked without use of preheating. For Test #07 a notch caused by lack of fusion was detected between the base metal and the weld metal. A stress concentration easily builds up in front of such a notch tip and makes the weld vulnerable to cracking. The starting point of the crack was determined to coincide with the notch tip. It then ran a short distance normal to the notch and into the weld before it proceeded vertically upwards through the weld centre. The crack path is seen from the photo that is inserted in the upper part of Figure 36.

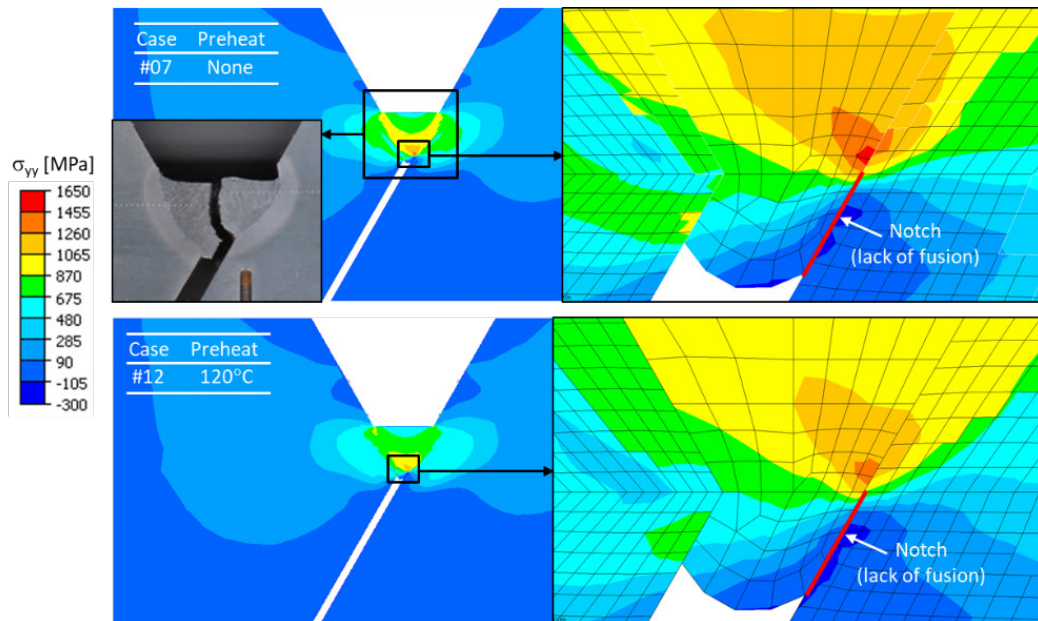


Figure 36 Computed transversal stresses for Test #07 (upper part, no preheating) and Test #12 (lower part, preheating at 120°C).

For Test #07, which cracked, the computed time-dependent evolution of each hydrogen concentration is shown in Figure 37. The positioning of the log points is identified from the upper right part of this figure. The behaviour of the curves reveals interesting aspects about the hydrogen diffusion model that has been developed in the project. Since the temperature is large during solidification and the microstructure consists of austenite, the concentration of hydrogen appears initially only as lattice hydrogen. Trapping in austenite was neglected. Trapping of hydrogen starts when austenite transforms to any of the other phases during cooling. For Test #07 this transformation occurred between 15 sec and 21 sec. A band of austenite in the HAZ, which coincides with the martensite band in Figure 35, was predicted to transform slower than austenite in the weld metal and the fused metal.

After about 20 sec there is a sharp decrease of lattice hydrogen and a corresponding rapid increase of trapped hydrogen. Because of the large solubility of hydrogen in austenite, the amount of hydrogen in the austenite band with delayed transformation is significantly larger than in the adjacent region. When also this austenite transforms, it feeds the adjacent region with hydrogen. Some of this hydrogen is trapped and some increases the lattice hydrogen concentration. As a result, the lattice and the total hydrogen in the two log points labelled #2 and #3 increases and obtains a local maximum in concentration. Because of its proximity to the band, the increase is larger for the former monitor point, which is also located in front of the crack tip.

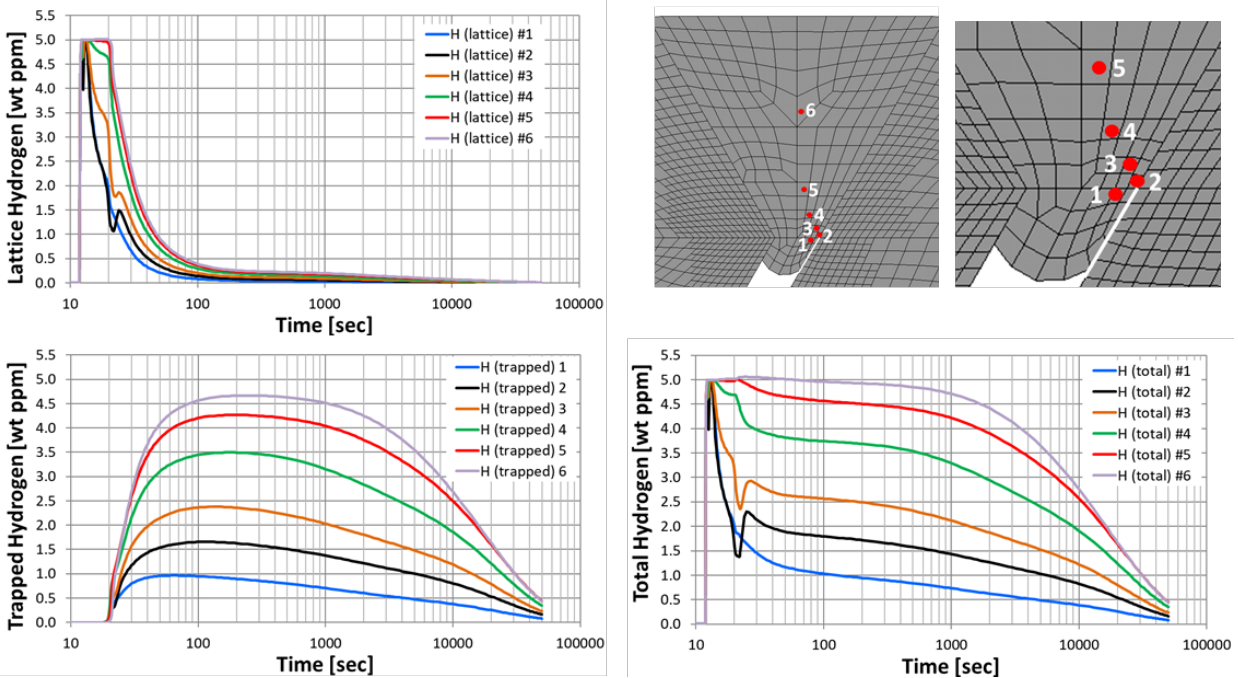


Figure 37 Local concentration of hydrogen versus time. Lattice (upper left part), trapped (lower left part) and total hydrogen (lower right part). Results obtained for Test #07.

Hydrogen embrittlement is generally considered to be influenced by an unfavourable combination of large level of hydrogen, large residual stresses and brittle microstructure in and adjacent to the weld. This makes prediction of a possible crack challenging. The effect of preheating on the resulting hydrogen and principal stress at the log point located in front of the crack tip are shown in Figure 38. Results from all six cases examined are included. While the LHS part displays results based on no moisture in the shielding gas, the RHS part shows the two cases exposed to humid shielding gas. The latter part does also include temperatures. The temperature in the legend identifies the preheat temperature. The hydrogen represents the total concentration of hydrogen at the log point. A higher initial temperature allows more hydrogen to diffuse through the HAZ and into the base metal.

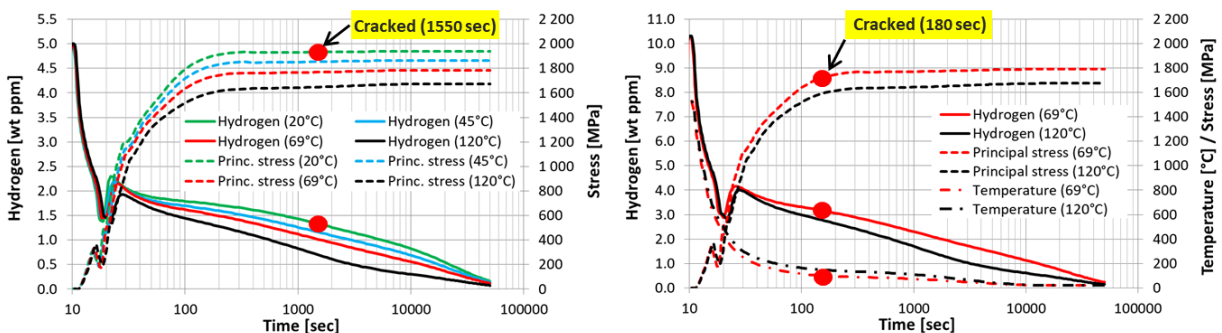


Figure 38 Principal stress and concentration of hydrogen (total) at a point in front of the crack tip. Left: Dry shielding gas. Right: Moisturized shielding gas.

As these curves show, the residual stresses are significantly influenced by the level of preheat. Because of the size of the components to be welded, and the fact that the complete structure is heated prior to the welding, preheating keeps the weld and the adjacent material hot for a relatively long time after welding. Diffusivity of hydrogen is more efficient at elevated temperatures, which means that the diffusion of hydrogen in the Tekken

test is also influenced by the level of preheat. For a field weld the constructions are typically larger, which means that provided preheat is quickly conducted to surrounding material with lower temperature. Preheating influences on the resulting residual stresses, less to decrease of hydrogen in such welds. However, for field welds in humid surroundings, preheating is often used to dry the metal surfaces.

Case Study on Repair Welding of Clad Pipes

Early in the project a case study was carried out to examine the influence of heat treatment (pre, interpass and post) on residual stresses, microstructure and decay of hydrogen in and adjacent to a multi-pass U-groove weld. Realistic process parameters and weld geometry was used. The computer results highlighted challenges related to hydrogen and welding of clad pipes. Austenitic AISI 316L was assumed as clad material to protect the ferritic X70 base material from corrosion. For simplicity, the material properties applied for the clad was adopted for the wire, which meant that the complete weld was filled by austenitic steel.

Figure 39 (a) shows the computed microstructure based on full heat treatment. It shows martensite (top, left), bainite (top, right), pearlite (bottom, left) and austenite (bottom, right). Computed stresses are shown in Figure 39 (b). It shows radial stresses (top, left), hoop stresses (top, right), axial stresses (bottom, left) and the von Mises stresses (bottom, right). Positive values are tensile.

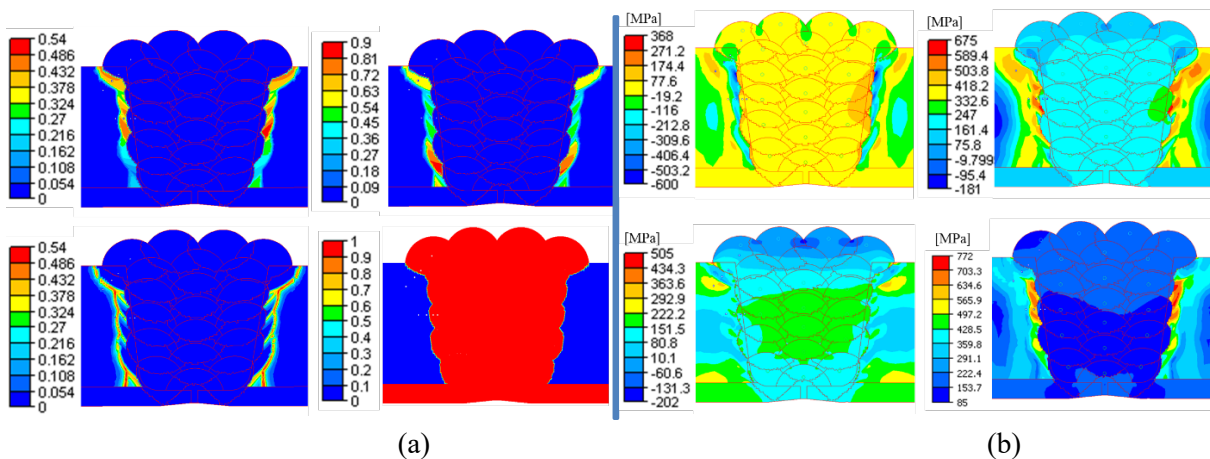


Figure 39 (a) Computed microstructure, (b) Computed stresses

While small differences were obtained for the microstructure and the residual stresses with and without heat treatment, hydrogen diffusion was significantly influenced. Contour plot of the lattice concentration obtained after completed heat treatment is shown on the LHS of Figure 40. Compared to a case without heat treatment, which is also included in this figure, the difference is obvious. Because of low diffusivity of hydrogen in austenite, as well as high solubility, the hydrogen content introduced in the weld metal (9 wt% ppm) decreases slowly. The weld metal provides hydrogen to the surrounding domains, the HAZ and the clad. Without heat treatment, the maximum value of lattice hydrogen, which located in the weld centre, was 5.7 ppm. Applying PWHT reduced the maximum value to 4.2 ppm.

In this study full heat treatment included both pre- and post-weld heating. The applied level of pre-heating did neither influence significantly on the hydrogen diffusion nor the resulting microstructure. Hardness in and adjacent to the weld was not computed.

Contour plots obtained for trapped hydrogen clearly demonstrates the benefit of heat treatment. Trapped hydrogen based on PWHT is shown on the LHS of Figure 41, while the corresponding plot with no heat

treatment is shown on the RHS. Both cases exhibit significant level of trapped hydrogen in the HAZ, but without heat treatment the band of trapped hydrogen adjacent to the fused zone is significantly wider and more dominating. The total level of hydrogen, which is obtained by adding the lattice hydrogen to the trapped hydrogen, clearly shows that for removal of hydrogen from the weld metal and the brittle crack susceptible HAZ, heat treatment proves to have large influence.

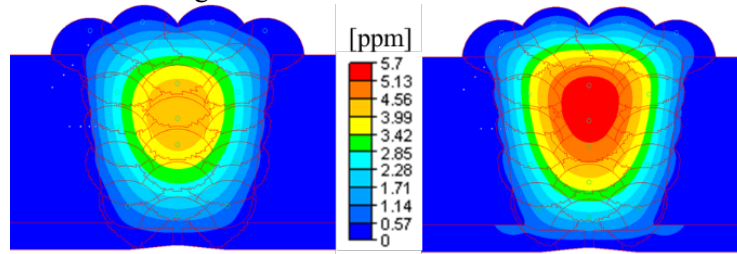


Figure 40 Lattice hydrogen. Full heat treatment (left), no heat treatment (right).

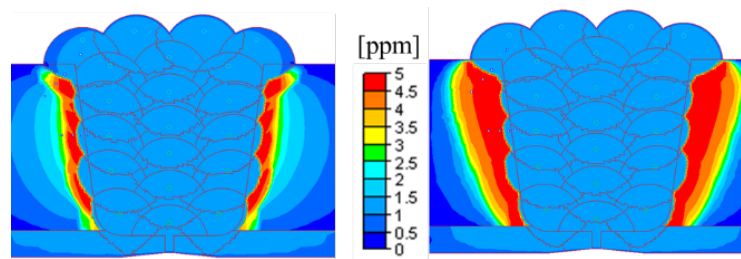


Figure 41 Trapped hydrogen. Full heat treatment (left), no heat treatment (right).

Because of strong coupling of the diffusivity to the temperature, post-weld heat treatment has large effect on decreasing the level of hydrogen in and adjacent to the weld. As shown by the above results, trapped hydrogen accumulates in the brittle HAZ where the level of residual stresses is significant. This makes the zone prone to hydrogen embrittlement. Omitting interpass heating had negligible influence on the calculated hydrogen distribution, which is because the time is too short to have effect compared to the time used for PWHT.

Without available experiments and/or a crack criterion that combines microstructure, residual stresses and hydrogen, it is difficult to judge if any of the weld cases studied will crack. Literature that addresses hydrogen in combination with residual stresses and an unfavourable microstructure to reduce the risk for cracking is limited. Clad pipes make such evaluation even more complicated as these combine different materials for the base metal and the clad, often also for the weld metal. Because stresses equal to yield stress are localized together with large level of hydrogen and a brittle microstructure, cracking is likely for the examined case despite use of heat treatment.

The appearance of the advanced hydrogen diffusion model that was applied in this study is seen from Figure 42. While the RHS part of this figure identifies a log point in weld segment #8, the LHS part shows details on how temperature, lattice hydrogen, trapped hydrogen and total hydrogen changes during welding. Each time a new segment is added the temperature increases, with the largest temperature rise caused by the three weld segments added above – segments #11, #14 and #17. Hydrogen introduced in weld segment #8 decreases rapidly until weld segment #11 is added. Fresh hydrogen in the weld increases slightly the level of hydrogen in the log point before it again continues to decrease. Trapped hydrogen is temporarily released when heat from neighbouring weld segments rises the temperature in weld segment #8. When the temperature drops, hydrogen returns to the traps. This interplay between trapped hydrogen and lattice hydrogen is clearly demonstrated in Figure 42.

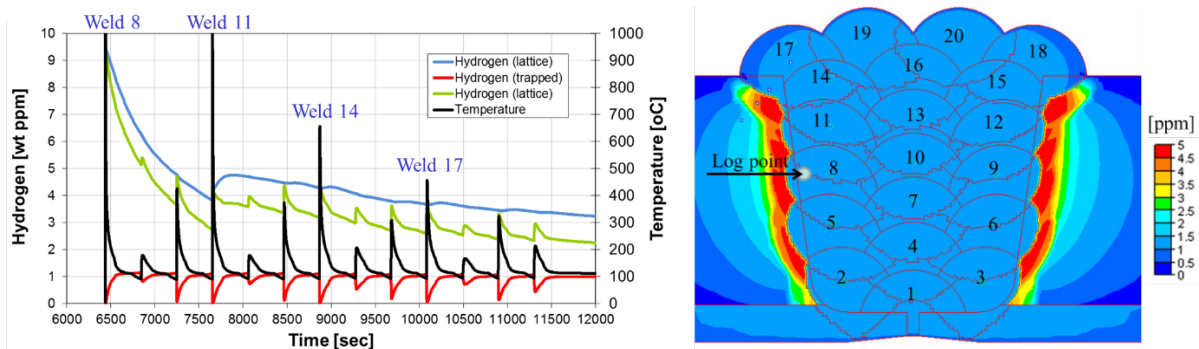


Figure 42 Time-dependent hydrogen concentrations and temperature in weld segment #8.

The hydrogen diffusion model predicted high levels of both lattice and trapped hydrogen, with the latter being far less mobile and therefore more difficult to reduce. Because of the low diffusivity of hydrogen in austenite, as well as the high solubility, the hydrogen content in the weld metal decreases very slowly. Because of its ductility, cracking in the austenite is of less concern. Because of the strong coupling of the diffusivity to the temperature, PWHT was demonstrated to have significant effect on reduction of hydrogen in the weld. For the specific case, the calculations predicted a brittle microstructure in the HAZ where trapped hydrogen is accumulated. Along the HAZ-FZ interface, residual stresses equal to the yield stress were obtained and combined with high level of hydrogen it makes the weld susceptible for cold cracking.

This study was presented at the 26th International Conference ISOPE 2016. A full paper is available in the conference proceedings, see publication no 22.

3.2.4 Task 2.4: Pre- and Post-Weld Heat Treatment

Diffusion of Carbon at the Bimetallic Base-Clad Interface

Clad pipes are manufactured both with and without a thin nickel interlayer. Diffusion of carbon from the base material to the clad, which degrades the structure adjacent to the interface and increases the local embrittlement, is effectively reduced by this interlayer. However, a majority of the existing subsea clad pipes are without this interlayer, and diffusion of carbon at the bimetallic interface is an issue that needs to be addressed. For repair welding a methodology was developed for calculation of carbon diffusion, or diffusion of any other elements, that also accounts for heat treatment applied in the production process of the clad pipes, diffusion bonding.

In a welding simulation the typical size of the elements is of the order 10^{-3} m (RHS of Figure 43 (a)). Diffusion of carbon is significantly slower than both diffusion of heat and diffusion of hydrogen (LHS of Figure 43 (a)) and therefore requires an element size of the order 10^{-6} m or less (Figure 43 (b)), which is too small for a welding simulation. Typically, the grain size adjacent to the bimetallic interface is of the order 10^{-5} m, while the width of the grain boundary is of the order 10^{-9} m.

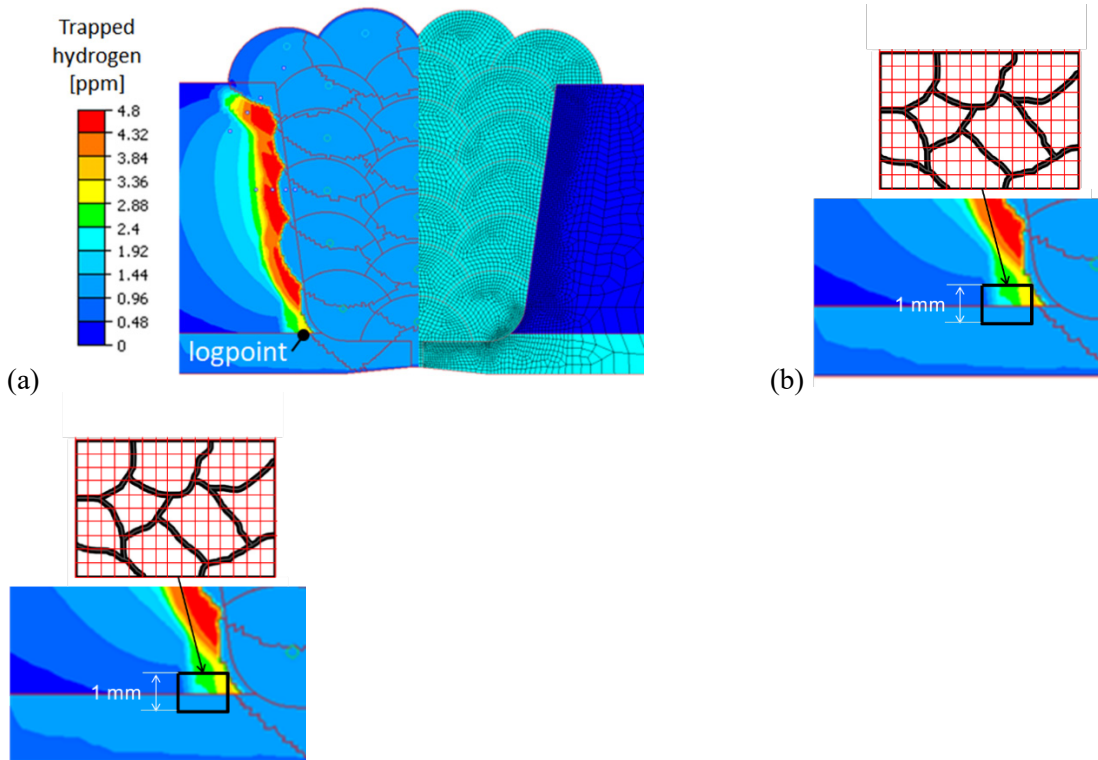
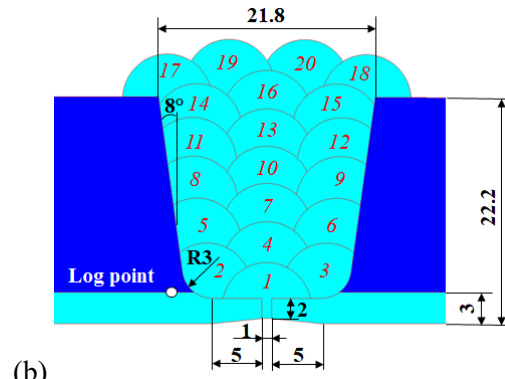
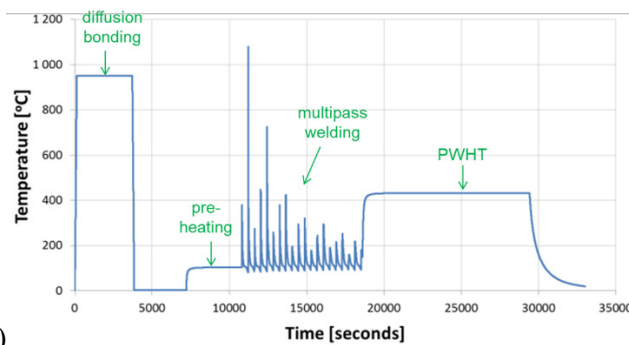


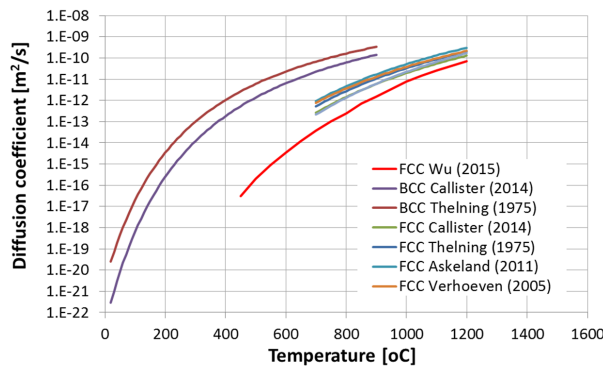
Figure 43 (a) The computational mesh, (b) Sub-domain mesh.

A solution is to divide the simulation into two parts; one welding simulation that focuses on the complete weld domain and another simpler, subsequent diffusion calculation that focuses only on pre-selected sub-domains with significantly smaller elements at the base-clad bimetallic interface. At log points like that included in Figure 43 (a), the calculated temperatures at every time step in the welding simulation are logged which ensures that all short-lived peak temperatures obtained during the welding is included in the diffusion calculation. If available, the log file can be extended after the welding simulation to also include recorded temperatures from the diffusion bonding (DB) process. In this way all significant heat cycles that influences on diffusion of carbon, or any other elements, are accounted for.

An example of temperatures stored on a log file and to be used in a carbon diffusion calculation is shown in Figure 44 (a). It accounts for diffusion bonding, pre-heating, heat input from the weld passes, interpass heating and finally PWHT. For an existing pipeline being subject to a repair weld, the time between diffusion bonding and welding can be several years. At low temperatures the diffusion coefficient of carbon is extremely low and therefore the carbon profile at the base-clad interface is insignificantly influenced. Diffusion coefficients in iron is shown in Figure 45.



(a) (b)
Figure 44 (a) Temperature history, (b) Weld geometry.



REFERENCES:

- Askeland, DR, Fulay, PP, and Wright, WJ (2011). "The Science and Engineering of Materials," 6th edition, Cengage Press.
- Callister, WD, and Rethwisch, DG (2014). "Materials Science and Engineering. An introduction," Wiley.
- Thelning, K-E (1975). "Steel and its Heat Treatment," Bofors Handbook, Sweden, Butterworth-Heinemann Limited.
- Verhoeven, JD (2005). "Metallurgy of steel for bladesmiths and others who heat treat and forge steel," Iowa State University, USA.
- Wu, D, Ge, Y, Kahn, H, Ernst, F, and Heuer AH (2015). "Diffusion profiles after nitrocarburizing austenitic stainless steel," Surface & Coatings Technology, Vol. 279, pp. 180–185.

FCC = Face-Centered Cubic crystal structure
 BCC = Body-Centered Cubic crystal structure

Figure 45 Diffusion in iron.

WeldSimS was used to solve for the energy equation (temperatures/enthalpies), the microstructure evolution and the carbon diffusion. To demonstrate the methodology a case study of repair welding of clad pipes (Figure 44 (b)), with X70 used as base material and AISI 316L as clad material, was carried out. Based on a bonding time of 1 hour and PWHT of 3 hours, several simulations were carried out where the bonding temperature (from 900°C to 1050°C) and PWHT temperature (from 263°C to 515°C) were varied. The resulting temperature history at the log point (Figure 43(a)) with $T_{DB}=950^{\circ}\text{C}$ and $T_{PWHT}=431^{\circ}\text{C}$ is shown Figure 44 (a). Similar curves were obtained for other combinations of T_{DB} and T_{PWHT} .

Significant amount of carbon diffusion occurs in the DB process. Resulting carbon profiles across the base-clad interface vs. the bonding temperature are included in Figure 46. The decarburized zone on the base metal side is larger than the corresponding carburized zone on the clad side. Resulting profiles obtained after diffusion bonding (950°C), welding and PWHT (431°C) are shown on the LHS of Figure 47. Even if some of the weld cycles induce large local temperatures at the bimetallic interface, these are too short-lived to have significant influence on the carbon profile. As seen from the RHS of Figure 47, PWHT applied at a large temperature and for a long time influences significantly on the diffusion of carbon. During PWHT the ratio of the diffusivities on each side of the interface is large ($\sim 10^5$), which moves the kink point at the bimetallic interface towards a larger carbon concentration value and in the opposite direction than in the DB process.

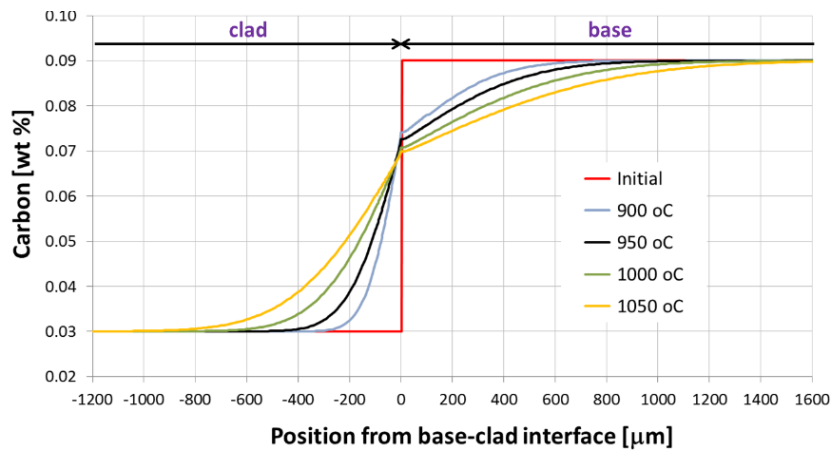


Figure 46 Carbon profiles across the base-clad interface vs. bonding temperature.

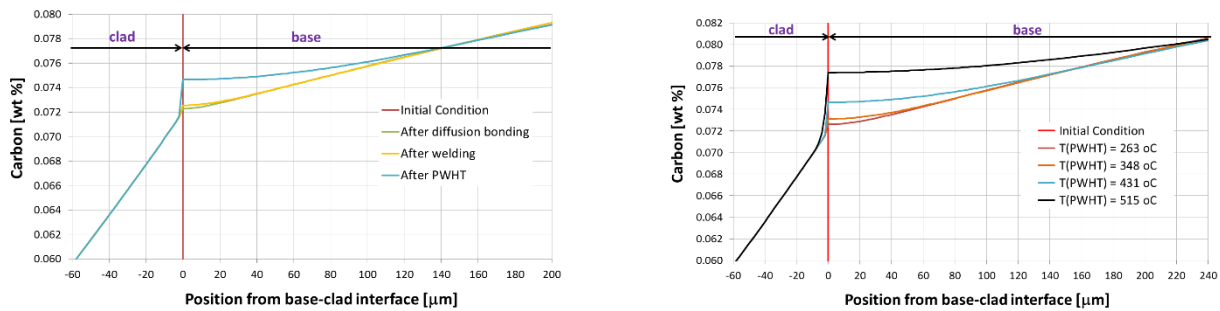


Figure 47 Left: Carbon profiles across the base-clad interface after DB, after welding and after PWHT. Right: Carbon profiles across the base-clad interface obtained after PWHT.

Besides to demonstrate the methodology, the case study shows that the thermal process to produce the clad pipes (diffusion bonding) has the largest influence on the formation of a carburized/decarburized zone adjacent to the clad-base material interface. PWHT applied at a large temperature and for a long time proved to give significant contribution to the diffusion, but still less than that of diffusion bonding. Even if some of the weld cycles induce large local temperatures at the bimetallic interface, with the diffusion coefficient of carbon raised several orders of magnitude, these are too short-lived to make any impact. For repair welding a challenge is to obtain reliable temperature data from the diffusion bonding process which may have been performed long time (years) prior to the repair welding.

This study was presented at the 28th International Conference ISOPE 2018. A full paper is available in the conference proceedings, see publication no 33.

3.3 WP3 Technical solutions (WP leader: Ragnhild Aune, SINTEF)

3.3.1 Task 3.1 Hyperbaric CMT (Cold Metal Transfer) welding

Root pass welding up to 35bar

Hyperbaric TIG Root pass weld has been used for years⁶. However, as the method is diver assisted and limited to depth (180msw) because of the wear of the tungsten electrode, trials have been performed to do root pass welding using the MIG method which is also easier to automate. However, the MIG method has not resulted in acceptable root pass penetration without using backing⁷. The CMT is a short-circuiting method adding much lower heat input into the weld pool than the conventional MIG welding method. In this work hyperbaric CMT root pass welding has been tested for different base and filler wire combinations, mainly at 5bar (40msw), as shown in Table 10. Some few tests have also been performed at 35bar (340msw) and 150 bar (1500 msw). The test specimen grooves are shown in Figure 48a where the fit-ups 2-0-0 (root face - high/low - root gap (in mm)) and 2-1.5-2 have been tested. The root face has been 2mm for all test specimens. Welding has been performed on plates simulating different positions around a pipe when welding from 12 to 6 o'clock position, as shown in Figure 48b. A summary showing root pass cross sections for different base and filler material combinations are shown in Figure 49 and Figure 50. Combination of base and filler wire materials with high viscosity, as the 316L/Alloy 59, gives acceptable root pass with root gap but is more challenging without root gap and high low, especially at 3 and 0430 o'clock positions, where the weld pool does not float out into the sidewalls and penetration is limited. Combination of base and filler wire materials with low viscosity, as the C-Mn/Coreweld, is more challenging both with and without root gap, although possible to get good results. Without root gap and high/low the weld pool floats out better into the sidewalls and penetration is good, but the parameter window for both fit-ups is narrow because of the low viscosity.

PT-400HM and PZ-400HM , both flux cored arc filler wires, were used for welding High Mn steel. The PT-400HM produced slag during welding, and it is not relevant for further testing. However, it was possible to do root pass welding with both filler wires.

Table 10 Overview of base and filler wire combinations welded at different chamber pressure.

Chamber pressure [bar]	Base material	Base material thickness [mm]	Filler wire	Filler wire diameter [mm]
5/35	C-Mn	15	Alloy 59	1
5	C-Mn	15	ESAB Coreweld HBQ	1
5/35	316L	15	Alloy 59	1
5/35	316L	15	Thermanit 309LMo	1.2
5	High Mn	15	PT-400HM	1.2
5	High Mn	15	PZ-400HM	1.0

⁶ O.M. Akselsen, R.Aune, H. Fostervoll, A.H. Hårsvær: "Dry Hyperbaric Welding of Subsea Pipelines", Welding Journal, 85, 2006, 52-55.

⁷ SINTEF Report No. F25928 DEEPIT Project.

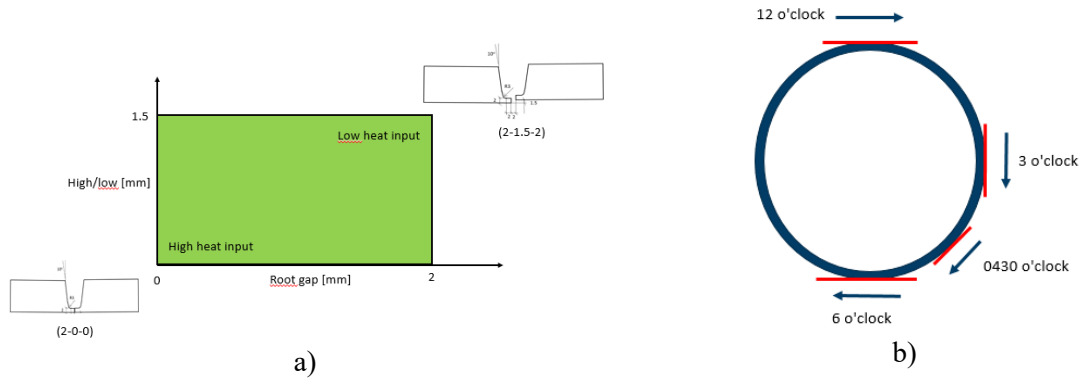


Figure 48 Groove configuration a) and welding position and direction b).

Base metal/ Filler wire/ Fit-up	Clock position			
	12	3	4:30	6
316L/ Alloy 59/ 2-1.5-2				
316L/ Alloy 59/ 2-0-0				
316L/ Thermanit 309LMo/ 2-1.5-2				
316L/ Thermanit 309LMo/ 2-0-0				

Figure 49 Root pass cross-sections for two different fit-ups using for Alloy 59 or Thermanit 309LMo as filler wires for welding 316L stainless steel in different clock positions (5bar).

Base metal/ Filler wire/ Fit-up	Clock position			
	12	3	4:30	6
C-Mn/ Alloy 59/ 2-1.5-2				
C-Mn/ Alloy 59/ 2-0-0				
C-Mn/ ESAB Coreweld/ 2-1.5-2				
C-Mn/ Esab Coreweld/ 2-0-0				

Figure 50 Root pass cross-sections for two different fit-ups using for Alloy 59 or Coreweld HBQ as filler wires for welding C-Mn steel in different clock positions (5bar).

Root pass welding has been performed at 35bar for the combinations 316L/Alloy 59 (Fit-up: 2-0-0), 316L/Thermanit 309LMo (Fit-up: 2-0-0) and C-Mn/Alloy 59 (Fit-up: 2-1.5-2). For the same working distance, the arc voltage increases as the chamber pressure increases. For the combination 316/Alloy 59 it was possible to use the same parameters (except for the arc voltage) as at 5bar to obtain acceptable welds, as shown from Figure 51. For the combination 316L/Thermanit 309LMo the welding parameters must be adjusted from 5bar welding parameters to obtain an acceptable result as shown in Figure 52. For the combination C-Mn/Alloy 59 the welding speed was decreased from 8.4 to 7.6m/min to obtain an acceptable weld, as shown in Figure 53. As shown from these results, the welding parameters must be adjusted (more or less) depending on base and filler material combination for increasing chamber pressure.

Root pass 316L/Alloy 59 (2-0-0),
35bar, 12 o'clock (same
parameters as at 5 bar)



Figure 51 Over and underside of welding showing acceptable root pass penetration for the combination 316L/Alloy 59 for fit-up 2-0-0 (35bar).

Root pass 316/309LMo (2-0-0),
35bar, 12 o'clock (same
parameters as at 5 bar)

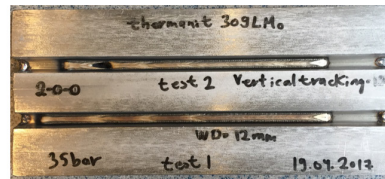


Figure 52 Over and underside of welding showing not acceptable root pass penetration for the combination 316L/Alloy 59 for fit-up 2-0-0 (35bar).



Figure 53 Root pass cross section for fit-up 2-1.5-2 using Alloy 59 as filler wires for welding C-Mn steel at 12 o'clock position (35bar).

Because of the zero-root gap challenge, controlling the gap spacing by applying so called protrusions as shown in Figure 54 to ensure a root gap have been examined. Test specimens with 0.5, 1 and 2mm root gaps have been tested at the 12 o'clock position. For a combination of materials with high viscosity (as the 316L/Alloy 59) good results were obtained. For materials with low viscosity as C-Mn/Coreweld HBQ it is however more challenging.

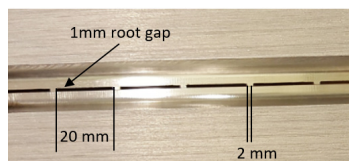


Figure 54 Groove with protrusion (2mm with no root gap) and 20 mm of root gap of 1 mm.

Root pass welding at 5bar - Robustness

Robustness testing of the developed parameters for fit-ups 2-0-0 and 2-1.5 in the 12, 3, 0430 and 6 o'clock positions is performed for different base and filler metal combinations. The root gap for these test specimens were increasing from 0 to 2-3 mm. The high/low was 0 mm, except for some few tests where the high/low was 1.5mm. Figure 55 summarizes the results for the root pass welding with different material combinations. As seen from Figure 55, the most robust welding positions are 3 and 0430 and the least robust welding position is

6 and 12 o'clock positions. For test specimens with protrusions, the results were the same. Further details of the project results are summarized and published in the SINTEF technical report⁸.

316L/ Alloy 59	Clock position			
	12	3	0430	6
Acceptable root welds for root gaps [mm] between:				
2-0-0 parameters	0-1.4	0-1.6	0-2++	0-1.6
2-1.5-2 parameters	1-2.2 0.8-2.4*	0.75-2.4++ 1.9-2.8*++	1.8-2.4++	1.25-1.8
316L/ Thermait 309LMo	Clock position			
	12	3	0430	6
2-0-0 parameters	0-0.9	0-2.9++	0-1.5	0-1.5
2-1.5-2 parameters	1-2.7	1-2.8++	1-2.7++	1.5-2.4
C-Mn/ Alloy 59	Clock position			
	12	3	0430	6
2-0-0 parameters	0-1.4	0-2++	0-2++	0-1.4
2-1.5-2 parameters	0.7-2.0	1.5-2.8++	1.6-2.9++	0.75-2.3
C-Mn/ ESAB Coreweld	Clock position			
	12	3	0430	6
2-0-0 parameters	0 - 0.8	0 - 2.5++	0 - 2	0 - 0.7
2-1.5-2 parameters	1.75 - 2.5++	1.9 - 2.4++	1.75 - 2.5++	1.5 - 1.75

Figure 55 Robustness testing using welding parameters developed for fit-up 2-1.5-2 and 2-0-0 at 5bar for varying root gap. The numbers in the table show the root gap in mm where acceptable root pass penetration was obtained. ++ means that the root pass penetration was still satisfactory at this root gap and may give acceptable penetration for larger root gaps (*High/low=1.5mm, else 0mm).

3.3.2 Task 3.2: Subsea repair of clad and lined pipes & Task 3.3: Effect of shielding gas on phase constituents in the root pass

These tasks were intended as PhD work. As the PhD candidate left his position, the work was continued as a post doc work and finalized in February 2020, see paragraph 4.2.

3.3.3 Task 3.4: Hydrogen effects

Hydrogen diffusion during welding has been implemented in WELDSIMS, see paragraph 3.2.3. The distribution of hydrogen in the weld metal and HAZ after welding, is a clue to the understanding of the 'hot spots' for hydrogen fracture initiation. The hydrogen distribution is also an input to the predictive model for hydrogen induced fracture.

3.3.4 Task 3.5: Characterization of microstructures and secondary phases

This task was performed by Helena Bjaaland as part of her project and master thesis works at NTNU. Base metal, heat affected zone, weld metal and the clad interface of welded clad pipes were characterized by optical

⁸ R. Aune, "Remotely Controlled Hyperbaric butt-welding for pipeline repair, Part I: Hyperbaric CMT root pass welding up to 150bar", SINTEF Report 2020:00235

microscopy, scanning electron microscopy, transmission electron microscopy, electron microprobe analyses and micro hardness measurements.

The following welded samples were investigated:

- Sample 1 (WPT-DJ): 316L clad, X60 BM, 309L root + hot pass, IN625 fill + cap.
- Sample 2 (WP-24): 316L clad, X60 BM, IN625 root + hot pass, IN625 fill + cap.
- Sample 3(1W kl.9): 316L clad, X65 BM, IN625 root + hot pass, IN625 fill + cap. With Ni-interlayer between clad and BM.

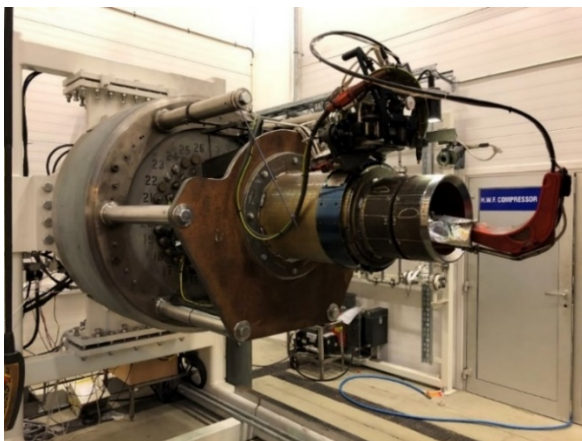
The work is published as a project thesis, a master thesis and a conference paper, see paragraph 7, publication no 7, 13 and 14.

3.3.5 Task 3.6: Pre- and post-weld heating

The influence of post weld heat treatment on carbon diffusion, and hence the tendency of carbide precipitations, have been investigated applying WELDSIMS, see paragraph 3.2.4.

3.4 WP4 Demonstrators (Ragnhild Aune)

From welding in fixed welding positions on plates at SINTEF at a maximum pressure of 35bar, the welding equipment was transported to Killingøy to be able to do orbital welding at pressure up to 150bar, as shown in Figure 56. Welding, both root and filler passes, was performed from 12 to 6 o'clock position, i.e., downhill welding.



a)



b)

Figure 56 a) Welding equipment P 450 from CRC Evans and Fronius and a welding coupon, and b) 400bar pressure chamber.

Root pass welding

Based on CMT root pass welding with different material combinations and positions on plates, the most promising combinations were tested further by orbital welding as shown in Table 11. Welding on X70 pipes with Alloy 59 filler was challenging due to high viscosity resulting in bad flow against the sidewalls and building of concave weld beds, while welding with Coreweld HBQ filler gave very good results. Successful orbital (downhill only) root pass welding was performed for fit-ups 2-1.5-2 and 2-0-0 at 5 and 150bar. Macros showing the root penetration for the most successful welds sampled close to 12, 3/9 and 6 o'clock positions are shown in Figure 57 and Figure 58.

For clad pipes, successful orbital (downhill only) root pass welding was performed with Alloy 59 as filler wire for fit-ups 2-1.5-2 and 2-0-0 at 5 and 150bar. Macros showing the root penetration for the most successful welds sampled close to 12, 3/9 and close to 6 o'clock are shown in Figure 59 and Figure 60.

Table 11: Overview of base and filler wire combinations welded at different chamber pressure for orbital root pass welding.

Chamber pressure [bar]	Base material	Base material thickness [mm]	Filler wire	Filler wire diameter [mm]
5 and 150	X70	27.2	ESAB Coreweld HBQ	1
5	X70	27.2	Alloy 59	1
5 and 150	Clad (316L/X60)	19	Alloy 59	1

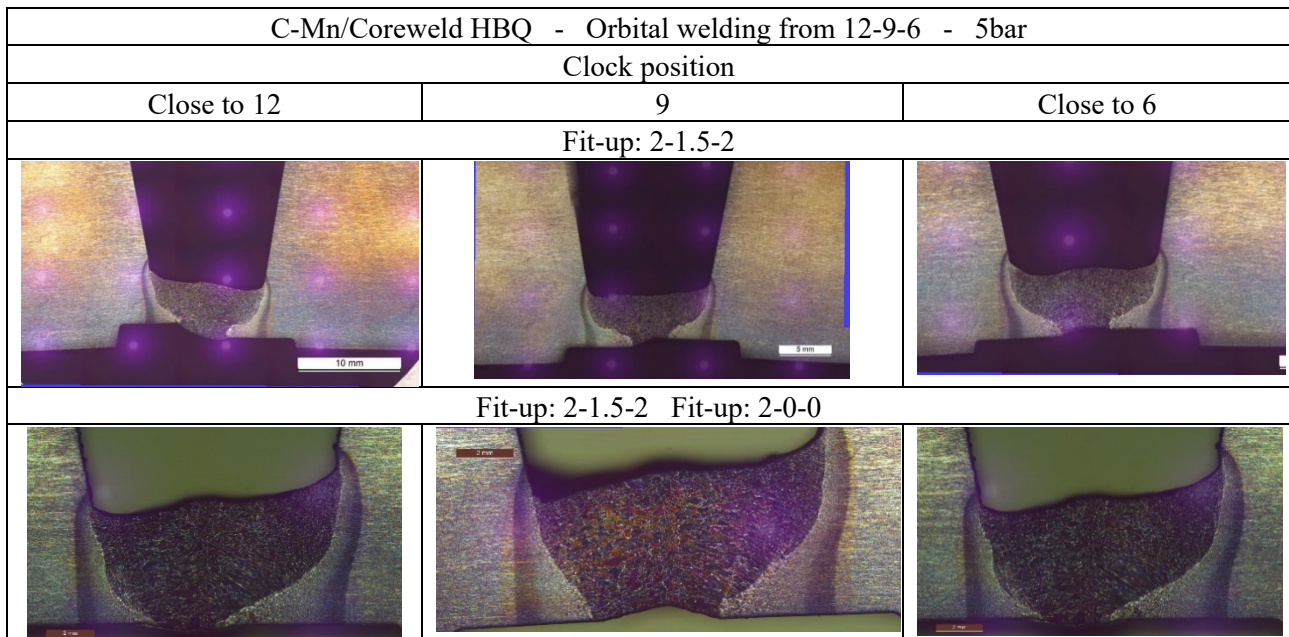


Figure 57: Successful orbital root pass welding from 12-9-6 positions for a fit-up of 2-1.5-2 and 2-0-0 for C-Mn (X70) welded with Coreweld HBQ at 5bar.

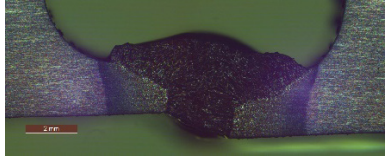
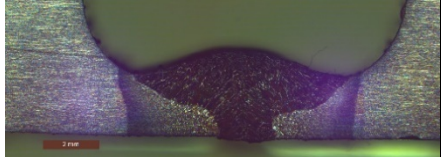
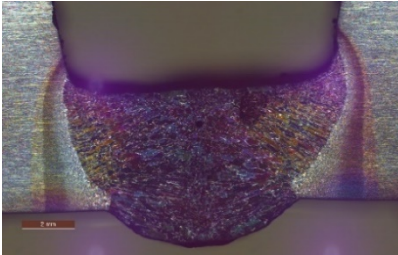
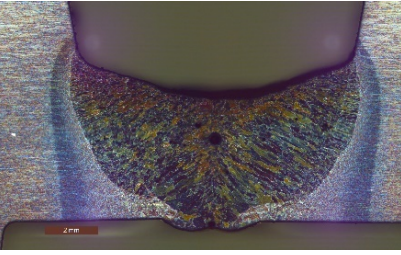
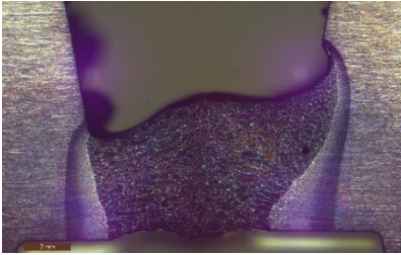
C-Mn/Coreweld HBQ - Orbital welding from 12-9-6 - 150bar		
Clock position		
	3	Close to 6
Fit-up: 2-1.5-2		
		
Fit-up: 2-0-0		
		
a)	b)	c)

Figure 58: Successful orbital root pass for a fit-up of 2-1.5-2 showing penetration at a) 3 and b) 6 o'clock positions for C-Mn (X70) welded with Coreweld HBQ at 150bar.

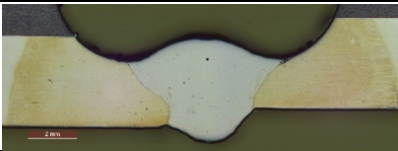
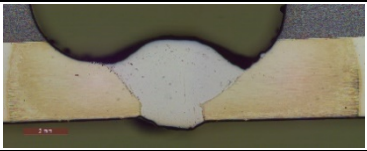
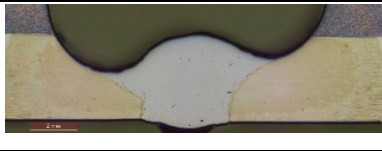


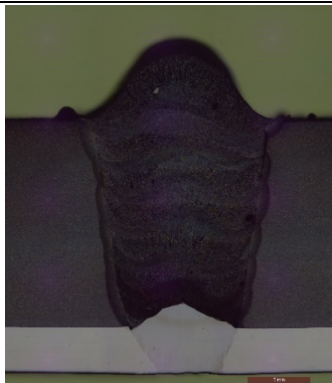
Clad pipe/Alloy 59 - Orbital welding from 12-3-6 - 5 bar		
Clock position		
Close to 12	3 o'clock	Close to 6 o'clock
Fit-up: 2-varying-varying		
		
Fit-up: 2-varying-about 0		
		

Figure 59: Successful orbital root pass welding from 12-3-6 positions for a fit-up of (2-Varying-Varying) and (2-varying-close to 0) for clad pipe welded with Alloy 59 at 5bar.

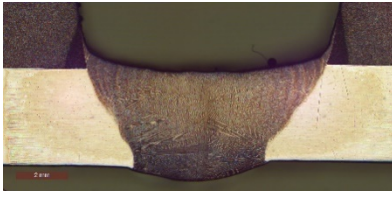
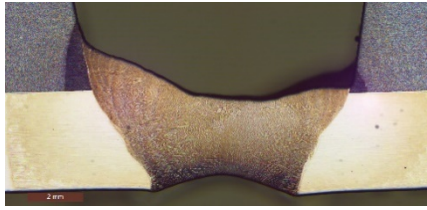

Clad pipe/Alloy 59 - Orbital welding from 12-9-6 - 150bar		
Clock position		
Close to 12	08.30	Close to 6
Fit-up: 2-varying-about 0		
		

Figure 60: Successful orbital root pass welding from 12-9-6 positions for a fit-up of (2-Varying-about 0) showing penetration a) close to 12 o'clock, b) 0830 o'clock and c) close to 6 o'clock for clad pipe welded with Alloy 59 at 150bar.

Multipass welding at 150bar

An overview of the base and filler wire combinations welded at different chamber pressure for multipass welding is shown in Table 12. For the combination C-Mn steel and Coreweld HBQ filler wire, a successful orbital weld was made at 150bar (X65) as shown in Figure 61. The root pass was welded with the CMT method, while the filler passes were welded with the pulsed MIG method. All mechanical test results as hardness, Charpy-V and all weld tensile results were acceptable according to standard⁹. Hardness test results were also acceptable to sour service conditions. All weld yield tensile strength test result was below the yield strength for the base material, however, above the Specified Minimum Yield Stress (SMYS) of X65.

For the combination Clad pipe (316L/X60) and Alloy 59 filler wire, a successful orbital weld was made at 150bar as shown in Figure 62. The root pass was welded with the CMT method, while the filler passes were welded with the pulsed MIG method. All mechanical test results as hardness, Charpy-V and all weld tensile were acceptable to standard. Further details of the project results are summarized and published in SINTEF technical report¹⁰.

Based on following results, it is possible to do successful hyperbaric root and filler passes butt welds up to 150bar using the CMT and pulsed MIG methods.

Table 12: Overview of base and filler wire combinations welded at different chamber pressure for orbital root and filler pass welding.

Base material/ Wall thickness [mm]	Filler wire	Fit-up	Chamber pressure [bar]	Welding position	Number of passes
X65/14.3	Coreweld HBQ	2-0-0	150	5G downhill, PJ	5

⁹ Offshore standard DNV-OS-F101, "Submarine Pipelines Systems", October 2013.

¹⁰ R. Aune, "Remotely Controlled Hyperbaric Butt-welding for Subsea Pipeline Repair, Part II: Welding complete welds up to 150bar", SINTEF Report 2020:00236

Clad pipe/19	Alloy 59	(1.84-3.5)- (0.27-1.15)- (0.05-0.1)	150	5G downhill, PJ	7
--------------	----------	---	-----	-----------------	---

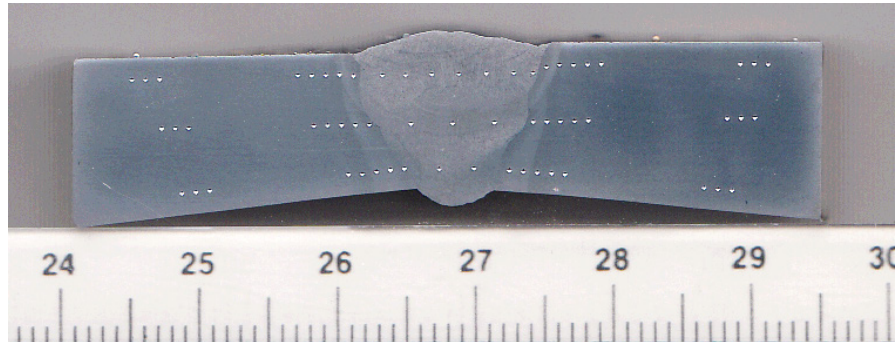


Figure 61: C-Mn (X65) welded with Coreweld HBQ as filler wire at 150bar and macro close to 12o'clock position.



Figure 62: Clad pipe welded with Alloy 59 as filler wire at 150bar and macro close to 12o'clock position.

4 PhD and Post Doc.

4.1 PhD Lise Jemblie

Dr. Lise Jemblie defended her thesis "Hydrogen embrittlement of clad steel pipes" in June 2018.

The two main subjects she covered were:

- 1) The fracture properties and hydrogen embrittlement susceptibility of clad steel pipes, with and without an intermediate Ni-interlayer between the clad and the base material.
2. Coupled diffusion and cohesive zone finite element modelling for numerically assessing the hydrogen embrittlement susceptibility of steel structures.

The prediction of hydrogen induced fracture in not welded fracture toughness specimens, as described in paragraph 3.1.3, by developing and applying 2D and 3D numerical models for prediction of hydrogen induced fracture was a central task. A 3D model of a deformed fracture toughness specimen is presented in Figure 56. The work was conducted under WP1 Structural integrity, with supervision from Prof. Odd M. Akselsen and SINTEF scientists.

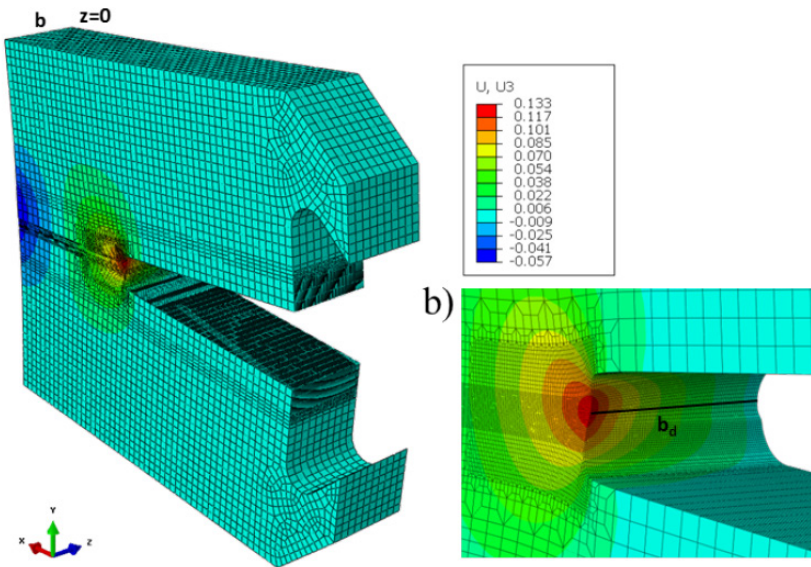


Figure 63 Deformed shape of the CT FE model at fracture initiation in air, (a) FE model. (b) Notch tip close-up.

The models were fitted to fracture mechanics tests in air before hydrogen was applied in varying lattice concentrations. Best representation of the experimental test results in hydrogen (CP) was obtained for a lattice hydrogen concentration of 0,005 wppm, see Figure 57.

Table 2 – Experimentally determined fracture initiation toughness values for the bi-material X60/316L specimens, tested in air and under CP.

Env.	δ_i [mm]	J^a [N/mm]	K_{Ic}^b [MPa \sqrt{m}]
Air	0.176	173	199
CP	0.025	25	76

^a $J = 2\delta R_{p0.2}$
^b $K_{Ic} = (J/E(1-\nu^2))^{1/2}$

a)

Table 4 – Simulated CTOD fracture initiation toughness for $C = C_{Lo}$, with C_{Lo} in the range 0.000513–0.5 wppm and trap density models by Kumnick and Johnson and Sofronis et al.

C_{Lo} [wppm]	CTOD (δ_i) [mm]	
	Trap model	
	Kumnick & Johnson	Sofronis et al.
0	0.173	0.173
0.000513	0.111	0.112
0.005	0.023	0.024
0.05	0.002	0.002
0.5	0.0002	0.0002

b)

Figure 64 Comparison of a) experimental and b) numerical results for fracture toughness tests in air and hydrogen.

The main conclusions from the numerical work were as follows:

- The reported numerical simulations revealed a significant dependency on the choice of mass diffusion input parameters, trap density formulation and hydrogen boundary conditions on the resulting hydrogen distributions and fracture initiation toughness values.

- Both hydrogen in lattice and hydrogen trapped at dislocations were found to be possible sources of the hydrogen embrittlement of clad steel pipes, dependent on the overall choice of input parameters and hydrogen boundary conditions.
- The numerical model can qualitatively predict the detrimental effect of hydrogen on the fracture initiation toughness of clad pipes, giving reasonable results when compared to experimental findings. Further effort is necessary to provide a reliable description of the interface hydrogen content and distribution.
- Asymmetrical notch opening, and plastic zone size was revealed for all simulations, confined to the undermatching base material. The deleterious effect of material mismatch was found to be less severe in hydrogen environment.

Lises work is published in the thesis document as well as in four publications in international Journals with peer review and four conference contributions:

Main papers:

- 1) L. Jemblie, H. Bjaaland, B. Nyhus, V. Olden, O.M. Akselsen, Fracture toughness and hydrogen embrittlement susceptibility on the interface of clad steel pipes with and without a Ni-interlayer, *Materials Science and Engineering: A*, Volume 685, 8 February 2017, Pages 87-94, 2017.
- 2) L. Jemblie, V. Olden and O. M. Akselsen, A coupled diffusion and cohesive zone modelling approach for numerically assessing hydrogen embrittlement of steel structures. *International Journal of Hydrogen Energy*, 42(16), 11980-11995, 2017.
- 3) L. Jemblie, V. Olden, P. Mainçon, O.M. Akselsen, Cohesive zone modelling of hydrogen induced cracking on the interface of clad steel pipes, *Int Journal of Hydrogen Energy*, Vol 42, Issue 47, Nov. 2017, p 28622-28634.
- 4) L. Jemblie, V. Olden, A. Alvaro, V. Osen, B. Nyhus and O. M. Akselsen, 3D cohesive zone modelling of hydrogen embrittlement on the interface of bi-material clad steel pipes, 2017.

Additional paper:

- 5) L. Jemblie, V. Olden and O. M. Akselsen, A review of cohesive zone modelling as an approach for numerically assessing hydrogen embrittlement of steel structures. *Philosophical Transactions of the Royal Society A*, 375, 20160411, 2016.

Conference contributions:

- 6) L. Jemblie, V. Olden, A. Alvaro, H. Bjaaland, B. Nyhus and O. M. Akselsen, Hydrogen embrittlement at the interface of clad steel pipe produced by hot-roll bonding. *European Congress and Exhibition on Advanced Materials and Processes*. Warsaw, Poland, September 2015. (Poster presentation)
- 7) L. Jemblie, V. Olden, A. Alvaro, B. Nyhus and O. M. Akselsen, Hydrogen embrittlement at the interface of clad steel pipes - fracture mechanical testing and FE simulations. *2016 International Hydrogen Conference*. Jackson Lake Lodge, Wyoming, USA, September 2016. (Poster presentation)
- 8) L. Jemblie, V. Olden, B. Nyhus, O.M. Akselsen, Hydrogen embrittlement susceptibility of clad steel pipes, *ASME Pressure Vessels and Piping Conference*, Waikoloa, Hawaii, USA, July 2017. (Oral presentation and paper).
- 9) L. Jemblie, V. Olden, B. Nyhus, A. Utvær, O. M. Akselsen, Hydrogen embrittlement susceptibility on the interface of clad steel pipes, before and after welding. *International Conference on Metals & Hydrogen*. Ghent, Belgium, May 2018.

(Oral presentation and paper)

4.2 Post doc Ivan Bunaziv

Ivan started his Post doc position March 1. 2018 and finished February 29th, 2020.

In the performed work, dry hyperbaric welding of HSLA steel (X70) was tested in bead-on-plate configuration by utilizing CMT arc mode under different ambient pressures and with the use of two different filler wires. 1.0 mm in diameter ESAB Coreweld HBQ which was denoted as wire-1 and 1.2 mm in diameter Kobelco TrustArc MX-A55T was denoted as wire-2. The effect of ambient pressure on weld bead geometry and cooling rates was established. Explanation of increasing penetration depth with increase of ambient pressure was described through dimensionless numbers and results are consistent with those of other researchers. The microstructure formation was studied based on simulated thermal cycles and characteristics of non-metallic inclusions (NMIs). The effect of ambient pressure on melt flow characteristics was investigated analytically. It will be shown that the experimental results are in good agreement with numerically simulated results.

Welding at increased ambient pressure revealed more unstable arc behaviour with destabilized CMT phases as shown on Figure 65 based on volt-ampere characteristics acquired during processing. Increased ambient pressure causes adjustment of the current/voltage where voltage is increasing by 20% in order to keep the stability of the arc.

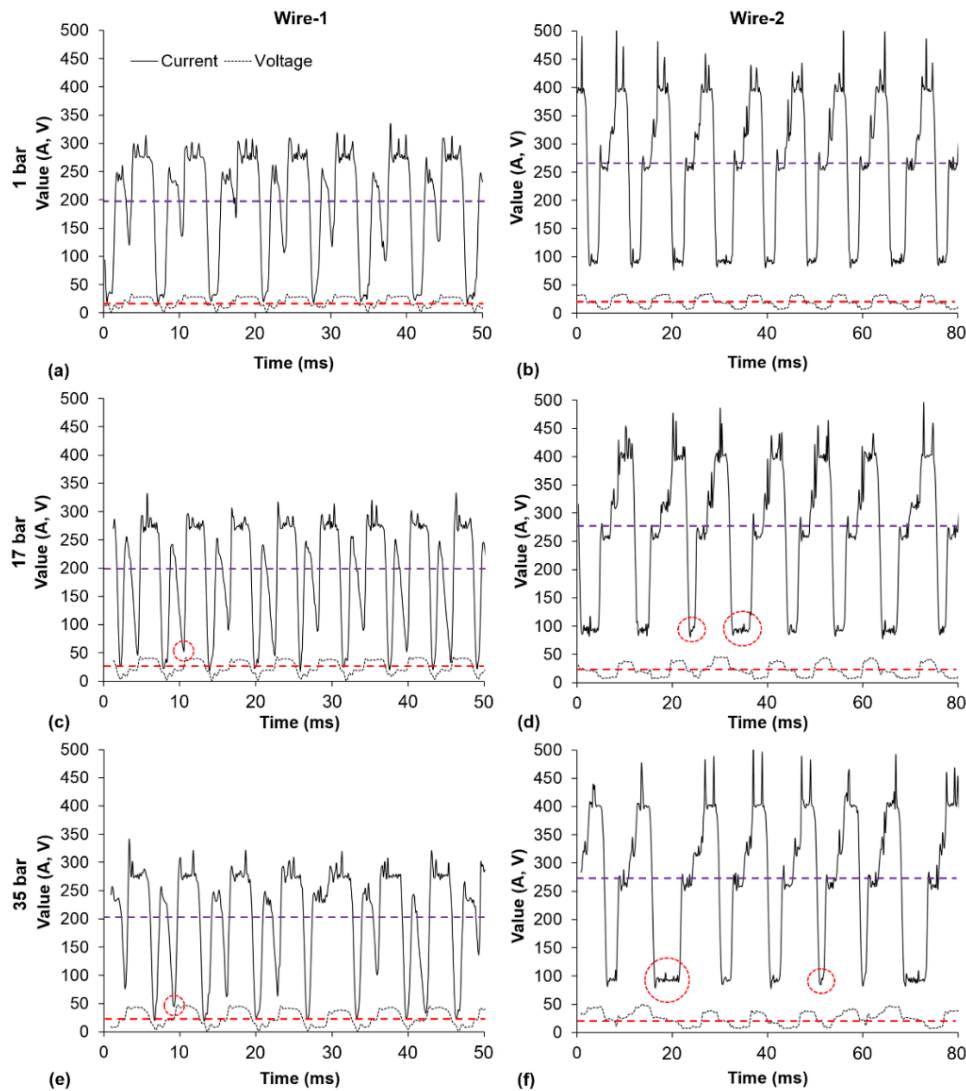


Figure 65 Volt-ampere characteristics at different ambient pressures. Mean values represented by dashed lines

The macrographs of welds are presented in Figure 66. With an increase of ambient pressure, the penetration depth is increasing. It was established by studying dimensionless number that buoyancy and Marangoni forces have low effect. The electromagnetic force was predominant even though the current was increased up to 3%. It causes additional melt vortex at the root with increasing convection due to faster melt flows. Another explanation of the increasing penetration depth is reduction of the anodic and cathodic spots as well as pressure effect due to squeezing arc. In general, a very good correlation of the increase of heat input and penetration depth was established.

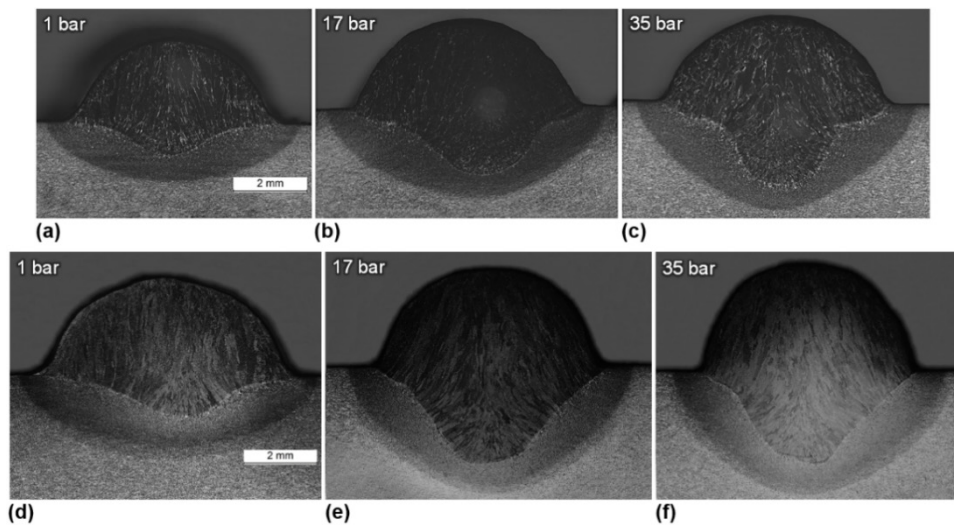


Figure 66 Effect of ambient pressure on weld width and depth in case of wire-1: (a) 1 bar; (b) 17 bar; and (c) 35 bar; in case of wire-2: (d) 1 bar; (e) 17 bar; and (f) 35 bar

Microstructure evolution of the two used filler wire is shown in Figure 67. There is a clear difference that ESAB Coreweld HBQ wire provided much higher volume fraction of the acicular ferrite and significant hardness reduction potentially providing higher toughness. By using DFLUX subroutine in ABAQUS, the cooling rate in weld metal was identified, shown in Figure 68. CMT mode produce very fast cooling rates (Δt_{8-5} is about 0.8 s) which can cause lath martensite formation, especially in case of Kobelco TrustArc MX-A55T wire.

Characterization of the non-metallic inclusions (NMIs) is shown in Figure 69. Both wires provided small average diameter (0.14-0.18 μm). Therefore, the oxygen level was measured from welds since the oxygen is very potent chemical element for acicular ferrite nucleation. According to an inert gas fusion analysis (IGFA) provided by SINTEF Molab, WM with wire-1 had 520 ppm of oxygen (regardless ambient pressure) compared to WM with wire-2 which provided 760 ppm. Therefore, other elements for NMIs composition were taken into consideration. More NMIs with composition of $(\text{Ti})_x\text{O}$ and TiN were produced in wire-2, also being potent for AF nucleation. In general, both wires produced complex NMIs with Al_2O_3 as a core with MnS and TiN as outer shell. However, both simple (e.g., SiO_2) and complex silicates (e.g., $\text{Mn}_2 \cdot (\text{Al}_2\text{O}_3)_2 \cdot \text{Si}_5$ and or $(\text{Al}_2\text{O}_3)_3 \cdot \text{Si}_2$) according to EDS mapping developed in case of wire-1 which are potent nuclei for AF. This partly explains why wire-1 provided much higher AF volume fraction. Wire-2 had higher nickel content and higher hardness, which demonstrates higher hardenability. The lower amount of AF may thus be due to excessive hardenability for the rapid cooling rate employed. The microstructure examination showed that this wire had low potency for grain boundary ferrite formation along prior austenite grain boundaries. It strengthens the assumption of excessive hardenability. This observation may be the main reason for the lower AF volume fraction, providing favourable intergranular condition for bainite to form.

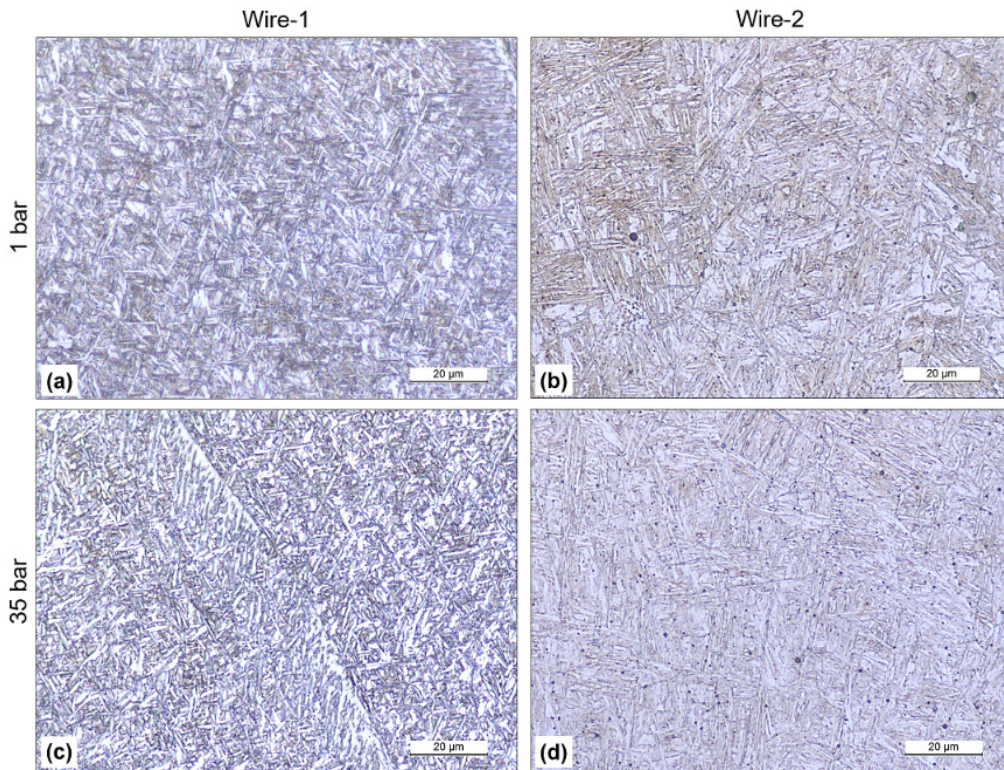


Figure 67 Optical micrographs of weld metal at different ambient pressure and filler wires. (a, c) ESAB Coreweld HBQ and (b, d) Kobelco TrustArc MX-A55T

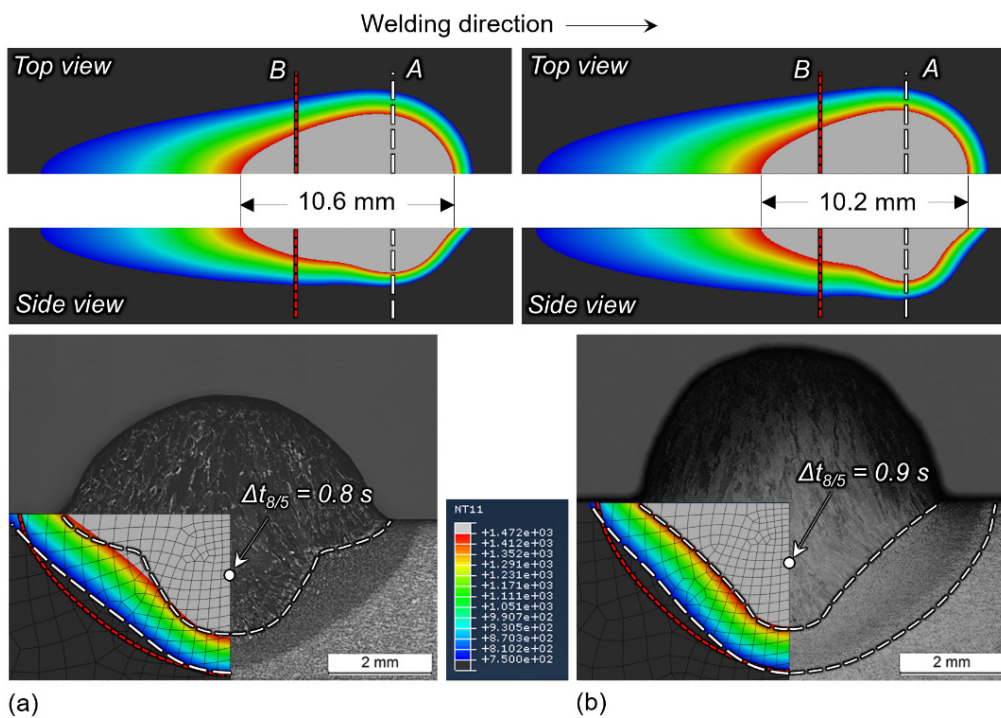


Figure 68 Numerically simulated welded joints at 35 bar ambient pressure for (a) wire-1 and (b) wire-2

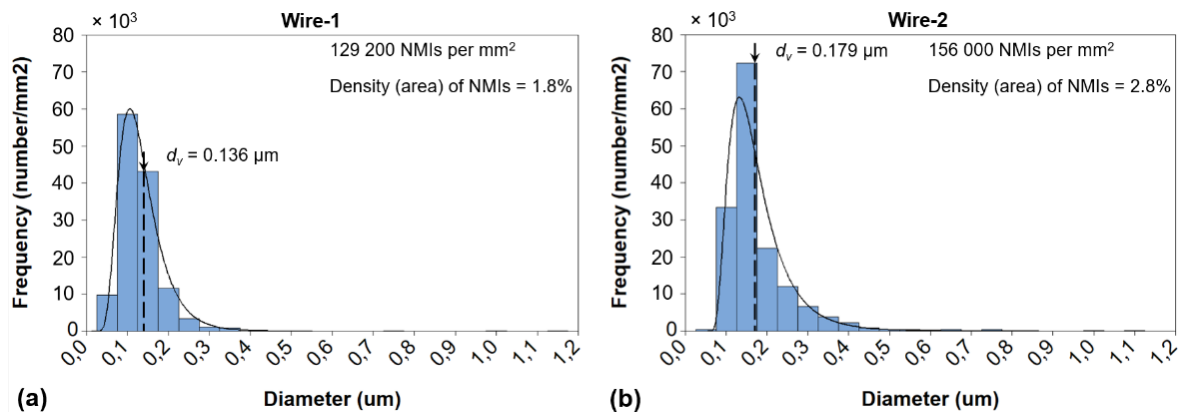


Figure 69 Statistical characterization of NMIs for (a) wire-1 and (b) wire-2

The conclusions of the performed work are:

- 1) With increase of ambient pressure, the process stability deteriorates due to constricted arc conditions
- 2) The penetration depth increases significantly with increasing ambient pressure which enhances melt flow magnitude (faster) and direction (inward)
- 3) The increased ambient pressure has low effect on the Marangoni force for enhancing penetration depth. The electromagnetic force with convective heat transport (faster melt flows) due to higher arc pressure is the most influencing factor for controlling weld geometry
- 4) Filler wire with higher silica content and lower nickel content provides higher volume fraction of acicular ferrite at any ambient pressure even though amount and mean average size of non-metallic inclusions are lower. Therefore, it is more suitable also for processes with faster cooling rates such as CMT

Publications 2019:

- Bunaziv, I., Aune, R., Olden, V., Akselsen, O.M. *Dry hyperbaric welding of HSLA steel up to 35 bar ambient pressure with CMT arc mode*. The International Journal of Advanced Manufacturing Technology 105(5-6), 2019; p. 2659-2676, doi: 10.1007/s00170-019-04511-6
- Bunaziv, I., Akselsen, O.M., Olden, V. *Metallurgical aspects in welding of clad pipelines – A global outlook*. Applied Sciences, 9(15), 2019; 3118, doi: 10.3390/app9153118

Two more journal publications from the project are planned in 2020.

5 Education and recruitment

The following students have been involved in the project through Master theses, summer jobs and internships.

- 1) Helena Bjaaland, project work, summer job and MSc, 2014-2015 (WP1)
- 2) Anh Quynn, Summer job 2015 (WP2)
- 3) Sunny Islam, NTNU project work and summer job, 2015 (WP 1)
- 4) Martin Degos, visiting internship candidate, 2016 (WP1)
- 5) Andreas Utvær, MSc and summer job, 2017 (WP1)
- 6) BSc, Malin Alette Lervåg, summer job, 2017 (WP1), hired by SINTEF

6 Project management

The project management has (so far) been responsible for submitting 10 progress reports and 4 project account reports to the RCN. 14 quarterly status reports and 1 final report (this report) have been submitted to the project group. A total of 10 project meetings (including the kickoff meeting) have been organized, two per year. The meetings have been carried out in the spring and in the fall, and all partners have hosted meetings at least one time.

7 Publications

A total number of 45 publications are produced in the period March 2014 – March 2020. This includes 7 scientific publications in international journals with peer review, 1 PhD thesis, 2 Master thesis, 14 conference papers/presentations, 4 conference posters, 3 popular science articles and 14 technical reports, including this report. A blog is also established for the project <https://www.sintef.no/en/industry/rop-blog/>, including 14 blog posts. The ROP project has taken part in arranging one international workshop and one internal workshop in cooperation with Equinor. The publication list is given below.

2014

1. O.M. Akselsen, Into the deep, popular science article in Pan European Networks, Vol 11 2014, page 95-97.
2. A. Azar, Characterization of clad pipelines, SINTEF Report 26506, 2014.
3. H. Bjaaland, Literature report on welding and PWHT of dissimilar joints, SINTEF report 26504, 2014.
4. Alvaro, P. Mainçon, V. Osen, FEM formulation for mass diffusion through UMATHT subroutine, SINTEF Report 26585, 2014.
5. M. Rudshaug, Cathode sheath model for gas metal arc welding, IFE Report IFE/KR/F-2014/134, 2014.
6. A. Azar, Influence of Welding Thermal Cycle on the mechanical Conditions around Clad/pipe interface, SINTEF Report 26506, 2014.
7. H. Bjaaland, Investigation of macros of welded joints in clad pipelines, NTNU project work and SINTEF Report 26503, 2014.
8. A. Azar, Characterization of oil & gas clad pipelines, SINTEF Report 26507, 2014.
9. D. Lindholm, H. Fjær, N. Woodward, A numerical study of hydrogen diffusion in a part size sleeve-on-mock-up exposed to two different levels of post weld heat treatment, Int. Journal of Offshore and Polar Engineering, No 24, Issue 2, 2014, page 149-156.

2015

10. D. Lindholm, A literature survey on diffusion of major alloying elements in steel, IFE, Matpro-note 001/2015.
11. V. Olden, A. Barnoush; Lite atom – stor skade, popular science article in Dagens Næringsliv, June 19., page 35.
12. X. Ren, H. Fjær, D. Lindholm, M. Rudshaug, Through-process modelling of welding: concept and perspective, In proceedings of EuroJoin 9, 20-21 May, 2015.
13. Bjaaland, H., Akselsen, O. M., Olden, V., Nyhus, B., Karlsen, M., and Hjelen, J., 2015. Metallurgical reactions in welding of clad X60 / X65 pipelines, oral presentation and in proc. Twenty-fifth Int. Ocean Polar Eng. Conf., pp. 61–66.
14. H. Bjaaland, Evaluation of Welded Clad Pipe - Microstructures and Properties, NTNU Master Thesis, June 2015.
15. A. Alvaro, V. Olden, B. Nyhus, Influence of stress concentration on hydrogen embrittlement susceptibility of a X70 weld simulated coarse grained HAZ, oral presentation at the Euromat Conference, Warsaw, September 20-24, 2015.

16. D. Lindholm, A case study on the influence of Heat Treatment on Hydrogen Diffusion and residual Stresses in Repair Welding of Clad Pipes, poster at the Euromat Conference, Warsaw, September 20-24, 2015.
17. L. Jemblie, Hydrogen embrittlement at the interface of clad steel pipe produced by hot-roll bonding, poster at the Euromat Conference, Warsaw, September 20-24, 2015.
18. V. Olden et al., A multiscale approach to interface degradation by hydrogen, invited oral presentation at the Hydrogen Energy Development Forum 2015, Kyushu University, Fukuoka, Japan, January 31, 2015.

2016

19. L. Jemblie, V. Olden and O. M. Akselsen, A review of cohesive zone modelling as an approach for numerically assessing hydrogen embrittlement of steel structures. Philosophical Transactions of the Royal Society A, 375, 20160411, 2016.
20. L. Jemblie, V. Olden, A. Alvaro, B. Nyhus and O. M. Akselsen, Hydrogen embrittlement at the interface of clad steel pipes - fracture mechanical testing and FE simulations. Poster at the 2016 International Hydrogen Conference, Jackson Lake Lodge, Wyoming, USA, September 11-14, 2016.
21. L. Jemblie et al, Hydrogen assisted fracture at the interface between clad and X60 pipeline steel, SINTEF and NTNU's Environmental Assisted Cracking workshop – SNEAC, Trondheim, 7-9 June, 2016.
22. D. Lindholm, A Numerical Case Study on Repair Welding of Clad Pipes with Focus on Post Weld Heat Treatment and its influence on Hydrogen Diffusion, Paper no 2016-TPC-0254, in Proc. Twenty-sixth Int. Ocean Polar Eng. Conf., June 26-July 2, Rhodes, Greece, 2016.
23. M. Degos, Influence of hydrogen embrittlement on welded clad X60/65 pipelines, Student Internship report Ecole des Mines, St Etienne, France.

2017

24. A. Alvaro, V. Olden, H₂ in the energy sector, popular science article in PAN European networks, science and technology, Issue 22, p 36-38.
25. P. Mainçon, Cohesive zone element, SINTEF Report 28059.
26. L. Jemblie, H. Bjaaland, B. Nyhus, V. Olden, O.M. Akselsen, Fracture toughness and hydrogen embrittlement susceptibility on the interface of clad steel pipes with and without a Ni-interlayer, Materials Science and Engineering: A, Volume 685, 8 February 2017, Pages 87-94, 2017.
27. L. Jemblie, V. Olden and O. M. Akselsen, A coupled diffusion and cohesive zone modelling approach for numerically assessing hydrogen embrittlement of steel structures, International Journal of Hydrogen Energy, 42(16), 11980-11995, 2017.
28. L. Jemblie, V. Olden, P. Mainçon, O.M. Akselsen, Cohesive zone modelling of hydrogen induced cracking on the interface of clad steel pipes, Int Journal of Hydrogen Energy, Vol 42, Issue 47, Nov. 2017, p 28622-28634.
29. L. Jemblie, V. Olden, B. Nyhus, O.M. Akselsen, Hydrogen embrittlement susceptibility of clad steel pipes, Paper No. PVP-2017-65247, ASME Pressure Vessels and Piping Conference, Waikoloa, Hawaii, USA, July 2017. Oral presentation and paper.
30. D. Lindholm, A methodology to Calculate Diffusion of Carbon across the Base-Clad Bimetallic Interface of Welded Offshore Clad Pipes, poster at Euromat, September 17-22, Thessaloniki, Greece
31. A. Alvaro, V. Olden, V. Osen, B. Nyhus, L. Jemblie, Hydrogen embrittlement in structural steel welds – Influence of varying the stress concentration, oral presentation at Euromat, September 17-22, Thessaloniki, Greece.
32. T. Coudert, X. Ren, P. Skjetne, S. Dumoulin, Modelling of cold metal transfer welding process using SPH, In proceedings of NWC 2017, NAFEMS World Congress, 11-14 June, Stockholm, Sweden
33. A. Utvær, FE simulation of hydrogen embrittlement on X60 clad pipe, using cohesive zone elements, NTNU Master thesis.

2018

34. L. Jemblie, Hydrogen embrittlement of clad steel pipes, Doctoral thesis at NTNU, 2018:200.
35. D. Lindholm, Carbon Diffusion across the Bimetallic Interface of Welded Clad Pipes, oral presentation and proceedings of the Twenty-eighth (2018) International Ocean and Polar Engineering Conference, Sapporo, Japan, June 10-15, 2018.
36. J-G. Sezgin, H. G. Fjær, H. Matsunaga, J. Jamabe, V. Olden, Hydrogen Trapping in X70 Structural Pipeline Steel and Weldments, Paper no. 1297, oral presentation and proceedings of the Twenty-eighth (2018) International Ocean and Polar Engineering Conference, Sapporo, Japan, June 10-15, 2018. Accepted for publication in the International Journal for Ocean and polar engineering.
37. D. Lindholm, Diffusjon av karbon i rørledninger av stål, oral presentation at Nasjonal konferanse for materialteknologi 2018, Oslo, 31. May.
38. L. Jemblie, V. Olden, B. Nyhus, A. Utvær, O.M. Akselsen, Hydrogen embrittlement susceptibility on the interface of clad steel pipes, before and after welding, oral presentation and proceedings of 3rd International conference on Metals & Hydrogen, Ghent, Belgium, 29.-31. May 2018.

2019-February 2020

39. V. Olden, Visualization of user-defined elements in ABAQUS, SINTEF Report 2019:00006.
40. Bunaziv, I., Aune, R., Olden, V., Akselsen, O.M. *Dry hyperbaric welding of HSLA steel up to 35 bar ambient pressure with CMT arc mode*. The International Journal of Advanced Manufacturing Technology 105(5-6), 2019; p. 2659-2676, doi: 10.1007/s00170-019-04511-6
41. Bunaziv, I., Akselsen, O.M., Olden, V. *Metallurgical aspects in welding of clad pipelines: – A global outlook*. Applied Sciences, 9(15), 2019; 3118, doi: 10.3390/app9153118
42. V. Olden, Knowledge basis for repair contingency of pipelines, final report, SINTEF Report 2019:00027 (this report).
43. R. Aune, Remotely Controlled Hyperbaric butt-welding for pipeline repair, Part I: Hyperbaric CMT root pass welding up to 150bar, SINTEF Report 2020:00235.
44. R. Aune, Remotely Controlled Hyperbaric Butt-welding for Subsea Pipeline Repair, Part II: Welding complete welds up to 150bar, SINTEF Report 2020:00236.

Workshops

- 1) SINTEF and NTNU's international Environmental Assisted Cracking workshop - SNEAC, Trondheim, 7-9 June 2016.
- 2) ROP Welding workshop on hyperbaric welding. 27. April 2017.

ⁱ V. Tvergaard, J. W. Hutchinson, The relation between crack growth resistance and fracture process parameters in elastic-plastic solids, *J. Mech. Phys. Solids*, Vol.40, No. 6. Pp 1377-1397, 1992.

ⁱⁱ Y. Lee, R. P. Gangloff, Measurement and modeling of hydrogen environment assisted cracking of ultra-high-strength steel, *Metall. Mater. Trans. A* 38 (13) (2007) 2174-2190. doi:10.1007/s11661-006-9051-z.

ⁱⁱⁱ British Standard BS 7448-1, Fracture mechanics toughness tests - Part 1: Method for determination of K_{Ic} , critical CTOD and critical J values of metallic materials (1991).



Technology for a better society

www.sintef.no

Appendix 1

2020:00339- Restricted

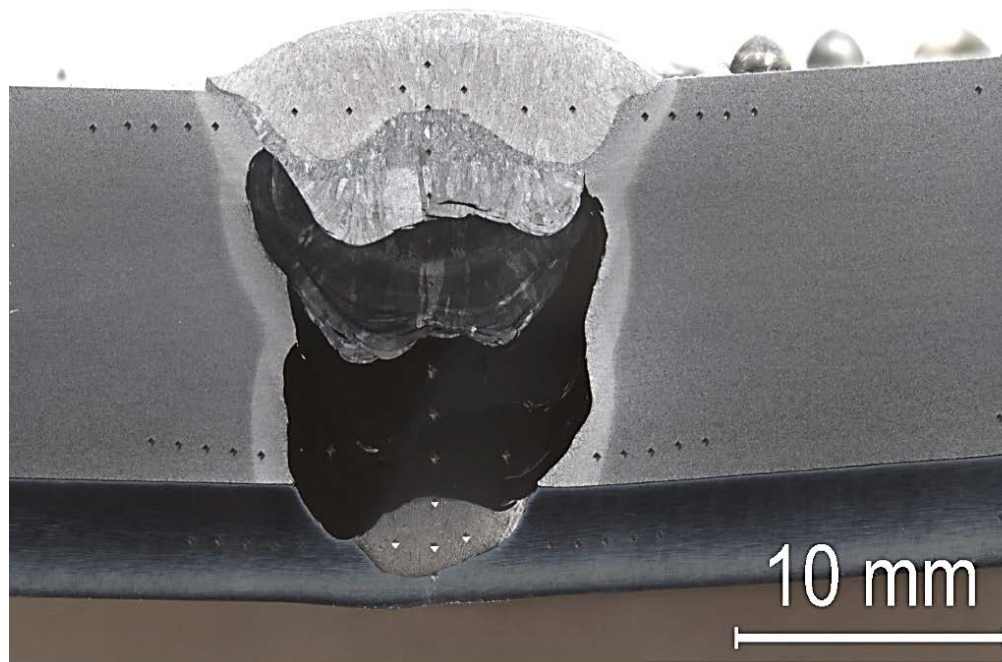
Report

Design build and installation of CMT hyperbaric welding chamber

HISC screening testing of FL and WM of CoreWeld and Alloy 59 filler materials

Author(s)

Bård Nyhus



Report

Design build and installation of CMT hyperbaric welding chamber

HISC screening testing of FL and WM of CoreWeld and Alloy 59 filler materials

KEYWORDS:

Keywords

Hyperbaric welding

Hydrogen embrittlement

HISC

VERSION

Version

DATE

2020-03-23

AUTHOR(S)

Bård Nyhus

CLIENT(S)

Equinor

CLIENT'S REF.

4502902771, Karl H. Ahlen

PROJECT NO.

102005947.

NUMBER OF PAGES/APPENDICES:

24 + Appendices

ABSTRACT

Abstract heading

This report presents the results from HISC screening testing of FL and WM of CoreWeld and Alloy 59 filler materials. The work is part of the project, "Design, build and installation of CMT hyperbaric welding chamber (Contract 4502902771 VO-4 and VO-6).

PREPARED BY

Bård Nyhus

SIGNATURE

**Nyhus
Bård**

Digitally signed by
Nyhus Bård
DN: cn=Nyhus Bård
Date: 2020.04.01
17:42:57 +02'00'

CHECKED BY

Ragnhild Aune

SIGNATURE

APPROVED BY

Magnus Eriksson

SIGNATURE

REPORT NO.

2020:00339

ISBN

ISBN

CLASSIFICATION

Restricted

CLASSIFICATION THIS PAGE

Restricted

Document history

VERSION	DATE	VERSION DESCRIPTION
Version 01.	2019-03-11	For Client review
Version 02	2020-03-23	Final version

Table of contents

1	Introduction	4
2	Material	4
3	Hydrogen charging	5
4	Test procedure	9
4.1	"Standard" HISC testing	9
4.2	Hydrogen measurement	11
4.3	HISC testing to check the effect of oversaturation	13
5	Results and Discussion	14
6	Conclusions	22
7	Suggestion to further work	23

APPENDICES

[List appendices here]

1 Introduction

This report presents the results from HISC screening testing of FL and WM of CoreWeld and Alloy 59 filler materials. The work is part of the project, "Design, build and installation of CMT hyperbaric welding chamber (Contract 4502902771 VO-4 and VO-6).

Equinor has experienced hydrogen assisted HUB failure between Inconel (625) buttering-welds and carbon steel (F22). Due to these failures it has been questioned if the same failure mechanisms can appear for hyperbaric welding of clad pipes. Hyperbaric welds are not coated, and the welds will therefore be exposed for hydrogen charging from cathodic protection. The material combination in the failed hubs is not the same as for the hyperbaric welds. The carbon steel in the HUB is typically F22, while in the clad pipes it is X-60/X-65 backing steel. The weld material is typically 625 for the HUB buttering welds, while it is alloy 59 in the hyperbaric welds in this study.

An alternative to use alloy 59 for the whole weld is to use it just in the root, where it is necessary for the internal corrosion resistance, and fill up the groove with carbon steel (CoreWeld) filler wire. The outer surface that is exposed to hydrogen charging will then be X-60/X65 backing steel with carbon steel filler wire. The experience with carbon steel in both base material and weld is good when it comes to HISC resistance. Such a weld will give complication to the welding because it is necessary to change filler wire, and it might also give unfavourable microstructure in the first layers with carbon steel that will be a mixture between CoreWeld and Alloy 59.

In this study the HISC properties have been studied for carbon steel welded with both CoreWeld and Alloy 59 filler material.

2 Material

In this study, the HISC properties on the external surface of the pipe for three different welds have been investigated

- Clad pipe with X-60 backing steel and Alloy 59 filler wire
- Clad pipe with X-60 backing steel, Alloy 59 in the root, Ni-1 for the 1st filler and then it is filled up with CoreWeld, see **Figure 1**
- X-70 pipe with CoreWeld filler wire

The welding is performed by SINTEF in the same project, but will be reported in a separate report.

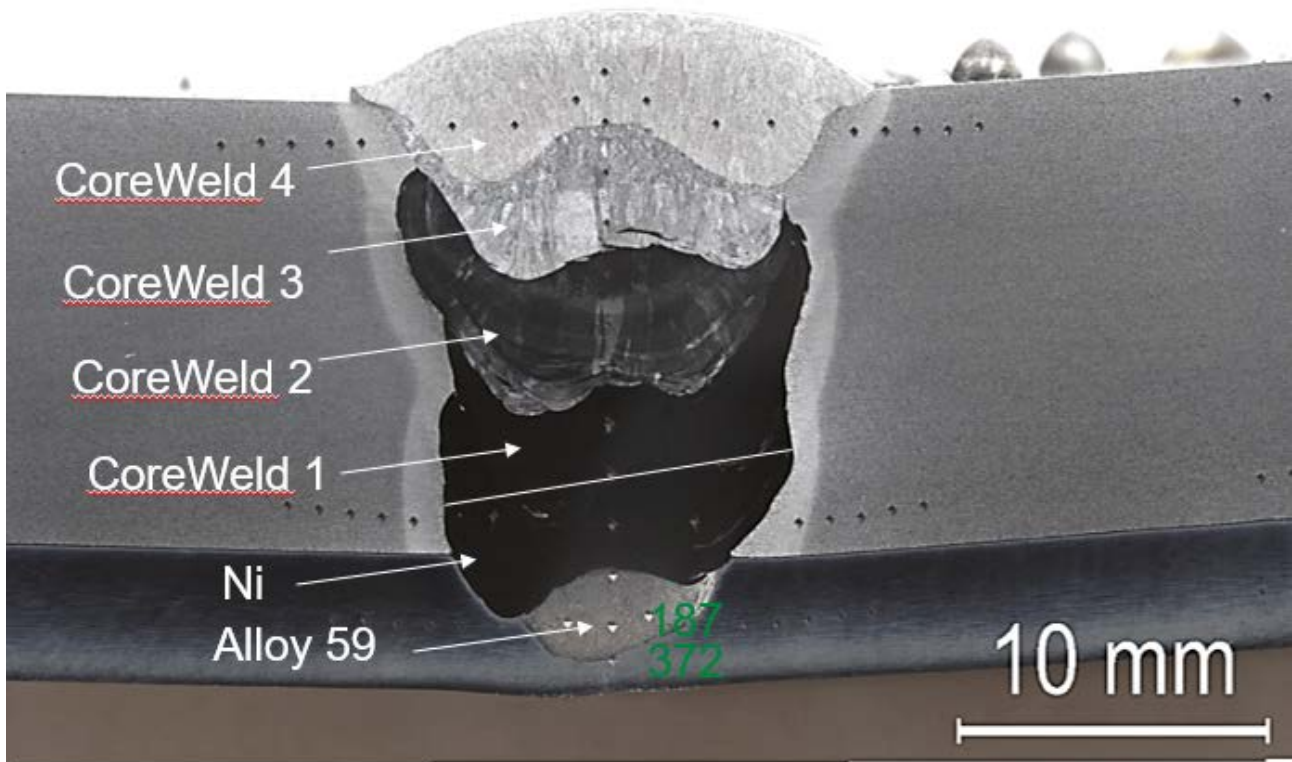


Figure 1 Clad pipe with X-60 backing steel, Alloy 59 in the root, Ni-1 for the 1st filler and then it is filled up with CoreWeld

3 Hydrogen charging

Cathodic protection of a hyperbaric weld that is not coated will cause hydrogen charging of the material. The BCC structure in the backing steel has a high diffusion rate and low saturation level, while the FCC structure in the filler material will have a low diffusion rate and a high saturation level. For both materials the diffusion rate and saturation level will increase with temperature.

In Figure 2 - Figure 4, the assumed lattice hydrogen charging from CP is sketched for a weld. It is further assumed that the weld consists of weld material (FCC) and base material (BCC) with homogenous microstructure. Different microstructure in HAZ is not included. It is also assumed that subsurface hydrogen level in the outer surface is constant (different levels for weld metal (WM) and base material (BM)). On the inner side there are no hydrogen source and the subsurface hydrogen content on the inner side is therefore set to zero.

Figure 2 show the hydrogen charging over the wall thickness for a pipe without clad. The outer subsurface saturation level is low in BM compared with WM, but due to much faster diffusion rate in BM, a steady state diffusion profile is reached much earlier in base material than in WM. The steady state is normally assumed to be a straight line for lattice diffusion in a homogenous material. The hydrogen profiles illustrate why HISC usually starts from the exposed surface for pipelines. The outer surface is fully exposed for HISC from the start. The hydrogen content deeper into the material is increasing with time, but even at steady state the hydrogen content is decreasing with distance from the outer surface as illustrated with red curves in Figure 2.

In Figure 3 the diffusion for a clad pipe is illustrated. The conditions are identical, except that the pipe has an internal clad (FCC). Hydrogen diffusion in the clad is much slower than in the backing still, resulting in a steady state where the hydrogen level in the backing steel is equal to the outer subsurface for all the backing steel. The whole hydrogen gradient to the inner surface will be taken by the clad layer that act as a barrier for the hydrogen diffusion. The clad might influence the risk for HISC after long time of charging. The risk for HISC in the outer exposed surface is not influenced by the clad, but in difference to pipes without clad, the hydrogen level of the outer surface will be reached in all the backing steel. Since the backing steel next to the weld is so high at steady state, the steady state level in weld metal will also be high through most of the wall thickness, see Figure 3.

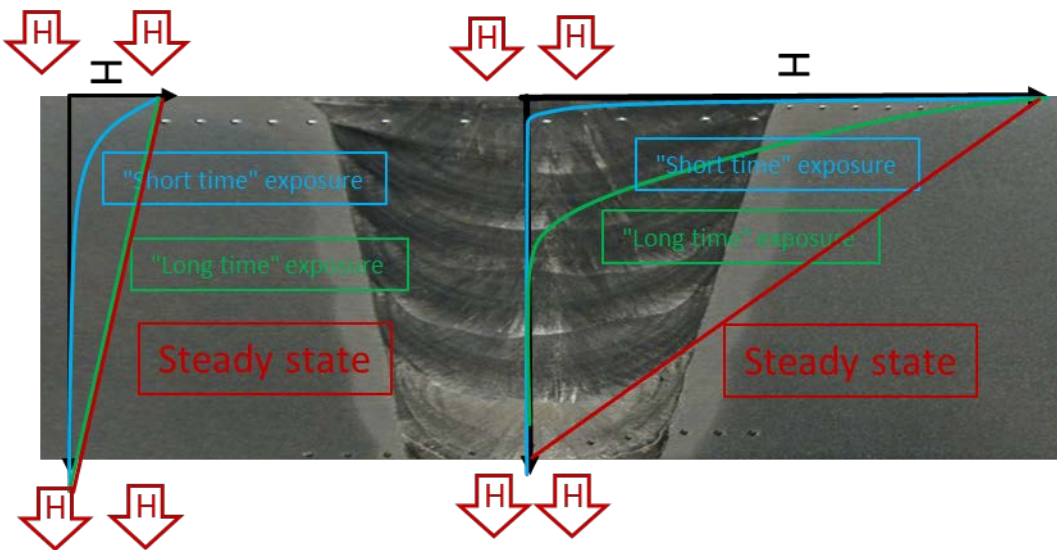


Figure 2 Schematic illustration of hydrogen charging in base metal (BCC) and weld metal (FCC)

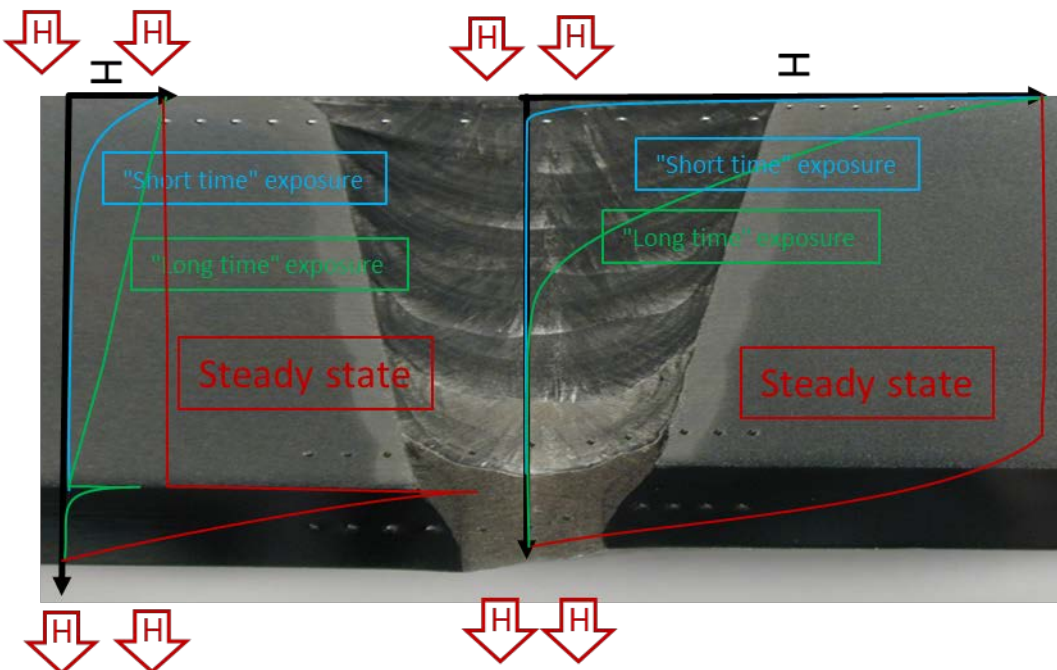


Figure 3 Schematic illustration of hydrogen charging of pipeline with a FCC clad, backing steel (BCC) and weld metal (FCC).

Figure 4 show the hydrogen profiles transverse to the weld (mid thickness) for a clad pipe. The red curve indicates steady state hydrogen level at "high" temperature during operation. The blue curve illustrates steady state hydrogen level at "low" temperature. The steady state hydrogen level in both BM and WM is decreasing with decreasing temperature.

The yellow curve is indication hydrogen level after a temperature decrease before a new steady state is reached. A hypothesis is that you might get an increased hydrogen level in HAZ temporary because the oversaturation in WM will cause and increased diffusion out of weld metal.

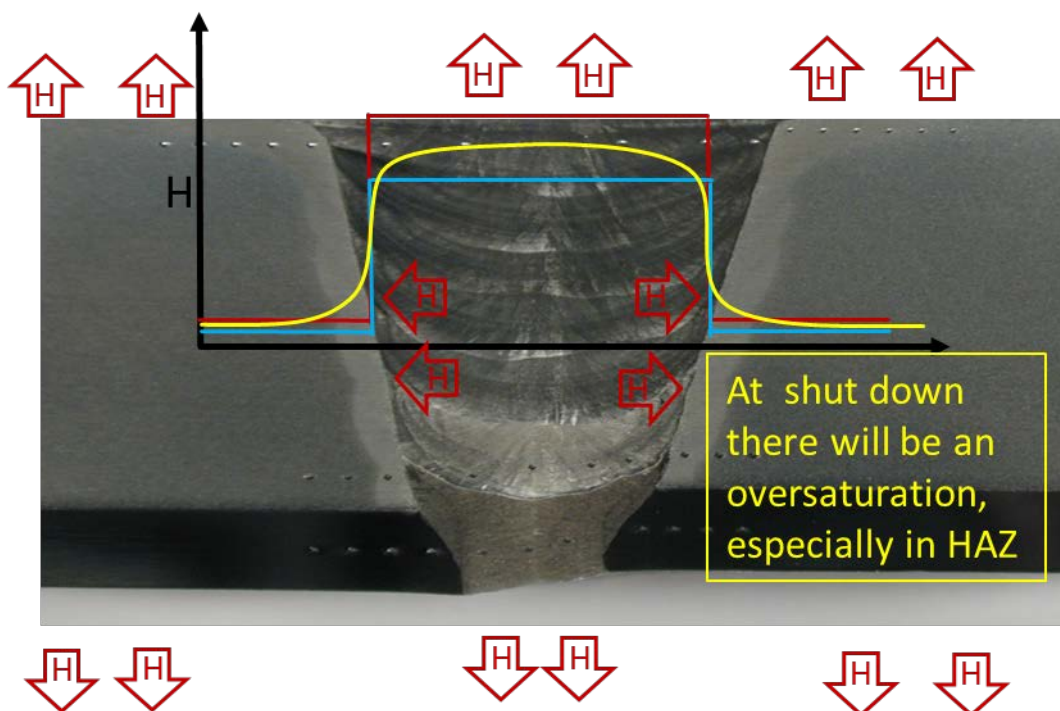


Figure 4 Schematic illustration of hydrogen redistribution after cooling in a clad pipe.

The locally high oversaturation of HAZ might be an important reason for hydrogen assisted failures of hubs during shutdown.

Hypothesis for hydrogen assisted HAZ failures of HUBS at shutdown:

1. Locally high oversaturation of HAZ/Fl during shutdown as illustrated in Figure 4.
2. HAZ/FL is more sensitive to HISC than BM and WM
3. The hydrogen level in HAZ/FL might be higher than BM, due to more traps, before shutdown. This is not illustrated in Figure 2 - Figure 4
4. The oversaturation will be highest in the mid thickness of the wall since the diffusion way is longer than at the surface. This fits with observation of HUB failure not starting from the surface, see Figure 5
5. The clad will give a high steady state hydrogen level in both HUBs (Figure 5) and in clad pipelines in most of the wall thickness as illustrated in Figure 3.

In the above, a hypothesis for the hydrogen assisted HUB failures is presented. It is also described the similarities between the HUBs and hyperbaric welds. It is, however, important to be aware that it is differences in the materials and welding procedures.



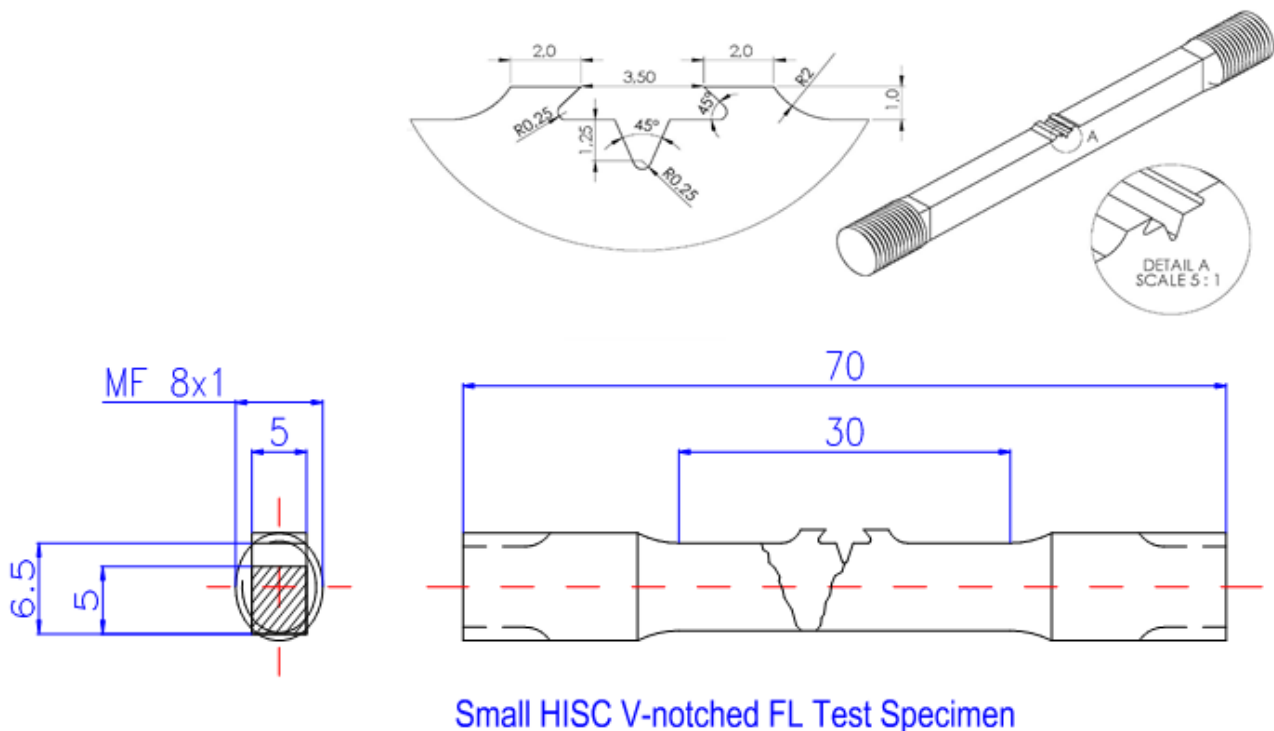
Figure 5 Picture of a hydrogen assisted failure of a HUB.

It is a challenge to perform testing to investigate the fracture mechanism discussed above. This is because it is necessary to saturate the material with hydrogen, and this was assumed to be difficult with the time and budget in this project. It was therefore decided to do some standard HISC testing in accordance to the procedure developed in the HISC 2-4 projects. This procedure does not include the effect of temperature changes. To address the effect of temperature changes, small pieces of BM and WM was charged with hydrogen at different temperature history to indicate the potential effect of temperature drop.

4 Test procedure

4.1 "Standard" HISC testing

- The geometry of the HISC specimens is given in Figure 6. The notch is in accordance to the V-notch established in the HISC2-4 projects. The notch is designed to give a lower bound undercut in the weld toe.
- All specimens are machined with the notch is as close as possible to the exposed outer surface as possible, see **Figure 7**.
- The notch was positioned in both WM and HAZ, the test matrix is given in Table 1.
- The specimens were precharged prior to testing at 80°C for 14 days in 3% NaCl solution, polarised to -1050 mV SCE
- All the HISC testing is based on the HISC test procedure (for Screening tests) established in the HISC2-4 projects.:
 - Test specimens exposed in slowly flowing 3% NaCl solution at 4°C
 - Specimens continuous polarised to -1050 mV SCE
 - Loading:
 - Loading up to a net section stress equal to 86% of the yield stress
 - 2% increase of the load every second day until failure



Small HISC V-notched FL Test Specimen

Figure 6 Geometry of HISC specimens

Table 1 Overview of the test matrix for "standard" HISC testing

Material	Material code	Spec. ID	Precharging	Loading
Coreweld /X-70	A35-2	A1 HAZ A2 WM	14 days, 80C	Stepwise loading to failure
Alloy 59 filler	B5-2	B1 HAZ B2 WM		
Alloy 59+Coreweld/X-65Clad	E5-1	E1 HAZ E2 WM		



Figure 7 Picture showing that specimens are machined, so that the notch is as close external surface of the pipe as possible

The stepwise loading is based on an extensive testing of SDSS/DSS and SMSS materials in the HISC2-4 projects. These experiments concluded that 2 days at every load level is enough to trigger HISC, if the load is above the threshold load for HISC. 2 days is not enough to saturate the bulk material, but the test results indicated that it is enough time to saturate the process zone (indicated with red in Figure 8). The same stepwise loading rate is used in this project, but it is not verified by testing that it is enough to saturate the process zone in Alloy 59 filler material.

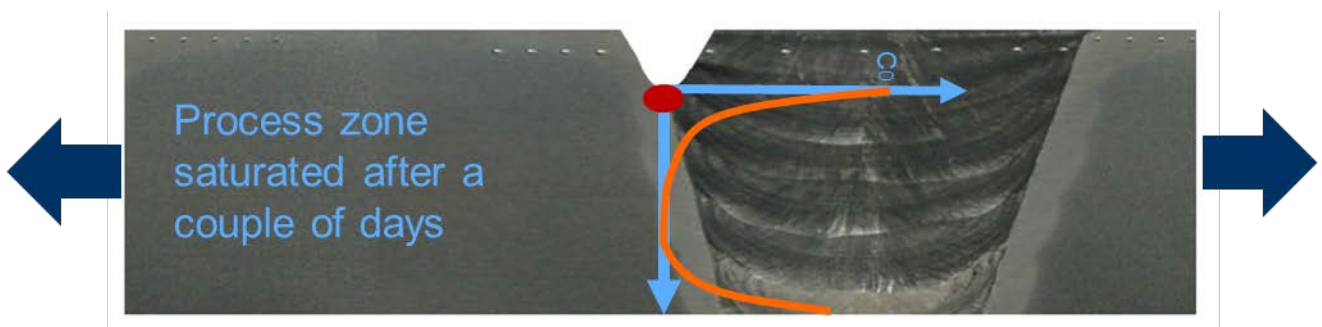


Figure 8 Illustration of the hydrogen profile in a specimen, where it is just the process zone that is saturated with hydrogen

The precharging and loading is illustrated in Figure 9

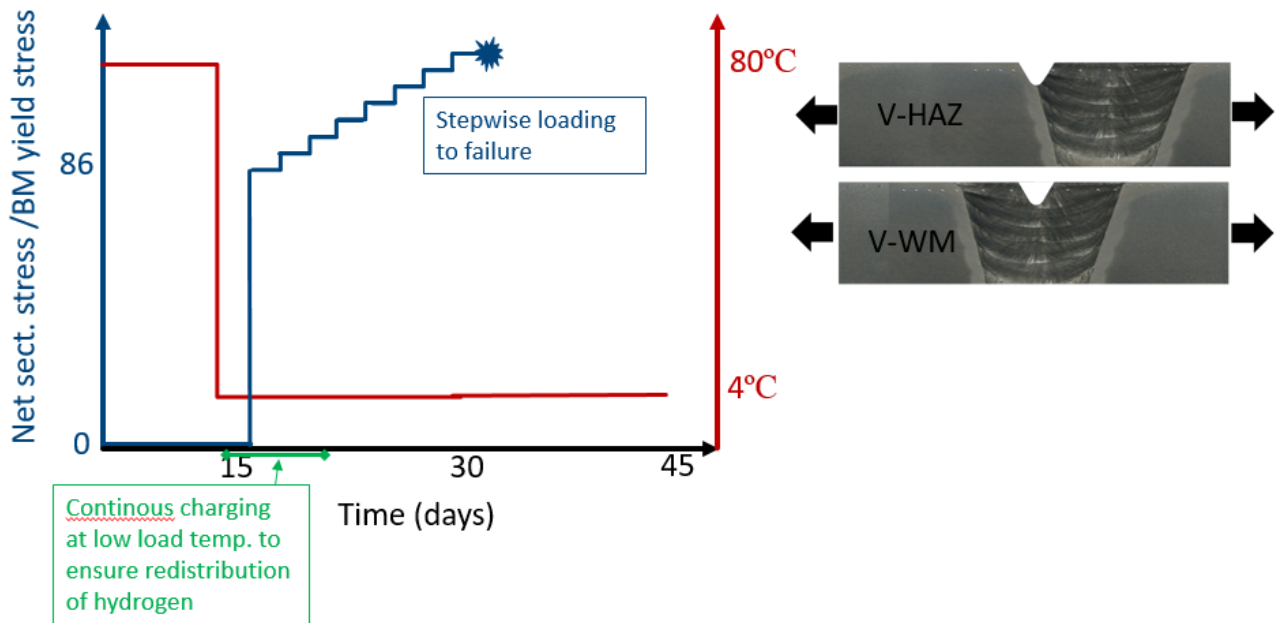


Figure 9 Sketch showing temperature and loading versus time.

4.2 Hydrogen measurement

The HISC testing above do not include the potential effect of oversaturation in combination with a temperature drop (shut down). HISC testing of this failure mechanism is challenging because it needs a long time of precharging to saturate the bulk material. Instead, charging and hydrogen measurements of small pieces was performed to give an indication if the effect of oversaturation of HAZ is likely to occur. Figure 10 sketch the testprogram and assumed hydrogen level as a function of temperature and time. The idea was to precharge small pieces of X-60 (BM) and Alloy59 (WM) at 80°C, and then reduce the temperature to 4°C to see if the hydrogen level decreases. If there is a "significant" drop in the hydrogen level it will indicate that there will be an oversaturation that can cause HISC. If the drop in alloy 59 is high compared to X-60 it will indicate that hydrogen will diffuse from WM to HAZ and cause higher oversaturation in HAZ compared to WM and BM.

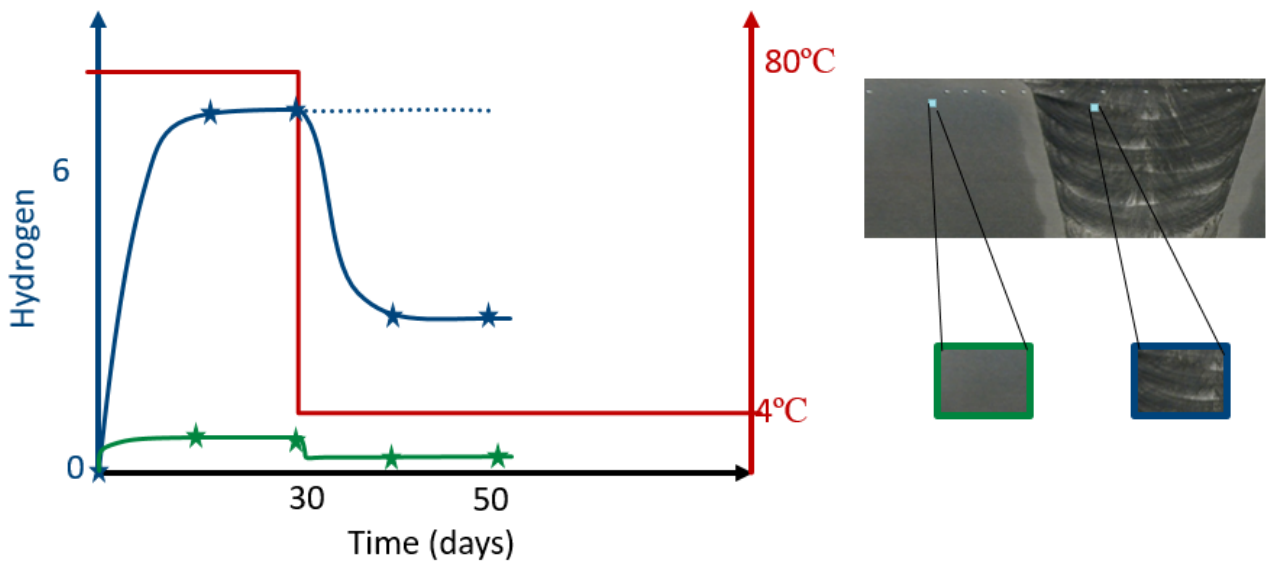


Figure 10 Sketch showing temperature and assumed hydrogen content versus time.

Pictures from the precharging is shown in Figure 11. The charging pieces was made so small that they could be analysed for hydrogen content without any cutting. Short time between charging and hydrogen measurements is important to minimize loss of hydrogen. The small size of the pieces will also reduce the charging time to saturation. The hydrogen was measured by melt extraction.

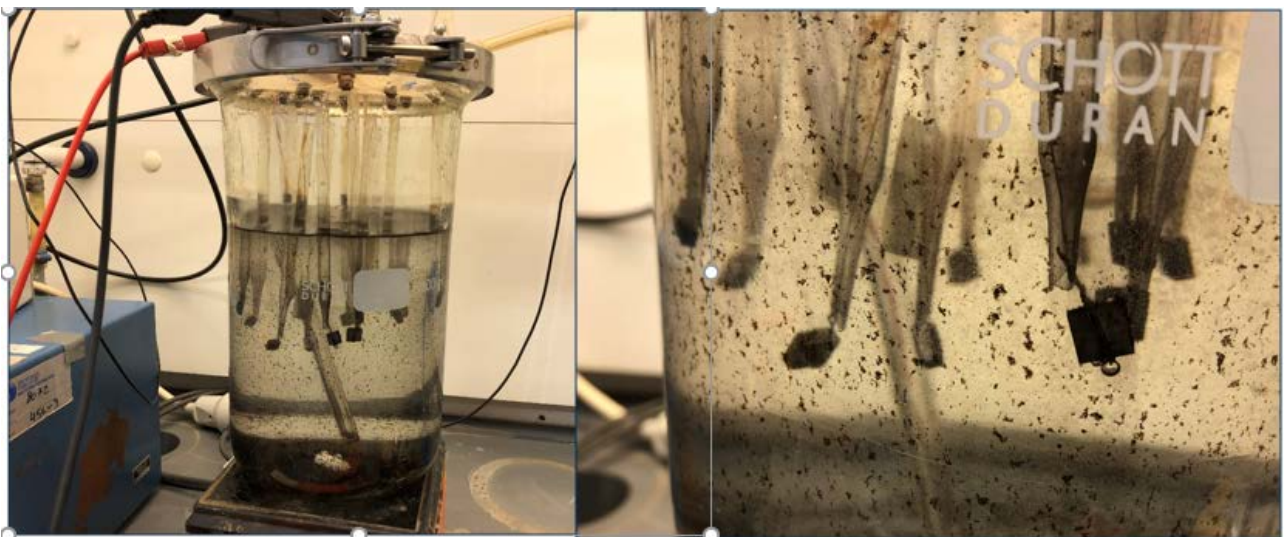


Figure 11 Picture of the precharging

Table 2 gives an overview of the pieces that were charged for hydrogen measurement

Table 2 Overview of the hydrogen charged test pieces.

Sample ID	Material and precharging
3	Alloy 59: filler, No charging (reference)
7	
10	Alloy 59: Sample charged at 80°C for 1 week
14	
1	Alloy 59: Sample charged at 80°C for 2 weeks
2	
5	
4	Alloy 59: Samples charged at 80°C for 2 week and at 4°C for 1 week
6	
8	
9	
11	
13	
B16	X-60 backing steel: filler, No charging (reference)
B14	
B10	X-60 backing steel: Samples charged at 80°C for 1 week
B12	
B1	X-60 backing steel: Samples charged at 80°C for 2 weeks
B2	
B3	
B4	X-60 backing steel: Samples charged at 80°C for 2 week and at 4°C for 1 week
B5	
B6	
B7	
B8	

A new test series with increased charging time was started, but it was revealed that the electric contact between the platina wire and the material pieces was lost after long time of charging. The hydrogen level was therefore not measured.

4.3 HISC testing to check the effect of oversaturation

It was decided to do two extra HISC tests, with a "long" charging time at high temperature (63 days at 80°C) and then cool the specimens down to 4°C and load the specimens to failure, when it is still an oversaturation in the specimens. The testing was performed despite it is an uncertainty if there has been a loss of electric

contact between the platina wires and the specimens as happened for the small charging pieces that was charged for "long" time.

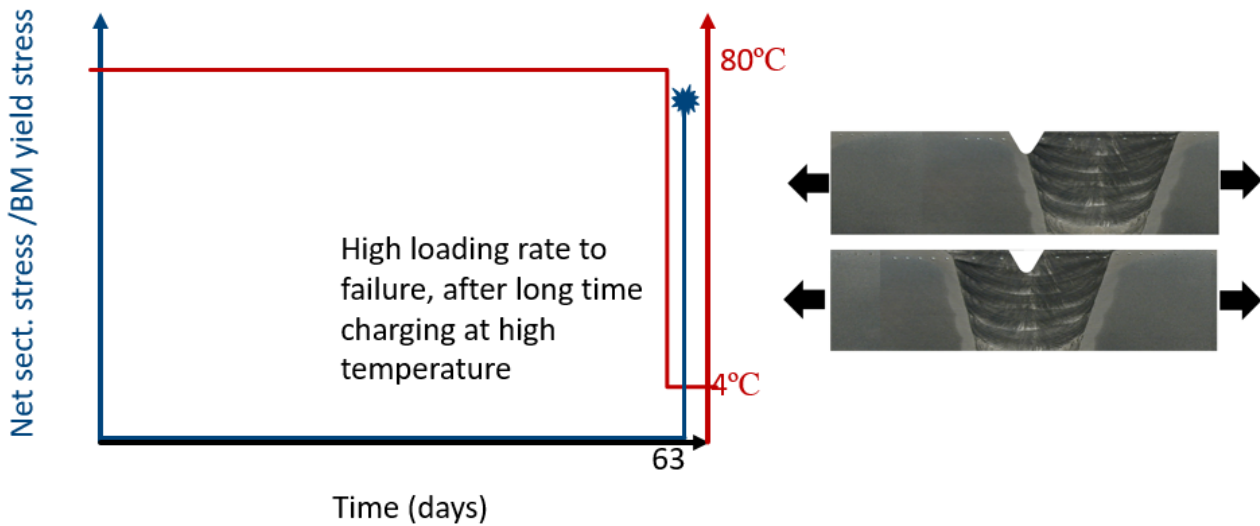


Figure 12 Sketch showing temperature and loading versus time to investigate effect of oversaturation of hydrogen after a temperature drop.

5 Results and Discussion

The results from the "standard" HISC testing of clad material is given in Figure 13 and Figure 14 with different pictures of the specimens after failure.

Table 3 Overview of test results from the HISC testing

Material	Material code	Spec. ID	Pre-charging	Loading	Net section failure stress	Net sect. failure stress/ Yield stress (BM)
Coreweld /X-70	A35-2	A1 HAZ	14 days, 80C	Stepwise loading to failure	569 MPa	1,16
		A2 WM			570 MPa	1,16
Alloy 59 filler	B5-2	B1 HAZ			578 MPa	1,18
		B2 WM			628 MPa	1,28
Alloy 59+Coreweld/ X-65Clad	E5-1	E1 HAZ			423 MPa	0,86
		E2 WM			499 MPa	1,02
Alloy 59 filler	B5-2	B3 HAZ	63 days, 80C	Rapid loading to failure	639 MPa	1,30
		B4 WM			623 MPa	1,27

The load versus time for the "standard" HISC testing of clad material is given in Figure 13 and Figure 14. The specimens with Alloy 59 filler material showed a high load capacity and ductile behaviour for both HAZ and WM. For the specimen with notch in HAZ the net section failure stress was 578 MPa, 18% higher than the BM yield stress. The specimen with the notch in the Alloy 59 filler material failed at a net section stress of 628 Mpa, 28% higher than the BM yield stress. The specimens showed no sign of reduced load or strain capacity due to HISC.

For the clad pipe welded with alloy 59 in the root, Ni-1 (1st filler) and then filled up with CoreWeld failed in a brittle manner at "low" loads, see Figure 13 and Figure 14. The specimen with notch in HAZ failed outside the notch at 423 MPa at the initial load level, 86% of BM yield stress. The specimen with notch in the CoreWeld filler material failed at 499 MPa, 2% higher than BM yield stress. The hardness of weldmetall is given in Figure 15. The first CoreWeld filler will have a high content of Ni and the hardness is low. For the second CoreWeld filler the hardness is high, and it is expected to have a low toughness. For the 3 filler the hardness drops to more expected values for CoreWeld filler material. Both the microstructure and the hardness for the 4th filler looks normal for a CoreWeld filler material. It is obvious that material from Alloy59 (root pass) and Ni-1 from the 1st filler, mix and are devastating for the microstructure in several of the following CoreWeld filler layers. More information about the welding will be reported in a separate report.

In Figure 16 it is a picture of the specimen (E5-1 E1 HAZ) that failed outside the notch. In Figure 17, the picture of the specimen (Figure 16) and the microstructure (Figure 15) is combined. It can be seen that the underside of the test specimen is in the most brittle part of the weld (CoreWeld 2 with Vickers hardness of 372), the failure started in this area. This show that the toughness in CoreWeld2 is extremely brittle and HISC sensitive.

Before the testing it was believed that the last CoreWeld fillers where the notch is located was not influenced by the Alloy59 in the root and Ni-1 in the 1st filler. The macro and test results show that the Alloy59 and Ni-1 layer is devastating for the properties in the CoreWeld fillers. Further work to improve the welds will be reported separately. CoreWeld filler is normally assumed to be little sensitive to hydrogen from CP.

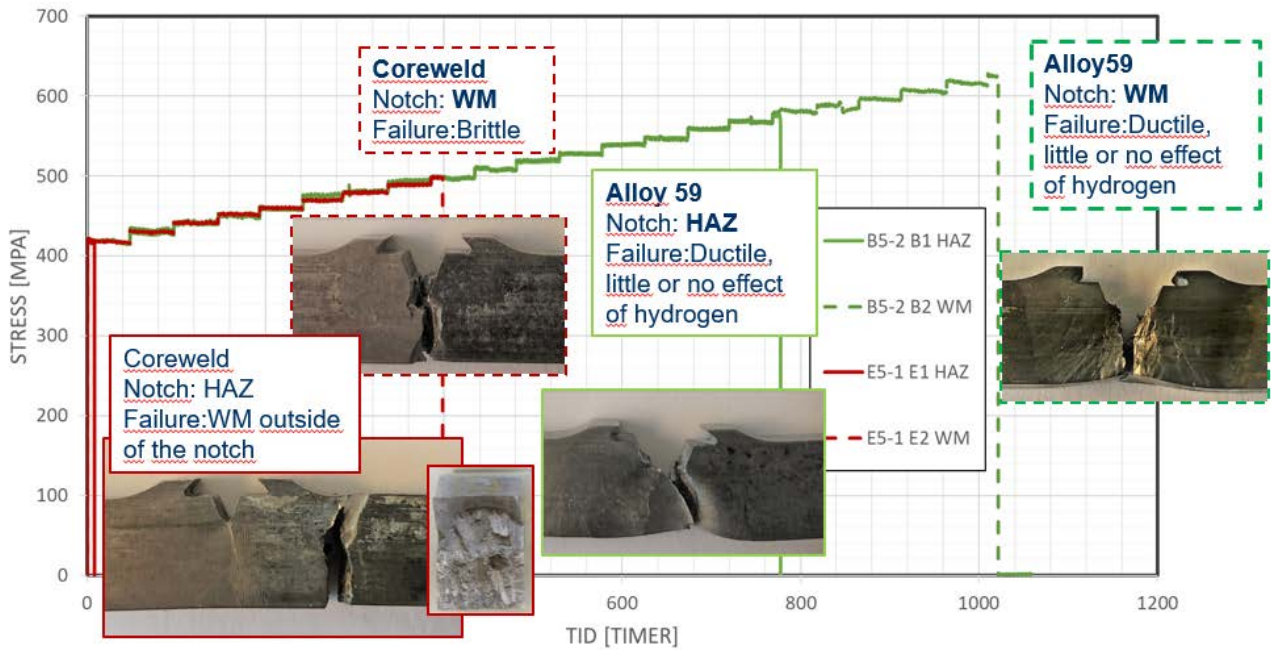


Figure 13 Load versus time for "standard" HISC testing of clad pipes

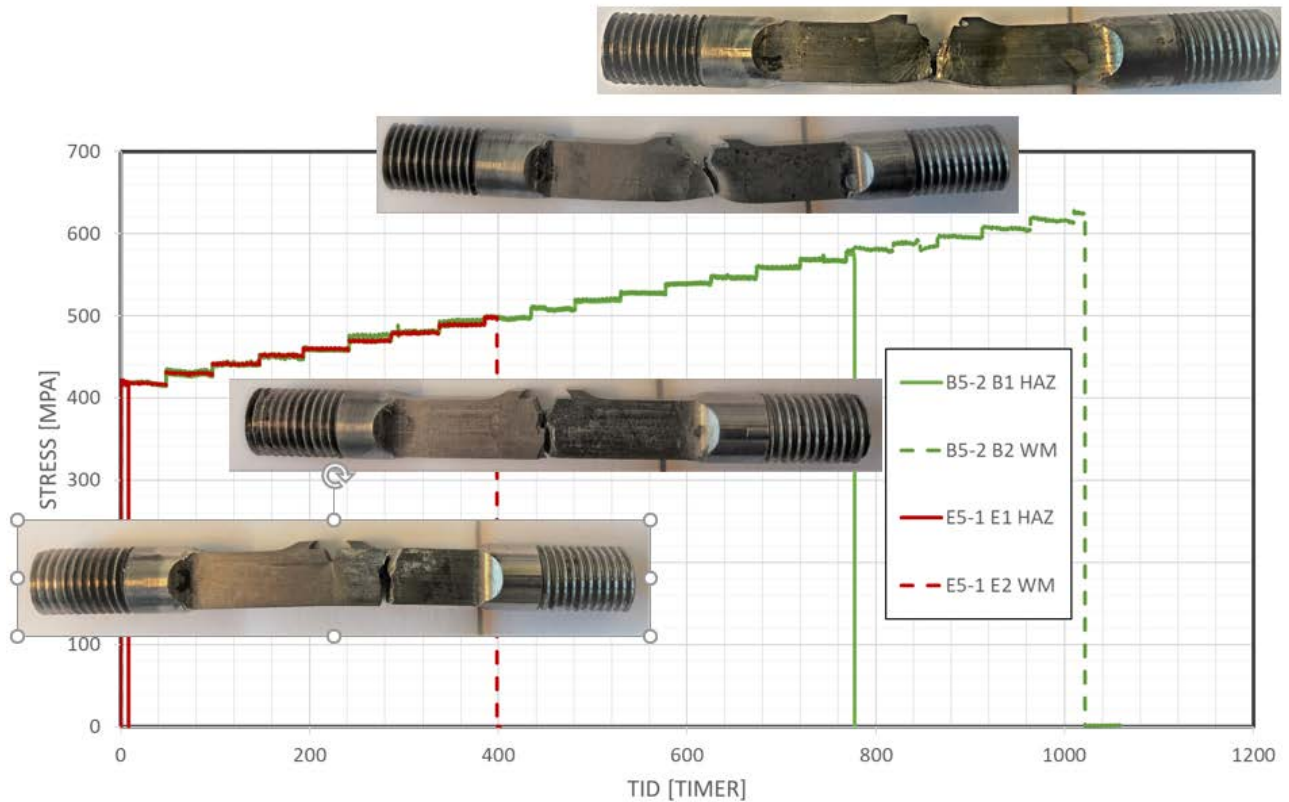


Figure 14 Load versus time for "standard" HISC testing of clad pipes (same results as in Figure 13).

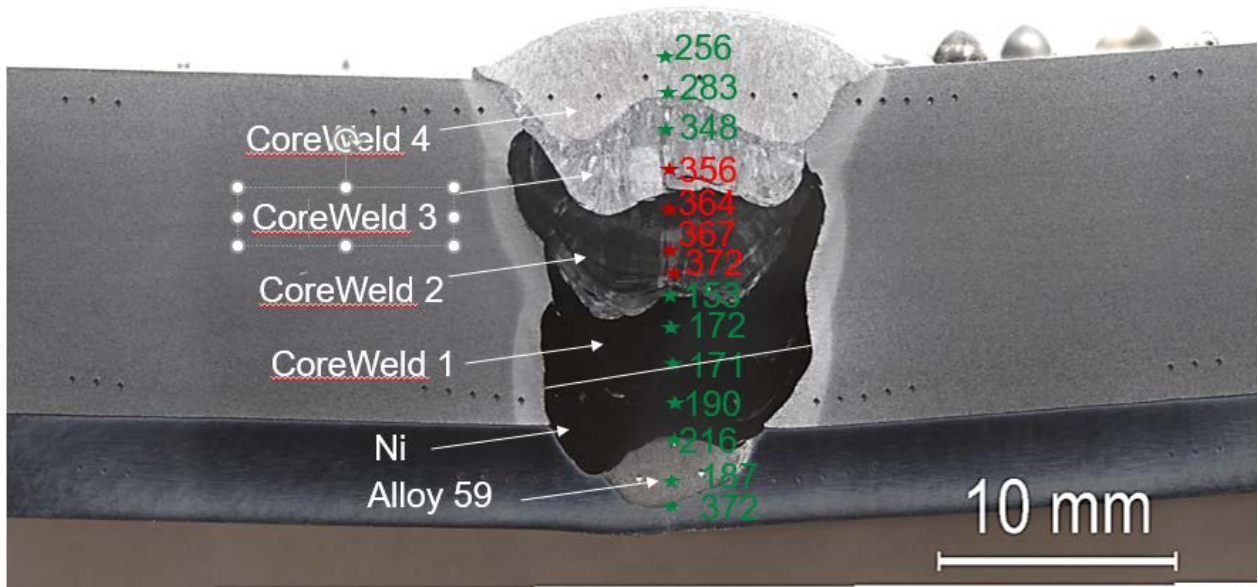


Figure 15 Macro of the clad pipe weld with alloy 59 in the root, Ni-1 (1st filler) and then filled up with CoreWeld.



Figure 16 Picture of specimen E5-1 E1 HAZ (failure outside the notch)

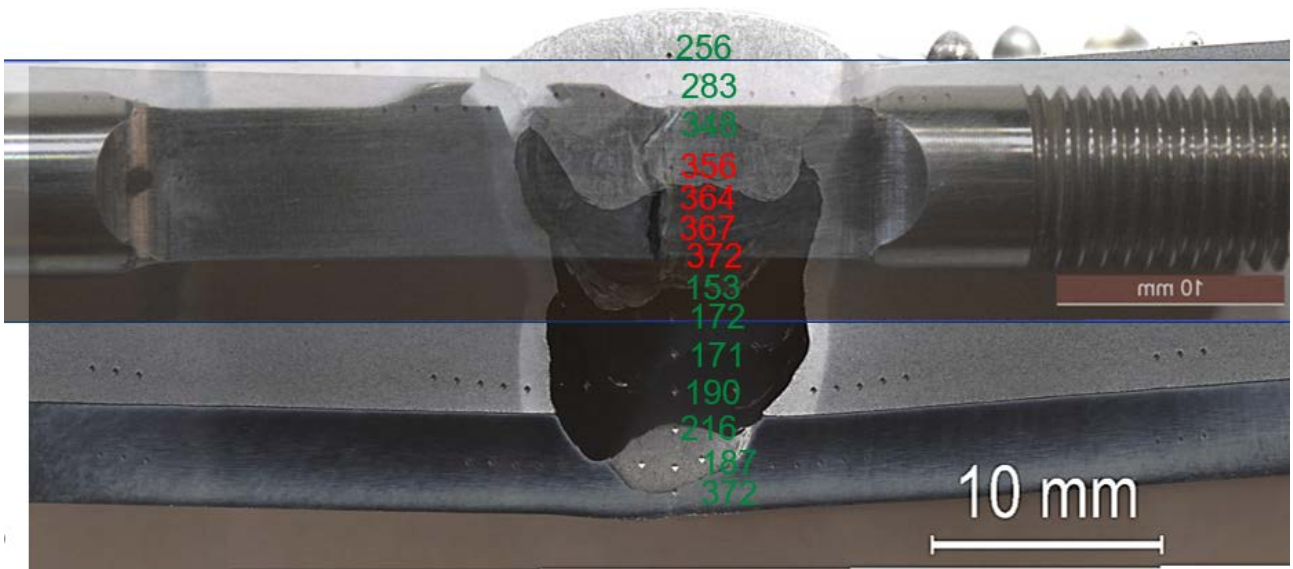


Figure 17 Combination of Figure 15 and Figure 16 to see the microstructure in the HISC specimen.

In Figure 18, the results from HISC testing of a X70 pipe with CoreWeld filler material is included in the load versus time plot. The net section failure load was 569 MPa with the notch in HAZ (dotted blue curve) and 570 MPa with the notch in CoreWeld (solid blue curve). The load capacity is high, and the material is not very sensitive to HISC. The solid blue curve (notch in "pure" CoreWeld) show the potential for improvement of the "diluted" CoreWeld (dotted red curve)

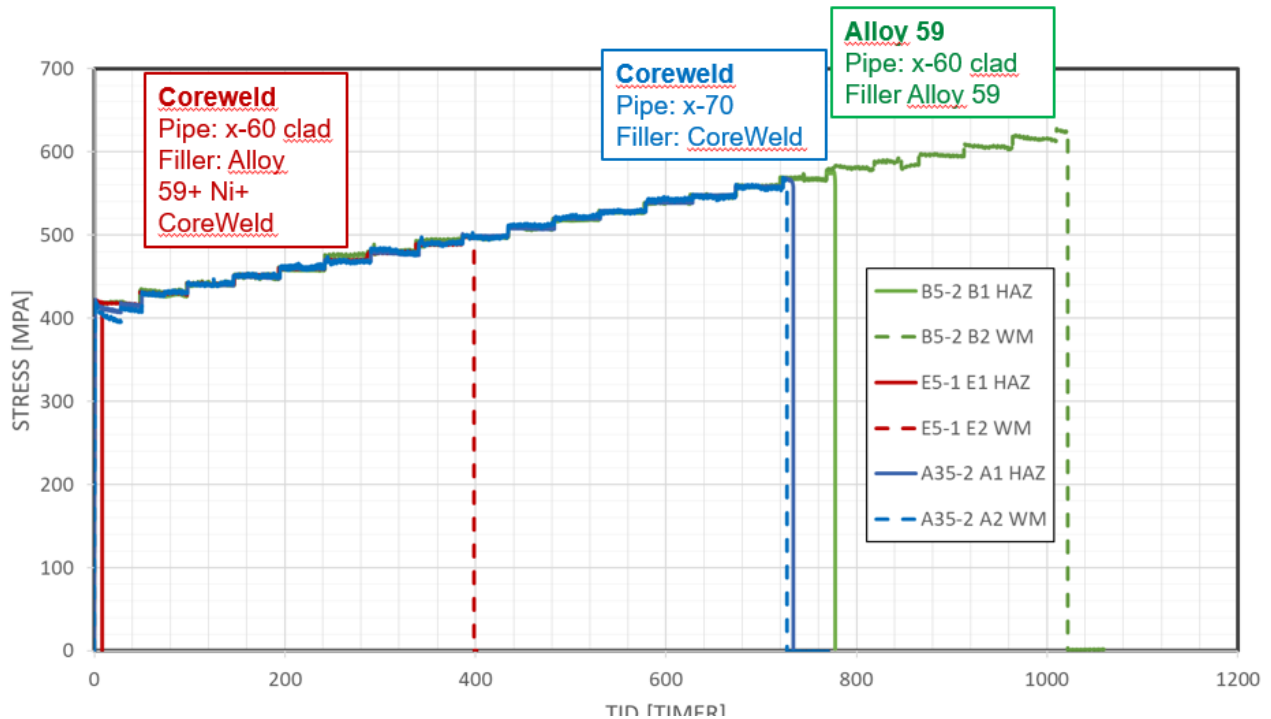


Figure 18 Test results for the "standard" HISC testing

Two specimens from the Clad pipe welded with Alloy 59 was precharged for 63 days, rapid cooled and the "rapid" loaded to failure to see if there was an effect of oversaturation due to the rapid temperature drop. The results are plotted in Figure 19 together with the standard HISC tests. To improve the comparison with the other results, the x-axes has a logarithmic scale. The specimens that was rapid loaded (1,5 h to failure) after precharging at 80°C for 63 days (light green curves) show the same load capacity as the "standard" HISC specimens (dark green curves).

Despite that there was no reduction in load capacity after a temperature drop, it cannot be concluded that the oversaturation theory is not valid. More work is needed before this can be concluded. It is mainly two reasons for this, the time to saturate the bulk material is probably too short, and in addition there was problems with the electric contact between the platina wire connected to the specimen for the long-term charging (63 days).

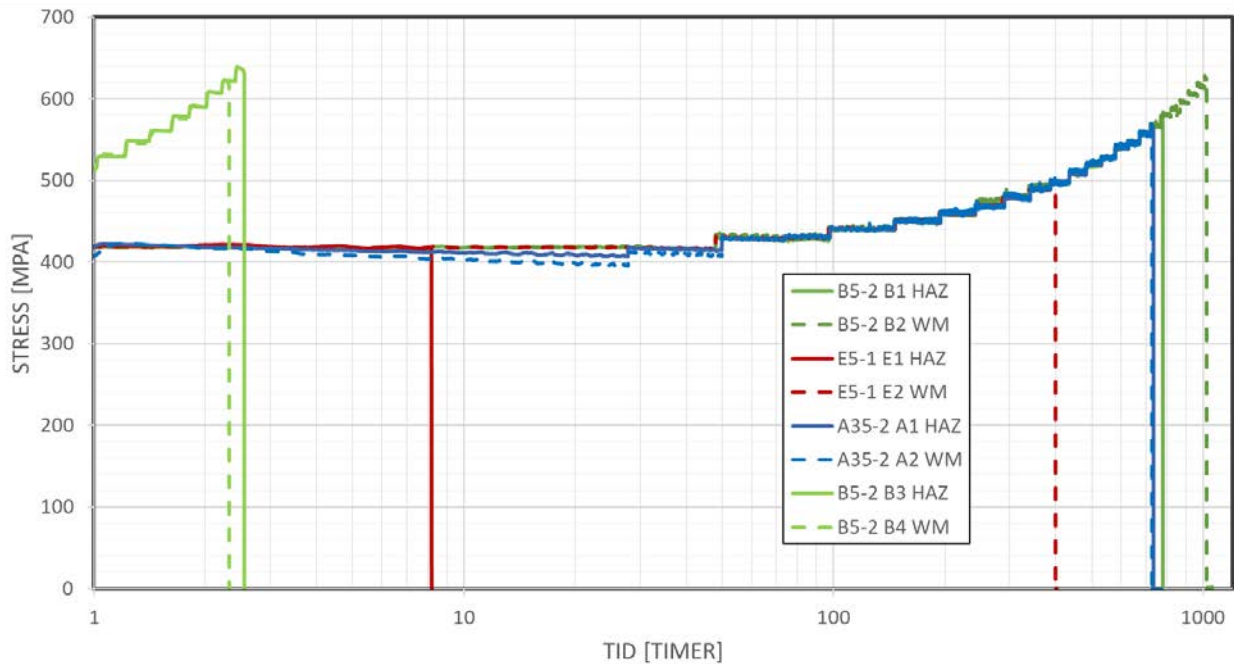


Figure 19 Test results for all the HISC tests (X-axis is logarithmic).

The hydrogen measurements of precharged small pieces of X-60 backing steel and the Alloy 59 filler material is presented in Figure 20 and Table 4. The aim was to study a potential hydrogen drop after a temperature drop. For the X-60 material, the time to saturation, and the saturation level was expected to be low. The hydrogen level in the X-60 was measured to 1.2 to 4.4 wppm which is as expected, but the scatter in the results makes it difficult to establish a clear effect of charging time and temperature.

For the Alloy 59, it is a clear trend that the hydrogen level is increasing with precharging time at 80°C and that it drops when the temperature is reduced to 4°C. The results support the hypothesis that oversaturation might be an issue after a temperature drop (shut down). The holding time is probably too short to give a saturation level for both 80°C and 4°C. A possible reason for the drop in hydrogen, when the temperature drops is that the subsurface hydrogen level is reduced, and that this gives a reduction in hydrogen level despite that the core of the piece is continuous increasing. Longer charging time is needed to get confidence of the saturation levels for the two temperatures.

Table 4 Results from hydrogen measurements of precharged small pieces of X-60 and Alloy59.

Sample ID	Material and precharging	Result (wppm)	AVG Result (ppm)
3	Alloy 59: filler, No charging (reference)	3,09	3,2
7		3,31	
10	Alloy 59: Sample charged at 80°C for 1 week	25,4	22,9
14		20,4	
1	Alloy 59: Sample charged at 80°C for 2 weeks	34,9	33,9
2		34,4	
5		32,5	
4	Alloy 59: Samples charged at 80°C for 2 week and at 4°C for 1 week	29,1	27,9
6		28,0	
8		27,6	
9		29,2	
11		24,5	
13		29,1	
B16	X-60 backing steel: filler, No charging (reference)	1,5	1,4
B14		1,3	
B10	X-60 backing steel: Samples charged at 80°C for 1 week	1,2	1,9
B12		2,5	
B1	X-60 backing steel: Samples charged at 80°C for 2 weeks	1,8	2,8
B2		4,4	
B3		2,1	
B4	X-60 backing steel: Samples charged at 80°C for 2 week and at 4°C for 1 week	2,2	3,4
B5		2,1	
B6		4,3	
B7		4,4	
B8		3,8	

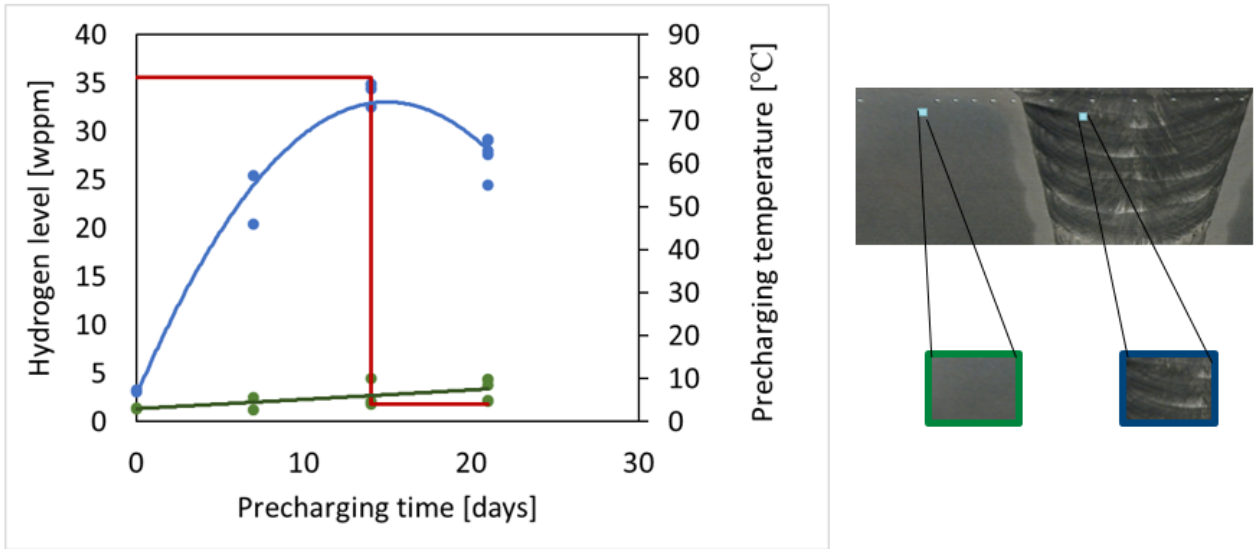


Figure 20 Results from hydrogen measurements of precharged small pieces of X-60 and Alloy59.

6 Conclusions

Equinor has experienced hydrogen assisted HUB failure between Inconel (625) buttering-welds and carbon steel (F22). Due to these failures it has been questioned if the same failure mechanisms can appear for hyperbaric welding of clad pipes. The Clad pipes has x-60/x-65 backing steel and Alloy 59 filler material.

To avoid Alloy 59 in the external hydrogen exposed surface, welding was performed with Alloy 59 in the root, Ni-1 in the 1st pass, and then the groove was filled with 4 passes with CoreWeld. CoreWeld in the outer surface is assumed to have high resistance to HISC.

In this study, the HISC properties on the external surface of the pipe for three different welds have been investigated

- Clad pipe with X-60 backing steel and Alloy 59 filler wire
- Clad pipe with X-60 backing steel, Alloy 59 in the root, Ni-1 for the 1st filler and then it is filled up with CoreWeld
- X-70 pipe with CoreWeld filler wire

The HISC properties based on "Standard" HISC testing showed excellent resistance against HISC for the Clad pipes welded with Alloy 59 and the X-70 pipe welded with CoreWeld.

The clad pipe welded Alloy 59 in the root, Ni-1 for the 1st filler and then filled up with CoreWeld gave very brittle and hydrogen sensitive microstructure in the Coreweld filler number 2 and 3. Research to improve the quality of the weld is performed in the project, but it will be reported in a separate report. No additional HISC testing has been performed.

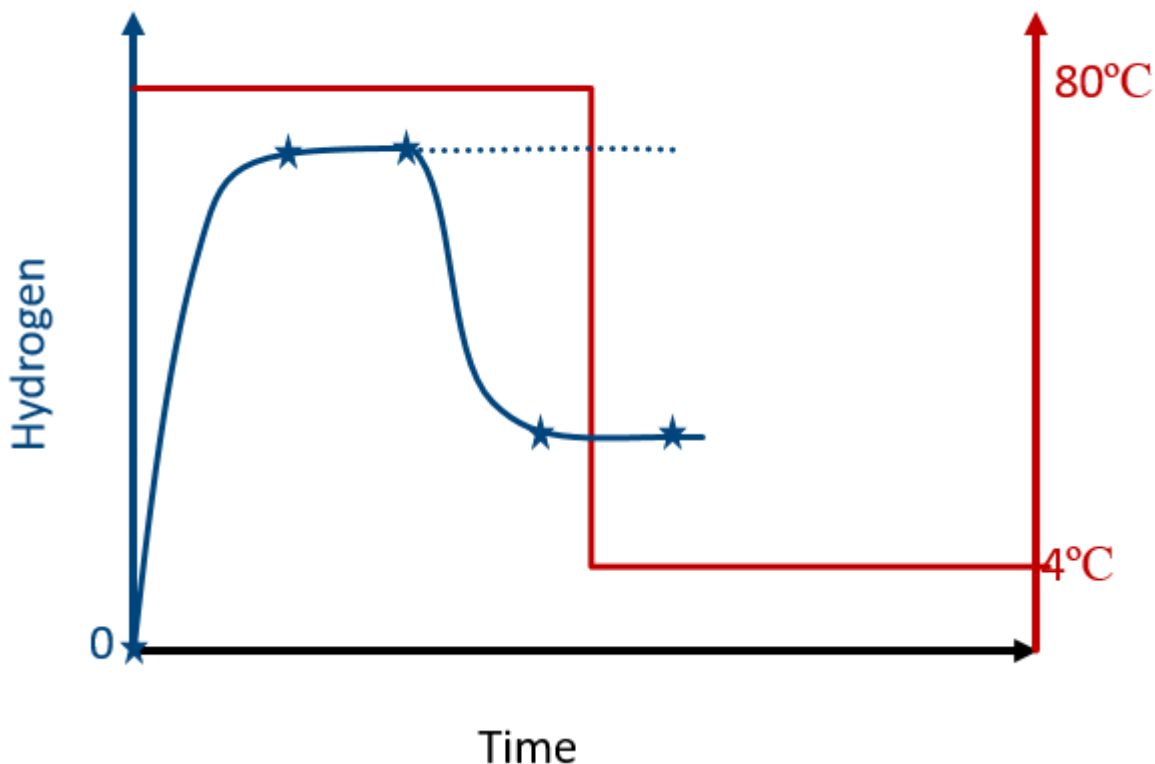
A theory of oversaturation in HAZ after a temperature drop for clad pipes welded with Alloy 50 (Nickel based FCC filler material) is explained in the report. To check this effect, a different test program that needs much longer time of charging is needed. Some simplified tests were performed, these gave no signs of reduced toughness due to oversaturation, but the time of charging was not long enough to conclude that oversaturation in HAZ after a shutdown cannot cause HISC.

7 Suggestion to further work

To investigate temperature effect and possible oversaturation of HAZ in dissimilar welds

1 Establish hydrogen saturation level as a function of temperature

- Precharge material FCC filler materials (Alloy 59 and Inconel 625) to establish saturation level at high temperatures (operation temperature)
- Reduce temperature to 4°C to establish a new saturation level at low temperature
- A solid round bar/wire for the precharging is suggested, small pieces is cut from the bar/wire when it is time for hydrogen measurements. This will solve the problem with lose of electric contact experienced in this project.
- Establish hydrogen diffusion properties that can be used in simulations (saturation level/sub surface level and diffusion coefficient)



2 Precharging of HISC specimens

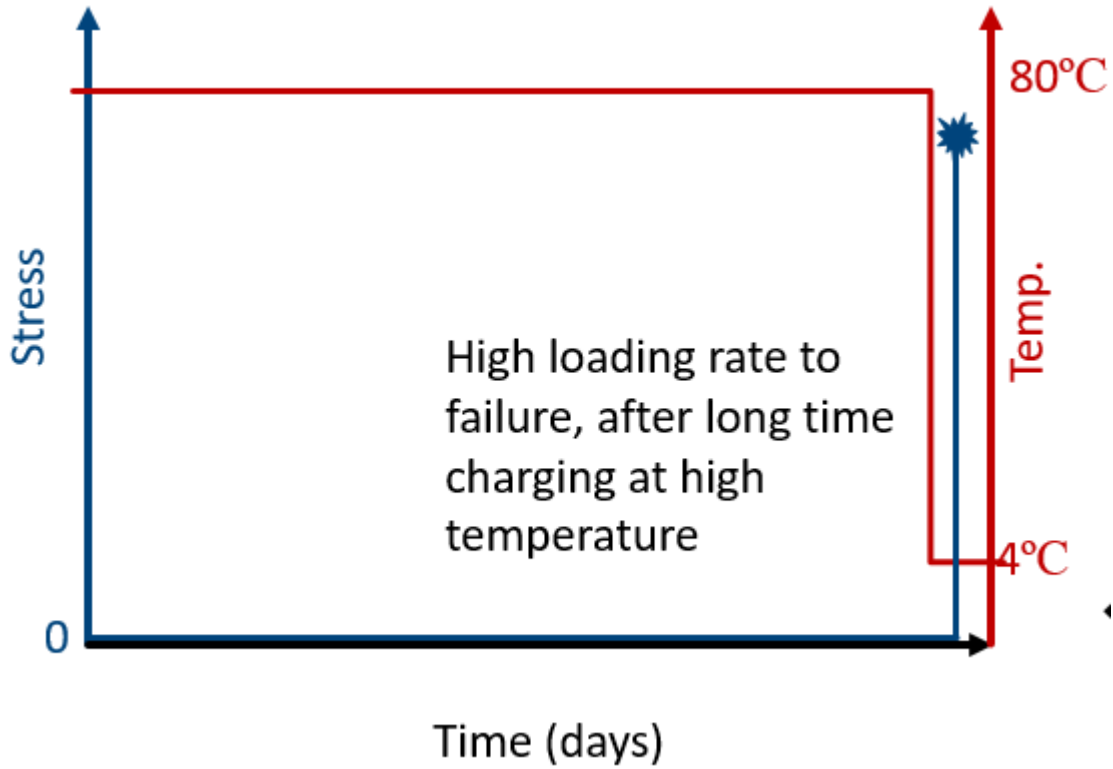
- It is suggested to machine smooth specimens without a notch. As discussed in the report, HISC is likely to start in the middle of the material where the oversaturation effect is believed to be strongest
- Precharging of specimens should start in parallel with activity 1.

3 Establish the time to saturation of the HISC specimens

- Activity one will be finished before the specimens is saturated. Based on the results in activity 1, the time to saturation of the specimens in activity 2 can be established

4 Testing of the precharged specimens

- Load the specimens to failure after the specimens is cooled down to 4°C





Technology for a better society

www.sintef.no